Fundamental Insights into the Radium Uptake into Barite by Atom Probe Tomography and Electron Microscopy

Juliane Weber

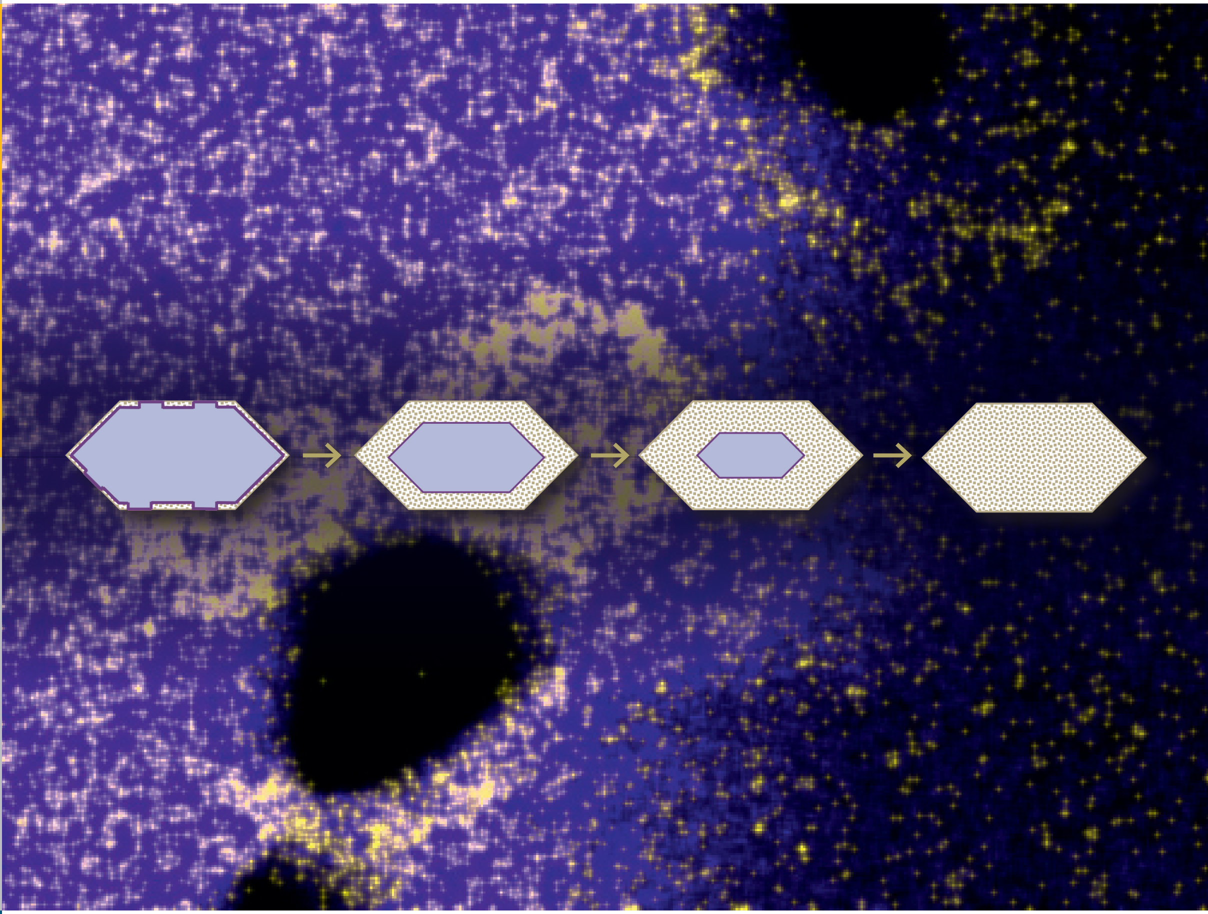

Member of the Helmholtz Association

Energie & Umwelt /
Energy & Environment
Band / Volume 367
ISBN 978-3-95806-220-7

JÜLICH
FORSCHUNGSZENTRUM

Schriften des Forschungszentrums Jülich
Reihe Energie & Umwelt / Energy & Environment Band / Volume 367

Forschungszentrum Jülich GmbH
Institut für Energie- und Klimaforschung
Nukleare Entsorgung und Reaktorsicherheit (IEK-6)

Fundamental Insights into the Radium Uptake into Barite by Atom Probe Tomography and Electron Microscopy

Juliane Weber

Schriften des Forschungszentrums Jülich
Reihe Energie & Umwelt / Energy & Environment Band / Volume 367

ISSN 1866-1793 ISBN 978-3-95806-220-7

Bibliographic information published by the Deutsche Nationalbibliothek.
The Deutsche Nationalbibliothek lists this publication in the Deutsche Nationalbibliografie; detailed bibliographic data are available in the Internet at http://dnb.d-nb.de.

Publisher and Distributor:
Forschungszentrum Jülich GmbH
Zentralbibliothek
52425 Jülich
Tel: +49 2461 61-5368
Fax: +49 2461 61-6103
Email: zb-publikation@fz-juelich.de
www.fz-juelich.de/zb

Cover Design: Grafische Medien, Forschungszentrum Jülich GmbH

Printer: Grafische Medien, Forschungszentrum Jülich GmbH

Schriften des Forschungszentrums Jülich
Reihe Energie & Umwelt / Energy & Environment, Band / Volume 367

D 82 (Diss. RWTH Aachen University, 2017)

ISSN 1866-1793
ISBN 978-3-95806-220-7

Ein Gelehrter in seinem Laboratorium ist nicht nur ein Techniker;
er steht auch vor den Naturgesetzen wie ein Kind vor der Märchenwelt.

Marie Curie

(1867-1934)

Alles Gescheite ist schon gedacht worden, man muss nur versuchen, es noch einmal zu denken.

Johann Wolfgang von Goethe

(1749-1832)

Abstract

Recently, the $Ba_xRa_{1-x}SO_4$ solid solution has been investigated with regard to its applicability to the long-term safety of spent nuclear fuel (SNF) disposal. As ^{226}Ra originates from the U decay chain, its concentration in SNF builds up with time. In some scenarios for the direct disposal of SNF taken from the Swedish license application for a final SNF repository, ^{226}Ra dominates the dose after 100,000 years. Currently, the solubility of ^{226}Ra is considered to be controlled by the formation of $RaSO_4$ in the Swedish license application as the $Ba_xRa_{1-x}SO_4$ solid solution characteristics were not sufficiently investigated at the point of submission. The $Ba_xRa_{1-x}SO_4$ solid solution could be considered as solubility controlling phase for Ra if the uptake mechanism of Ra into barite was understood in more detail.

Barite can occur as a primary phase in the surrounding of the future repository or as a secondary phase within nuclear waste due to the different positions of Ba and Ra within SNF. In the case of SNF corrosion, Ba would come in contact with water first. Sulfate-containing water would lead to barite precipitation. Therefore, a system is most likely where pre-existing barite is in equilibrium with an aqueous solution into which Ra then enters. Recent studies comprising long-term batch recrystallization experiments propose a kinetically influenced uptake of Ra into barite that equilibrates into a thermodynamically controlled situation within 800 days.

This thesis provides the first detailed four-dimensional characterization of the Ra uptake into barite by combining three-dimensional sample characterization with the temporal evolution. To understand the mechanism of Ra uptake into barite, two types of barites (SL and AL barite) obtained from batch recrystallization experiments of previous studies were characterized prior to, during and after the Ra uptake. A combination of different state-of-the-art high-resolution microscopy techniques was used to answer the questions regarding (1) the internal microstructure of the initial barite (2) the role of this internal microstructure during the Ra uptake and (3) the changes in the Ra distribution within the barite.

This study comprises the first characterization of barite by atom probe tomography (APT). By combining APT and transmission electron microscopy (TEM) methods, pores covering the size range from a few nanometers to a few micrometers were identified in the SL barite. The pores were organized in layers parallel to the outer crystal faces. High resolution chemical analysis indicated that the pores contain a solution of water and sodium chloride. By focused ion beam (FIB) tomography, it was revealed that open macropores of several micrometers size are present as well within the SL barite. These partially connected macropores are distributed within the complete barite particles. Therefore, the macropores provide a direct pathway for

Ra-containing aqueous fluid to enter the SL barite particles by diffusion within the aqueous solution. In addition, pores were also identified in the AL barite by TEM characterization.

The entrapment of solution during mineral precipitation is known for several minerals at high supersaturation. As barite only precipitates at high supersaturation, nano-scale fluid inclusions as well as macropores probably were entrapped during the particle growth by precipitation. A microstructure similar to the one of the barite type used in this study was previously reported for other barites. In Ra-free reference experiment, no microstructural changes were noted over recrystallization times of up to 898 days.

In prior studies, three different stages of Ra uptake were described based on macroscopic results. Ra-containing barite samples from all three stages were characterized to understand the role of the internal barite microstructure. At the beginning, the nano-scale fluid inclusions disappeared, probably due to coalescing to new macropores. This was part of an Ostwald ripening process driven by the minimization of the free energy in the complete system.

Furthermore, chemical analyses by Scanning TEM energy-dispersive X-ray spectroscopy (STEM-EDX) were conducted and a characteristic evolution of the Ra distribution within the solids with time was observed. After an intermediate, inhomogeneous Ra distribution within the barite, a homogeneous Ra distribution at the scale of STEM-EDX was detected.

In conclusion, the Ra uptake into barite takes place in several steps: first, the Ra-diffuses within the aqueous phase into the open macropores where it is incorporated into the barite via a dissolution-reprecitation process. The complex internal microstructure of the barite enlarges the barite surfaces and the uptake process takes place from the inside of the barite particles. The recrystallization of barite in the presence of Ra is completely different from pure barite recrystallization as the uptake of Ra causes fundamental changes within the Ra microstructure. The presence of Ra is a thermodynamic driving force which triggers the complete barite microstructure to rebuild despite the low concentration of Ra. A possible reason for these significantly different effects could be the radiation damage that is caused by the alpha-decay of ^{226}Ra.

Kurzzusammenfassung

Die $Ba_xRa_{1-x}SO_4$ Mischkristallreihe wird momentan als mögliche löslichkeitsbestimmende Ra-Phase für ^{226}Ra im Kontext der direkten Endlagerung abgebrannter Brennelemente (englisch: *spent nuclear fuel*, SNF) untersucht. ^{226}Ra ist ein Zerfallsprodukt der U-Zerfallsreihe. Daher baut sich seine Konzentration im abgebrannten Kernbrennstoff mit der Zeit auf und ist für die Langzeitsicherheit eines potenziellen Endlagers wichtig. In einigen Szenarios, die aus dem Genehmigungsverfahren der schwedischen Endlageragentur SKB für die direkte SNF-Endlagerung stammen, dominiert ^{226}Ra nach etwa 100.000 Jahren die Dosis. In dem aktuellen schwedischen Sicherheitsnachweis wird die Löslichkeit von ^{226}Ra durch das Löslichkeitsprodukt von $RaSO_4$ beschrieben, da die Eigenschaften von $Ba_xRa_{1-x}SO_4$ zum Zeitpunkt des Einreichens des Sicherheitsnachweises noch nicht in ausreichendem Maße erforscht waren.

Baryt kann sowohl als primäre Phase in der Umgebung eines zukünftigen Endlagers als auch als Sekundärphase innerhalb des Abfallgebindes auftreten. Aufgrund der verschiedenen Positionen von Ba und Ra innerhalb des SNF, ist die Entstehung des folgenden Systems anzunehmen: Ein bereits existierender Baryt befindet sich im Equilibrium mit einer wässrigen Lösung; anschließend wird Ra freigesetzt. Studien, in denen Langzeit-Rekristallisationsexperimente durchgeführt wurden, zeigten einen anfänglich kinetisch beeinflussten Einbau von Ra in Baryt. Innerhalb von 800 Tagen entwickelte sich dieses System zu einem thermodynamischen Gleichgewichtszustand hin.

Durch eine drei-dimensionale Probencharakterisierung in Kombination mit der zeitlichen Entwicklung wurden neue Erkenntnisse in den Ra-Einbau in Baryt gewonnen. Um den Ra-Einbaumechanismus in Baryt zu verstehen, wurden zwei verschiedene Arten von Baryten (SL und AL Baryt) aus Rekristallisationsexperimenten vor, während und nach dem Ra-Einbau charakterisiert. Eine Kombination verschiedener hochmoderner Mikroskopie-Techniken wurde angewendet um (1) die interne Mikrostruktur, (2) die Rolle dieser internen Mikrostruktur und (3) die Entwicklung der Ra-Verteilung während des Ra-Einbaus zu untersuchen.

Erstmals ist in dieser Arbeit eine Messung von Barytproben mit der Atomsonde (Atom Probe Tomography, APT) gelungen. Durch die Kombination von APT und verschiedener Transmissionselektronenmikroskopie (TEM) Methoden wurden Poren mit einer Größe zwischen einigen Nanometern und wenigen Mikrometern im SL Baryt identifiziert. Diese Poren bilden ein Lagensystem parallel zu den äußeren Kristallflächen. APT Analysen zeigten, dass die Poren mit H_2O und NaCl gefüllt sind. Durch eine Tomographie mit Hilfe des fokussierten Ionenstrahles (*Focused Ion Beam*

(FIB)) wurden außerdem offene, Mikrometer große Makroporen im SL Baryt beobachtet. Diese teilweise verbundenen Makroporen sind im gesamten Kristallvolumen verteilt und bieten so eine Wegsamkeit für Ra, um durch Diffusion in der wässrigen Phase in den Baryt zu gelangen. Ähnliche Poren wurden durch TEM Analysen im AL Baryt detektiert. In Ra-freien Referenzexperimenten konnte trotz Rekristallisationszeiten von bis zu 898 Tagen keine internen mikrostrukturellen Veränderungen beobachtet werden.

Basierend auf vorhergehenden makroskopischen Studien wurde der Ra-Einbau in drei verschiedene Stadien eingeteilt. Um die Veränderungen in der internen Mikrostruktur zu identifizieren, wurden Ra-haltige Barytproben aus allen drei Stadien untersucht. Anfangs verschwinden die nanometer-großen flüssigkeitsgefüllten Einschlüsse, wahrscheinlich durch das Zusammenwachsen zu neuen Makroporen. Dies ist Teil eines Ostwaldreifungsprozesses, angetrieben durch die Minimierung der freien Energie im gesamten System. Mit Hilfe von Rastertransmissionselektronenmikroskopie in Kombination mit energiedispersiver Röntgenmikrobereichsanalyse (STEM-EDX) wurden Element-Mappings aufgenommen und die zeitliche Entwicklung der Radiumverteilung innerhalb des Feststoffes analysiert. Nach einer temporären, inhomogenen Ra-Verteilung innerhalb des Barytes wurde im dritten Stadium eine auf der Skala von STEM-EDX homogene Ra-Verteilung beobachtet.

Der Ra-Einbau in Baryt findet in mehreren Schritten statt: Zuerst diffundiert das Ra in der wässrigen Phase durch die offenen Makroporen in den Baryt, wo es anschließend durch einen Auflösung/Wiederausfällungsprozess aus dem Inneren des Kristalles in den Baryt eingebaut wird. Durch eine Rekristallisation des kompletten Barytes entsteht ein homogener $Ba_xRa_{1-x}SO_4$ Mischkristall.

Die Rekristallisation des reinen Barytes unterscheidet sich grundlegend von der Rekristallisation unter Radiumeinbau, wie anhand der internen mikrostrukturellen Veränderungen zu erkennen ist. Hier stellt das Ra trotz seiner geringen Konzentration eine thermodynamische Triebkraft dar, die den kompletten Umbau der internen Mikrostruktur des Barytes verursacht. Ein möglicher Grund für diese signifikanten Unterschiede in der Rekristallisation könnten die durch den Alpha-Zerfall des Radiums verursachten Strahlenschäden darstellen.

Abbreviations

AL	Aldrich® Barite
APT	Atom Probe Tomography
BF	Bright Field
BSE	Back-scattered electrons
EDX	Energy-dispersive X-Ray spectroscopy
ER-C	Ernst Ruska-Centrum
DFT	Density Functional Theory
FIB	Focused Ion Beam
FWHM	Full Width at Half Maximum
HAADF	High-Angle Annular Dark-Field
HR	High Resolution
NORM	Naturally Occurring Radioactive Materials
PSD	Particle Size Distribution
SAED	Selected Area Electron Diffraction
SEM	Scanning Electron Microscopy
SL	Sachtleben® Barite
SNF	Spent Nuclear Fuel
STEM	Scanning Transmission Electron Microscopy
TEM	Transmission Electron Microscopy
ToF-SIMS	Time-Of-Flight Secondary Ion Mass Spectrometry

1 Introduction

Mining and milling of U ores, including waste waters, tailings and waste rock produce radionuclides containing waste. In addition, residues originating from other industries contain U and Th decay series radionuclides, e.g. the phosphate industry, mineral sand processing, oil, gas or coal industry. These residues are called natural occurring radioactive materials (NORM). Radium (Ra) is extremely important among the radionuclides of concern (U, Th, Ra, Rn, Pb and Po) due to the presence of its isotopes in all natural decay series and their relatively long half-life (Fesenko et al., 2009). Furthermore, it is easily accumulating in bones in the case of ingestion into the body. In addition, the gaseous Rn poses a severe health threat. Ra is considered as a key nuclide for the long-term safety of nuclear waste disposal due to its long half-life (Bruno et al., 2007; Curti et al., 2010).

The characteristics of Ra dissolved in aqueous solution, its fate during migration and its immobilization by possible secondary phases are investigated as dissolved Ra tends to be very mobile in various elemental conditions. Elevated Ra concentrations were found in produced water from hydraulic fracturing and oil production (Nabhani et al., 2016) but also in some drinking waters (Milvy & Cothern, 1990; Somlai et al., 2002; Bonotto, 2015). Because radionuclides can easily be ingested by drinking contaminated water, drinking water is monitored regarding its radioactivity in many countries. For example, the Ra limit in drinking water is 5 pCi (= 0.158 Bq) per liter (EPA, 2000) in the USA and in Germany the total activity limit of the alpha-emitters per liter of water is 0.1 Bq (Dritte Verordnung zur Änderung der Trinkwasserverordnung, 2015).

The formation of a solid solution is, among other processes as e.g. sorption, a possibility to immobilize Ra or other hazardous elements dissolved in aqueous solutions. The aqueous concentration needed for a minor element to get incorporated in a solid solution can be significantly smaller than its aqueous concentration which needs to be reached for pure phase precipitation. In the case of Ra, the aqueous Ra concentration needed for the formation of a $Ba_xRa_{1-x}SO_4$ solid solution would be several orders of magnitude lower than the solubility of pure $RaSO_4$. The sequestering of elements by solid solutions is widely recognized in environmental research, but has however only been taking into account in some cases, e.g. $Ba_xRa_{1-x}SO_4$ solid solution formation was considered in the Swiss nuclear waste safety case (Nagra, 2002; Prieto et al., 2013; 2016).

Ra is easily incorporated in barite and forms the $Ba_xRa_{1-x}SO_4$ solid solution (Curie, 1898; Hanor, 2000; Randa et al., 2010). Barite is an ubiquitous mineral which occurs in a variety of sedimentary, metamorphic and igneous geological environments (Hanor, 2000). The $Ba_xRa_{1-x}SO_4$ solid solution has recently been investigated in more detail with regards to the long-term safety of spent nuclear fuel (SNF) disposal (Bosbach et al., 2010; Curti et al., 2010; Vinograd et al., 2013; Klinkenberg et al., 2014; Brandt et al., 2015). One of the main tasks of our generation is to establish a safe disposal for SNF which mainly consists of UO_2 (Bruno & Ewing, 2006). As ^{226}Ra originates from the U decay chain, its' concentration builds up within SNF with time due to the decay of ^{234}U and ^{238}U. In some scenarios for the direct disposal of SNF (Fig. 1) taken from the Swedish license application for a final SNF repository, ^{226}Ra dominates the dose after 100,000 years and even leads to a second peak in the total dose which exceeds the typical background radiation in Sweden (SKB, 2011).

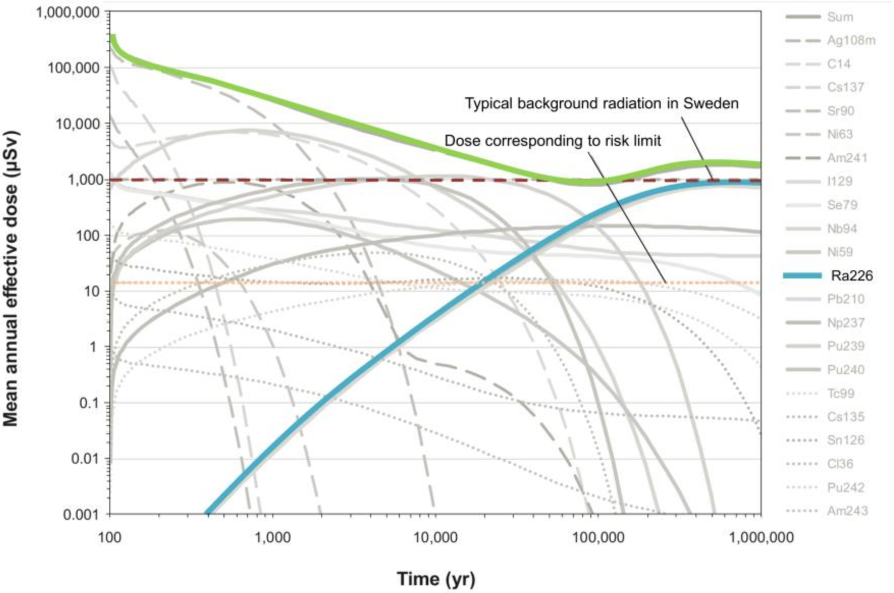

Fig. 1 Mean annual effective dose [µSv] in a special case of canister corrosion taken from the Swedish Nuclear Fuel and Waste Management Company (SKB). The contribution of Ra (blue line) to the total dose (green line) leads to a second peak after 300.000 years with possible doses above the level of the typical background radiation in Sweden (Modified after SKB, 2011).

Independent from the strategy of waste management, e.g. conditioning, long-term interim storage or direct disposal of the spent nuclear fuel from today's point of view, the deep geological disposal is the safest option to which no adequate alternative has yet been proposed (Röhlig et al., 2012; Baisden & Atkins-Duffin, 2011; Alexander & McKinley, 2007; Kim et al., 2011; EU, 2011; Ewing et al., 2016). Primarily, deep geological disposal is favored because it provides the best option for maintaining the two main safety principles: isolation and containment. The deep geological disposal in rock formations allows the radioactive waste enough time for the decay of its radioactive isotopes to natural levels in isolation from the environment. Another important requirement is the immobilization of radionuclides. This can be assured by the combination of technical and geotechnical barriers, e.g. canisters, backfilling, buffer and the selection of the host rock. Three different host rock types were identified as potentially suitable for the disposal of radionuclides: clay, salt and crystalline rock (Röhling et al., 2012; BGR, 2007). In Germany, no decision for one of these potential host rocks was taken since the restart of the final repository program in 2013 (§ 3 Standortauswahlgesetz).

Other countries like Finland, Sweden or France have already advanced in the process towards bringing a final repository into service (Posiva, 2014; Bennett & Gens, 2008). The Swedish waste management agency SKB has submitted its license application for a high-level waste disposal site in granitic rock in 2011 (Fig. 2) (SKB, 2011) and the Finnish waste management agency Posiva has submitted the construction license application in 2012. The Finnish construction license was granted in 2015 (Posiva, 2015).

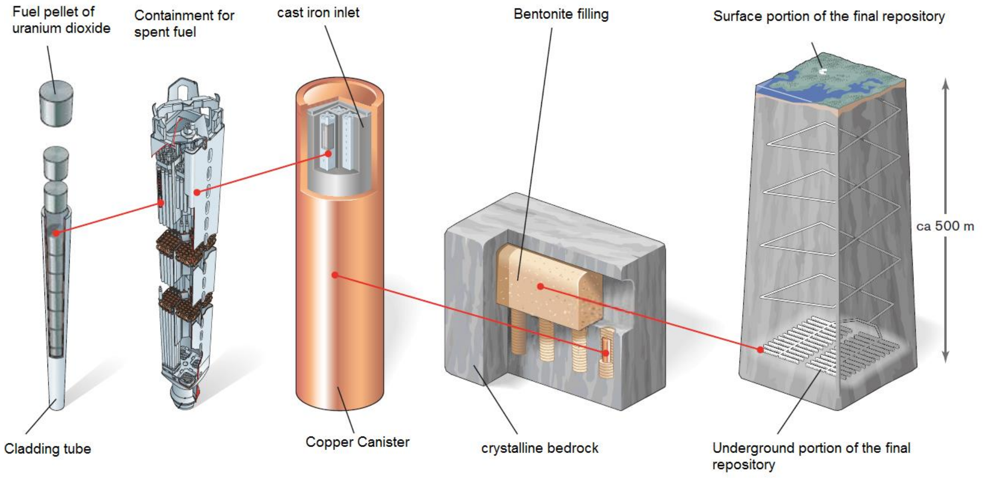

Fig. 2 The KBS-3 concept of spent nuclear fuel disposal by the Swedish SKB (Modified after SKB, 2010).

The provision of a long-term safety assessment evaluating the possibility of a release of radionuclides into the bio- or geosphere over a timescale of one million years is necessary for the license application of a repository (IAEA, 2012; Ojovan &

Lee, 2014). The behavior of radionuclides within this time-span is rather difficult to derive directly from laboratory experiments. Therefore, a long-term safety assessment includes probability calculations for radionuclide retention on different host phases and various scenarios, e.g. canister failure due to corrosion or buffer transformation. Crucial information for a reliable calculation is the assessment of possible interactions of radionuclides with primary or secondary mineral phases. Usually, this detailed information on the radionuclides interactions with mineral phases and dissolved species, e.g. stability constants, is obtained from laboratory experiments, which are further combined into a simulation of more complex processes in multicomponent systems (IAEA, 2012). This approach is the most favorable one for modeling the radionuclide behavior in the complex geochemical systems, as it is based on a fundamental knowledge about the system (e.g. composition, ionic strength, redox- and pH conditions, etc.) and radionuclides interactions.

A number of processes can lead to retention of radionuclides in the near-field of a repository system, e.g. adsorption on mineral surfaces, precipitation of pure phases or solid solution formation. These processes are substantially different on a molecular level but may result in a similar outcome on the macroscopic level. A molecular scale process understanding is still necessary to gain confidence in the long-term predictions made in the safety assessment. Therefore, the characterization of radionuclide interactions in a geochemical system on a molecular level is a prerequisite for a reliable safety assessment (Bruno et al., 2007).

In the submitted license application for a Swedish high level waste repository, the solubility of ^{226}Ra is considered by the formation of $RaSO_4$ because the $Ba_xRa_{1-x}SO_4$ solid solution characteristics were not sufficiently investigated (SKB, 2011). In the technical report for provisional safety analyses of the Swiss NAGRA calculations are performed with $RaSO_4$ and $RaCO_3$ as limiting solids for the upper guideline. Here, the solid solution formation between $BaSO_4$ and $RaSO_4$ is used for the lower guideline (NAGRA, 2014). There is evidence that barite might be present in the surrounding of the planned repository in Forsmark (Jaremalm et al., 2013) or forms as a secondary phase in some scenarios (SKB, 2011). In the specific bentonite examined as possible geotechnical barrier for the Swiss SNF repository, barite is present. Therefore, the $Ba_xRa_{1-x}SO_4$ solid solution formation could be considered in general as solubility controlling phase for Ra if the thermodynamic properties of this solid solution and the uptake mechanism of Ra into barite were known in more detail.

Barite can occur as a secondary phase in a nuclear waste repository. In Sweden, a final repository for the direct disposal of SNF will be built in granitic basement rock (SKB, 2011). The SNF will not be conditioned but it will be stored in Cu canisters which are surrounded by a bentonite filling. Already during the construction of such a repository fractures in the crystalline rock are existent and therefore the presence of water within the repository is likely and addressed in the safety assessment. By technical means (canister design and engineered barrier system), a possible migration of radionuclides should be prevented. Nevertheless, canister corrosion and water infiltration followed by a contact between spent nuclear fuel and water are considered as possible individual and combined scenarios.

The location of Ra and Ba within SNF differs. Within fresh nuclear fuel, stable Ba isotopes are already present as fission products. Ba results from ^{137}Cs and ^{135}Cs decay within SNF and it is part of the grey phase as oxide precipitates, e.g. (Ba,Sr)ZrO_3. During the operation time, the Ba precursor Cs is transported to the grain boundaries, fractures or the region between SNF and cladding (Bruno & Ewing, 2006; Brandt et al., 2015). ^{226}Ra will build up from ^{238}U and ^{234}U decay and is therefore located either in the UO_2 matrix or within secondary uranium phases. After the operation time, in the possible case of fuel corrosion, Ba is then more easily accessible compared to Ra. Therefore, in case of contact between SNF and a sulfate-rich groundwater, Ba is released first and then quickly precipitated as $BaSO_4$ due to its low solubility. Accordingly, barite would be in equilibrium with the aqueous solution and then, Ra would enter (Fig. 3).

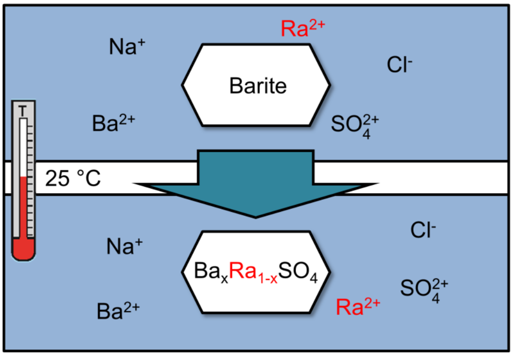

Fig. 3 **System of an aqueous sulfate solution including Ra^{2+} in equilibrium with barite (adapted from Klinkenberg et al., 2014).**

Recent studies have shown that pre-existing barite takes up Ra in long-term batch recrystallization experiments of about 800 days (Bosbach et al., 2010; Curti et al., 2010, Torapova et al., 2013, Klinkenberg et al., 2014; Brandt et al., 2015).

In the scenario mentioned above, the Ra concentration in aqueous solution is controlled by the solubility of a $Ba_xRa_{1-x}SO_4$ solid solution rather than by the solubility of a pure $RaSO_4$ phase. This assumption was made based on thermodynamic modeling, demonstrating a decrease of Ra solubility in the presence of pre-existing barite at close-to-equilibrium conditions (Vinograd et al., 2013). The combination of a stable Ra concentration in solution and a homogeneous Ra distribution within the solids indicate that a stable state is reached which can be thermodynamically predicted. A microscopic study by Klinkenberg et al. (2014) applying time-of-flight secondary ion mass spectrometry (ToF-SIMS) showed the uptake of the Ra into the barite crystal volume. In addition, Brandt et al. (2015) modeled the evolution of the Ra concentration in solution using the thermodynamic interaction parameter for the $Ba_xRa_{1-x}SO_4$ solid solution obtained by Vinograd et al. (2013). This enabled the prediction of the $Ba_xRa_{1-x}SO_4$ and the composition of the aqueous solution in equilibrium conditions with this solid. At the same time, due to the new observations made by Klinkenberg et al. (2014) and Brandt et al. (2015) a number of new questions arose. These questions are related to the internal microstructure of the initial barite, the potential changes within the internal barite microstructure and the homogeneity of the Ra distribution at equilibrium state. The answers would lead to a process understanding of the Ra uptake. The focus of this thesis is to develop a mechanistic understanding at a molecular scale of the Ra uptake into barite.

2 Scientific and Theoretical Background

2.1 Radium

Radium (Ra) is the sixth element of the second group in the periodic table, the alkaline earth metals and present in nature in doubly charged oxidation state. Due to similar ionic radii and resulting similar chemical behavior, Ba data has often been used if Ra was not available (Carvalho et al., 2014).

There are four naturally occurring isotopes of Ra, ^{223}Ra (half-life: 11.4 days) originating from the Ac decay series, ^{224}Ra (3.64 days) and ^{228}Ra (5.75 years) originating from the Th decay chain and ^{226}Ra (1602 years) from the U decay chains. The most long-living isotope ^{226}Ra decays to several isotopes, e.g. the gaseous isotope ^{222}Rn, to the stable isotope ^{206}Pb (Carvalho et al., 2014). Historically, research on Ra was concentrated on its impact on human health (e.g. Raabe et al., 1989; Sheen et al., 2016; Warren, 1980), its application as a tracer for environmental processes (e.g. Burnett et al., 2008; Krest & Harvey, 2003) or its use in industrial, medical or other application (e.g. Pratt,1993). This study is focused on the interaction of Ra dissolved in an aqueous solution with a pre-existing bariumsulfate (barite) solid.

Studies reporting the preparation of the Ra-containing halogenides, RaF_2, $RaCl_2$, $RaBr_2$ and RaI_2 exist, but the crystal structure of the solids decays within 10 h to amorphous material due the high radioactivity and accompanying radiation damage (Weigel & Trinkl, 1968). The Ra-salts $RaSO_4$, $RaSeO_4$, $RaCrO_4$, $RaMoO_4$ and $RaWO_4$ are more stable to radiation damage (Weigel & Trinkl, 1968a). Also $RaCO_3$ exists, but its solubility (K_{sp} = -8.3, Langmuir & Riese, 1985) is higher than that of $RaSO_4$ (K_{sp} = -10.26, Langmuir & Riese, 1985). The solubility of pure $RaSO_4$ will be discussed in detail in the next chapter.

Pure Ra phase precipitation of any of these Ra-phases in nature was not observed, probably due to the low molar Ra concentrations found in nature (Carvalho et al., 2014, 2014). Some solid phases in nature are known to take up Ra at conditions close to the thermodynamic equilibrium. Barite is one phase which is particularly known for incorporating Ra by recrystallization (Grandia et al., 2008; Bosbach et al., 2010). Minor amounts of Ra were found to incorporate into Celestine (Jucker & Treadwell, 1954). Other mineral phases, as e.g. gypsum ($CaSO_4$ x H_2O) were observed to poorly incorporate Ra (Jucker & Treadwell, 1954).

The kinetically influenced co-precipitation of Ra is another way to fixate Ra in solids. Here, Ra can also be sequestered in a phase which is thermodynamically not favorable, e.g. Ra precipitation with gypsum (Yoshida et al., 2009). When carbonate concentrations in waters are high, Ra and also other alkaline earth metals are precipitated as carbonate. Curti (1999) reviewed the available data on the partitioning of Ra and other radionuclides into calcite. This review was further supported by studies of Rihs & Condomines (2002) and Sturchio (1990) reporting co-precipitation experiments with Ra and calcite. Also the precipitation as a ternary solid solution of $(Ba,Ra,Sr)SO_4$ was observed (Zhang, 2014).

The $Ba_xRa_{1-x}SO_4$ solid solution was previously observed to be a scavenger for Ra. Therefore, the incorporation of Ra into barite by recrystallization at thermodynamic equilibrium and also the co-precipitation of a $Ba_xRa_{1-x}SO_4$ solid solution will be elaborated further in this thesis. In order to describe and understand the characteristics of the $Ba_xRa_{1-x}SO_4$ solid solutions, the end-members of this solid solution, $RaSO_4$ and $BaSO_4$, will be described first.

Already the discovery and the following investigation of the element Ra were closely related to its co-precipitation with barite and to the formation of a $Ba_xRa_{1-x}SO_4$ solid solution. In her ground-breaking work on the discovery of Ra, Marie Curie (1898) reported about the affinity of Ra for barite. Later, Curie stated in her Nobel Prize lecture (Curie, 1911) that she had used barite extracts for the recovery of Ra from the U residues.

The ionic radii of the Ba^{2+} and Ra^{2+} ions in 12-fold coordination only differ by 5 % (Tab. 1). A complete substitution of the two divalent cations should be possible according to the Goldschmidt rule (Goldschmidt, 1925). Also the unit cell parameters of both structures are similar, which should allow the formation of a complete solid solution (Tab. 1).

Tab. 1 Characteristics of the end-members of the $BaSO_4$-$RaSO_4$ solid solution. Ionic radii of Ba^{2+} and Ra^{2+} in 12-fold coordination from Shannon (1976) as well as lattice parameter of barite by Jacobson et al. (1998) and of $RaSO_4$ by Hedström et al. (2013)

Mineral	$BaSO_4$	$RaSO_4$
Ionic radius [12] [Å]	1.61	1.70
a [Å]	8.879	9.07
b [Å]	5.454	5.52
c [Å]	7.154	7.28

Although the formation of solid solutions with intermediate compositions should be possible based on thermodynamics, only barites containing minor amounts of Ra were observed in nature (Hanor et al., 2000; Randa et al., 2010). Radiobarites observed in nature often originate from hydrothermal precipitates (Randa et al., 2010).

2.2 Properties of $RaSO_4$

Due to its absence in natural environments and its high radioactivity, few studies are available on the characteristics of pure $RaSO_4$. Pure $RaSO_4$ has been used in medical applications (Weigel & Trinkl, 1968). Curie (1904) mentioned it but it was described in more details by Kolowrat (1910) and Hönigschmid (1911). The density of pure $RaSO_4$ is 5.77 g/cm³ and the molar volume 55.87 cm³/mol (Weigel & Trinkl, 1968).

The solubility of $RaSO_4$ was first studied by Lind et al. (1918) in pure water and at different ionic strength of sulfuric acid. Further experiments on the solubility of pure $RaSO_4$ were performed by Nikitin and Tolmatscheff (1933) in pure water and in 0.015 M Na_2SO_4 solutions at 293 K. Langmuir and Riese (1985) applied the results of Nikitin and Tolmatscheff (1933) for the calculation of $\log K_{RaSO_4}$ = -10.38 ± 0.02 at 293 K. Paige et al. (1998) used the experimental results of Nikitin and Tolmatscheff (1933) in pure water and additionally data from Lind et al. (1918) in H_2SO_4 to calculate $\log K_{RaSO_4}$ at 298 K using the Pitzer model (Pitzer, 1973). Values from -10.42 ± 0.03 to -10.21 ± 0.06 were obtained for K_{RaSO_4}. The thermodynamic constant implemented in the Nagra-PSI database (Thoenen et al., 2014) for $RaSO_4$ is $\log K_{RaSO_4}$ = -10.26 as obtained by Langmuir and Riese (1985). A detailed summary of all thermodynamic data available for $RaSO_4$ is included in Vinograd et al. (2013). Brown et al. (2015) gave a review of the temperature dependence for the $RaSO_4$ solubility.

2.3 Properties of $BaSO_4$

Barite is one of the best studied minerals in geosciences. It is a naturally occurring ubiquitous mineral (Hanor, 2000). It often occurs as unwanted scale in the oil and gas industry and therefore, its crystallization has been investigated in detail. In addition, its' easy cleaving characteristics make it suitable as a model mineral for many surface investigations (Fenter et al., 2001; Bosbach et al., 1998; Pina et al., 1998; Stack & Rustard, 2007; Stack, 2009) regarding the dissolution and precipitation rates of barite.

Barite is a rather soft mineral, with a Mohs hardness of 3 - 3.5 (Okrusch & Matthes, 2010). The calculated molar volume of barite is 47.95 cm³/mol based on the density of 4.48 g/cm³ (Hanor, 2000). In comparison to other minerals, barite is highly insoluble but shows a quick recrystallization. Barite powder recrystallization studies in the presence of a ^{133}Ba tracer have shown that the complete barite crystal is exchanged within several hundred days. Powders with different particle size distributions were investigated and no link between the particle size and uptake rate was observed (Curti et al., 2010, Bosbach et al., 2010). A recent review on stable mineral recrystallization at low temperatures stated that small particles (nm to µm scale) can be chemically very dynamic due to observed recrystallization (Gorski et al., 2016). In addition, the application of high resolution characterization is recommended for the identification of subtle changes in the mineral during recrystallization.

In the final report of the European project SKIN *"Slow processes in close-to-equilibrium conditions for radionuclides in water/solid systems of relevance to nuclear waste management*" (Grambow et al., 2014), it is concluded that for many other minerals than barite, the surface isotopic exchange rate is directly proportional to the detachment rates. For these minerals, a higher reaction rate results in a faster exchange with a monolayer. This is completely different for barite. The dissolution rate is smaller compared to e.g. calcite but the exchange in calculated monolayers is five orders of magnitudes higher. This behavior then lead to the conclusion that the existing phase is dissolved and subsequently, a new phase is precipitated (Grambow, 2013).

Naturally occurring barite is often formed by mixing of fluids originating from the alteration of silicate, carbonate and sulfate minerals in sedimentary, metamorphic and igneous rocks (Hanor, 2000). In these naturally formed barites, different defects were reported. Fluid inclusions in the micrometer scale are often reported in literature (Bodnar et al., 2014; Böhlke & Irwin, 1992; Rajabzadeh, 2007; Wilkinson, 2001; Zou et al., 2015; Jamieson et al., 2016; Asl et al., 2015). Furthermore, opaque material in oriented layers within the barite's crystal structure was detected. No chemical reason for these opaque layers was found so far (Frondel, 1935; Luedeking & Wheeler, 1891; Parr & Chang, 1935). Recently, barite deposits within hydrothermal vents from the Endeavour Segment, Juan de Fuca Ridge, were characterized by light microscopy and SEM. Again, layers were observed in this barite. At higher resolution, these layers were identified to consist of fluid inclusions (Jamieson et al., 2016).

Several studies on barite solubility in water and salt solutions at ambient conditions and elevated temperatures are available (Melcher, 1919; Neuman, 1933; Morey & Hesselgesser, 1951; Templeton, 1960; Uchameyshvili et al., 1966; Puchelt, 1967, Blount, 1977; Langmuir & Melchior, 1985; Paige et al., 1998). Blount calculated a $\log K_{BaSO_4}$ of -9.97 and as well investigated the effect of temperature on the solubility of barite in the range of 295 – 553 K. In addition, the solubility of barite as a function of pressure at different salt concentrations was investigated in this study.

The ionic interaction theory (Pitzer, 1973) was applied to the results of Blount (1977) in 0.2 and 1.0 M NaCl solution at 298 K and 373 K by Langmuir & Melchior (1985). Hereby, they showed that the data are consistent with the Pitzer model. The thermodynamic data which are listed in the Nagra-PSI database (Thoenen et al., 2014) are taken from the study of Helgeson et al. (1978) with the same solubility for barite as given by Blount (1977).

2.4 Immobilization of Radium by Solid Solution Formation: The $Ba_xRa_{1-x}SO_4$ Solid Solution

The main immobilization processes are adsorption, absorption or secondary phase formation. The different immobilization processes differ regarding their effectiveness and their reversibility. Adsorption occurs when a contaminant is immobilized by accumulating at the interface between the aqueous and a pre-existing solid phase without forming a three-dimensional molecular arrangement (Bruno et al., 2007). When one or more water molecules of the adsorbate are lost during the adsorption process, a chemical bond is formed. This process is called specific adsorption or chemisorption. If the water molecule is preserved during the process, the interaction is weaker. In this case, the adsorption is referred to as non-specific or physisorption and based on physical energies, e.g. Van-der-Waals forces (Brown et al., 1992; Zangwill, 1988).

The uptake of a chemical component from the aqueous solution into an existing solid phase by diffusion into the complete volume is called absorption. Zeolites are an example for minerals that immobilize contaminants by absorption (Bruno et al., 2007). In other mineral systems than zeolites, diffusion rates of cations are rather low. Zhang et al. (2010) reported ~10^{-17} m^2/s at 1600 K as a characteristic diffusion rate for cations in minerals. Compared to the characteristic values for aqueous diffusion rates of 10^{-9} m^2/s at 300 K or diffusion in silicate melts with a rate of 10^{-11} m^2/s at 1600 K (Zhang et al., 2010), this diffusion coefficient is lower. In Zhang (2008) an overview of 18 different references for experimental data on cation diffusion in a variety of minerals is presented. No experiments with barite are reported. The mineral system which probably resembles the $Ba_xRa_{1-x}SO_4$ system best is Sr diffusion in calcite. The experiments on Sr diffusion in calcite were conducted in a temperature range between 713 - 1073 K (= 439.85 - 799.85 °C) providing a function for the temperature dependency. Accordingly, the calculated diffusion coefficient at ambient conditions would be 2.2 x 10^{-58} m²/s. Therefore, bulk diffusion can be neglected for the interpretation and analysis of geochemical processes at ambient temperatures, as e.g. weathering or interaction of pollutants and minerals.

The formation of a secondary phase is less easily reversible than sorption (Poinssot & Geckeis, 2015). Secondary phases can be formed by precipitation or solid solution formation. The transfer of a dissolved contaminant from the aqueous to the solid phase by growing a three-dimensional arrangement is called precipitation. The grown three-dimensional arrangement is called the crystal structure.

Precipitation can occur as a pure phase precipitation when the solubility of this phase is reached. In addition, the precipitation of a solid solution by co-precipitation of two different components is possible. The formation of a solid solution can be thermodynamically more favorable than the precipitation of a pure phase. This may already be the case for small concentrations of contaminants and provides the possibility of an effective immobilization. Frequently, this characteristic is used in process engineered barriers for the retention of metals, radionuclides or other pollutants (Prieto et al., 2016). A very specific case of solid solution formation is the uptake of a solvent into a pre-existing solid. In this work, the case of interaction between a pre-existing barite solid and an aqueous solution containing Ra was investigated.

Depending on the mineral phases present in the environment, Ra^{2+} can be immobilized in different ways, e.g. by sorption onto clays (Ames et al., 1983 a+b) or absorption into zeolites (Jurado-Vargas et al., 1997; Chalupnik et al., 2013). Theoretically, also a pure Ra-containing mineral phase as e.g. $RaSO_4$ could precipitate. However, the precipitation of pure $RaSO_4$ has so far not been reported in nature. The high concentration of Ra in solution which is required to precipitate pure $RaSO_4$ might explain the lack of natural $RaSO_4$ precipitates. In general, the naturally occurring Ra content of rocks in the upper crust is low leading to low concentrations ($<10^{-11}$ mol/L) of Ra in natural groundwaters as well as in surface waters (Grandia et al., 2008). Therefore, these natural Ra concentrations always stay below the solubility limit of $RaSO_4$. To explain this finding, Sturchio et al. (1990) and Grundl & Cape (2006) have proposed the formation of a solid solution with barite. This is close to a circular argument because it can also be the case that the Ra concentration in nature is low per se and this is the reason why it is thermodynamically more favorable to be incorporated into barite than the precipitation of a pure phase.

The process of a $Ba_xRa_{1-x}SO_4$ solid solution formation was observed both in nature (Randa et al., 2010) and experimentally (Doerner & Hoskins, 1925; Klinkenberg et al., 2014; Brandt et al., 2015).

2.4.1 Theory of solid solution formation in aqueous solutions

In contrast to a mechanical mixture, where two or more solids are physically mixed, a solid solution is the combination of two or more solids forming a homogeneous crystalline structure by replacing atoms on defined crystallographic positions. The extent of the mixing and the ideality of the solid solution depends ob the size and charge of the substituting ions on a specific structural site and also the geometry of this site. For a binary solid solution (B,C)A, two mass-action equations define the thermodynamic equilibrium conditions (1) and (2).

$$\{B^{+}\}\{A^{-}\} = K_{BA}a_{BA} \tag{1}$$

$$\{C^{+}\}\{A^{-}\} = K_{CA}a_{CA} \tag{2}$$

In the curly brackets, the activities of the uncomplexed B^{+}, C^{+} and A^{-} ions are given; a_{BA} and a_{CA} are the activities of the BA and CA components in the solid solution and K_{BA} and K_{CA} are the corresponding thermodynamic solubility products. When both equations are satisfied at the same time, the system is at equilibrium. It can be difficult, however, to determine when this is the case. A complete description of the determination of these thermodynamic calculations can be found in Prieto (2009) and Prieto et al. (2016).

As the final compositions of the aqueous and solid solution at equilibrium depend on the initial solid/aqueous phase ratio, the calculation requires the conservation of mass of the solid-solution components as well as the conservation of charge in the solid. For the solution of these equations, a speciation code can be applied to determine the distribution of aqueous species and the aqueous activity coefficients from the aqueous concentration determined experimentally.

In equation (1) and (2) activities instead of mole fractions (X) are used. These are related to the mole fractions by equation (3):

$$a_{BA} = \gamma_{BA}X_{BA} \tag{3}$$

γ_{BA} is a dimensionless activity coefficient which is used to account for the non-ideality of solid solutions. a_{CA} is defined by an analogous expression. In case of an ideal solid solution, the solid phase activity coefficients are equal to 1. Therefore, the relations $a_{BA} = X_{BA}$ and $a_{CA} = X_{CA}$ are valid for all compositions. In non-ideal solid solution the activity coefficients vary depending on the solid solution composition and it is critical to define them in order to be able to describe the thermodynamic equilibrium conditions. A further description about the thermodynamics of solid solution can be found in Prieto (2009), Glynn et al. (1990), Glynn, (2000). Two expressions are needed to describe the activity coefficients of the components BA and CA in the solid solution:

$$ln\gamma_{BA} = X_{CA}^2[a_o + a_1(3X_{BA} - X_{CA}) + a_2(X_{CA} - X_{BA})(5X_{BA} - X_{CA}) + \ ...] \tag{4}$$

and

$$ln\gamma_{CA} = X_{BA}^2[a_o + a_1(3X_{CA} - X_{BA}) + a_2(X_{CA} - X_{BA})(5X_{CA} - X_{BA}) + \ ...] \tag{5}$$

a_0, a_1, a_2 are dimensionless parameters which were obtained by fitting experimental values of the excess free energy of mixing (ΔG_E) to a Guggenheim expansion series. The free excess energy of mixing is defined as the difference between the free energy of mixing (ΔG_M) of a given solid solution and the free energy of mixing of an equivalent ideal solid solution. ΔG_M is the difference between the free energy of the solid solution (G_{SS}) and the free energy of a mechanical mixture of the pure endmembers (G_{MM}).

$$\Delta G_E = X_{BA}X_{CA}[a_o + a_1(X_{BA} - X_{CA}) + a_2(X_{BA} - X_{CA})^2 + \ ...]RT \tag{6}$$

where R is the gas constant and T the absolute temperature in [K]. The dimensionless a_0 can also be converted into the interaction parameter W_H [J/mol] which is also often used:

$$W_H = a_0RT \tag{7}$$

The formation of a solid solution has a fundamental effect which is that the incorporation of a minor ion (C^+) into a suitable host phase (BA) can significantly reduce the aqueous concentration of C^+. The concentration required for the thermodynamic possibility of immobilization at equilibrium conditions is then lower than its concentration at equilibrium with the endmember, the CA solid.

2.4.2 The Lippmann theory

For the complete description of a solid solution-aqueous solution system at thermodynamic equilibrium, both equations (1) and (2) need to be fulfilled simultaneously. Lippmann (1980) defined the concept of the total solubility product Π, where Π is defined as (Equation (8):

$$\sum \prod = \{A^-\}(\{B^+\} + \{C^+\}) \tag{8}$$

In addition, he proposed two equilibrium conditions to be fulfilled simultaneously:
First, the solidus

$$\sum \prod\nolimits_{eq} = K_{BA}\gamma_{BA}X_{BA} + K_{CA}\gamma_{CA}X_{CA} \tag{9}$$

and second, the solutus:

$$\sum \prod\nolimits_{eq} = \frac{1}{\frac{X_{B,aq}}{K_{BA}\gamma_{BA}} + \frac{X_{C,aq}}{K_{CA}\gamma_{CA}}} \tag{10}$$

Using one mole fraction of the endmember phase, one mole fraction of an aqueous species and the total solubility product, Lippmann constructed a new type of diagram for describing equilibrium conditions in solid solution-aqueous solution system by a graphical representation of equation (9) and (10). This diagram works on a similar basis as regular phase diagrams and therefore it can be easily interpreted by geochemists.

To construct a Lippmann diagram, the solidus and solutus must be presented on the ordinate against a superimposed scale on the abscissa. Similar to conventional phase diagrams, horizontal tie lines between the solidus and solutus curve can give pairs of $X_{c,aq}$ and X_{CA} at which equilibrium conditions are fulfilled. The Lippmann diagram of the $Ba_xRa_{1-x}SO_4$ solid solution calculated using the values obtained in the study of Vinograd et al. (2013) is presented in Fig. 4.

This Lippmann diagram is based on the calculations of Vinograd et al. (2013) which determined the standard entropy of $RaSO_4$ and the regular interaction parameter of the $Ba_xRa_{1-x}SO_4$ solid solution by first principles. By using this approach, the interaction parameter was determined to be $a_0 = 1.0 \pm 0.4$. This value is in very good agreement with experimental data from recrystallization experiments (Vinograd et al., 2013; Brandt et al., 2015; Klinkenberg et al., 2014). Regarding the Lippmann diagram, this value suggests an alyotropic point close to the barite end-member of the solid solution (Vinograd et al., 2013). Alyotropic points are points in the Lippmann diagram, were solidus and solutus touch as indicated in Fig. 4.

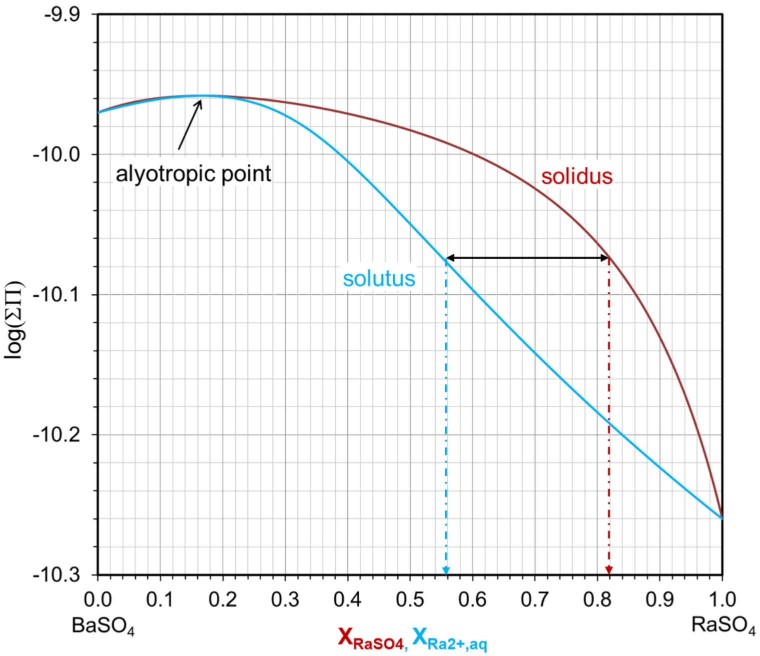

Fig. 4 Lippmann diagram for the $Ba_xRa_{1-x}SO_4$ solid solution at 25 °C. K_{RaSO_4} = -10.26 and a_0 = 1 were used by Vinograd et al. (2013).

2.4.3 Experimental work on the $Ba_xRa_{1-x}SO_4$ solid solution

In previous studies, two different approaches with regard to the supersaturation state were used to investigate the solid solution experimentally. Co-precipitation of $^{226}Ra^{2+}$ with Ba^{2+} and SO_4^{2-} from a supersaturated solution was performed as well as the interaction of $^{226}Ra^{2+}$ with pre-existing barite in an equilibrated aqueous solution was observed.

Co-precipitation of Ra^{2+} with Ba^{2+} and SO_4^{2-}

In the 1920's and 1950's, ground-breaking studies on the co-precipitation of Ra with barite precipitates have been conducted (Doerner and Hoskins, 1925; Gordon & Rowley, 1957; Jucker, 1954; Jucker and Treadwell, 1954). The general scheme of co-precipitation experiments is presented in Fig. 5. In the studies of Doerner & Hoskins (1925), Gordon & Rowley (1957), Jucker (1954) and Jucker & Treadwell (1954), sulfuric acid was added to a solution of $RaCl_2$ and $BaCl_2$.

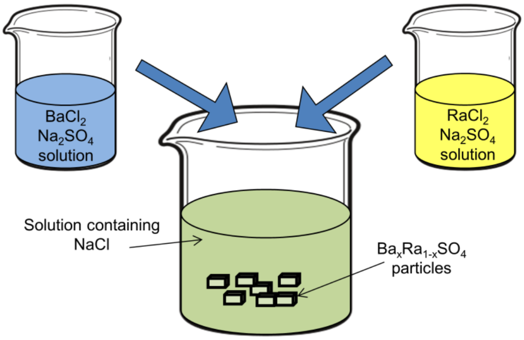

Fig. 5 Scheme of co-precipitation of Ba$_x$Ra$_{1-x}$SO$_4$ crystals.

A correlation between a decreasing concentration of Ra in an aqueous solution and an increasing amount of precipitated barite crystals was observed. Based on these observations, Doerner & Hoskins (1925) established the following logarithmic law (Eq. 11):

$$ln\frac{\{Ra\}_{surface}}{\{Ba\}_{surface}} = \lambda \times ln\frac{[Ra]_{solution}}{[Ba]_{solution}} \qquad (11)$$

$\{Ra\}_{surface}$ and $\{Ba\}_{surface}$ are the element fractions on the solid surface, $[Ra]_{solution}$ and $[Ba]_{solution}$ are the total Ra^{2+} and Ba^{2+} concentrations in the solution. λ is a proportionality constant, which is also called the heterogeneous partition coefficient. This relation is also known as the Doerner-Hoskins distribution law and is limited to closed system, in which no further Ra is added to the solution.

In many natural and experimental systems this law is used for the description of element partitioning between aqueous and solid phases during precipitation from an aqueous solution (Lorens, 1981; Lorens, 1978; Zhong & Mucci, 1995; Roden et al., 2002).

The Doerner-Hoskins partition coefficients may vary as a function of the metal complexation or the ionic strength because they are defined by total element concentrations. Curti (1999) classified such partition coefficients as phenomenological partition coefficients in contrast to those based on free ion activities which he defines as thermodynamic partition coefficients. Based on this distinction, Curti (1999) suggests a new equation for the calculation of the thermodynamic partition coefficient λ^0 (Eq. 12):

$$\lambda^0 = \frac{a_{RaSO_4}(Ba^{2+})}{a_{BaSO_4}(Ra^{2+})} = \frac{K^0_{BaSO_4}}{K^0_{RaSo_4}} \tag{12}$$

with a_{RaSO4} and a_{BaSO4} are the activities of the Ra and Ba in the solid $RaSO_4$ and $BaSO_4$ phase respectively. (Ba^{2+}) and (Ra^{2+}) are the activities of the free Ba^{2+} and Ra^{2+} cations in the solution and K_{BaSO4} and K_{RaSO4} are the thermodynamic solubility products. It is possible to compute a thermodynamic partition coefficient of a divalent metal ion into a mineral phase whenever the solubility products at zero ionic strength of the pure end-members are known.

Most published partition coefficients are phenomenological, with only a few exceptions (e.g. Tesoriero & Pankow, 1996; Davis et al., 1987). The interpretation is further complicated by the fact that many authors do not distinguish between phenomenological and thermodynamic distribution coefficients. It has to be noted, that thermodynamic and phenomenological partition coefficients may differ greatly in case of non-ideality of either the aqueous solution (ionic strength and complexation effects) or the solid solution (Curti, 1999). Additionally, terminologies as partition coefficient, exchange coefficient, distribution coefficient and fractionation coefficient are used indiscriminately for different expressions and depending on the publication; the meaning of the coefficient varies (Prieto et al., 2010).

Studies on the partition coefficients observed that a recrystallization of the precipitated solid occurred already during the co-precipitation process and therefore the Doerner-Hoskins coefficient was not accurate in this case (Morse & Bender, 1990). Zhu (2004) published calculated interaction parameters describing the ideality of the $Ba_xRa_{1-x}SO_4$ solid solution based on the experimental data of Doerner & Hoskins (1925) and Langmuir & Riese (1985). In these studies, the distribution coefficients were obtained from experiments far from the thermodynamic equilibrium. The further use of these coefficients which are only valid in restricted cases for the calculation of thermodynamic constants can be considered problematic because kinetic influences on the system cannot be excluded. Possible kinetic influences were reported e.g. for (Sr,Ca)CO_3 precipitation experiments of Plummer & Busenberg (1987) at 25 °C, where a homogeneous solid solution formed that segregated the more soluble $CaCO_3$ component. The problematic use of phenomenological coefficients is explained in detail by Curti (1999).

Barite recrystallization in the presence of Ra^{2+} in aqueous solution

The interaction of a pre-existing barite solid with an aqueous solution that contains Ra is another possible scenario in nature. To investigate this interaction, replacement experiments can be conducted (Fig. 6). Replacement experiments are batch mineral recrystallization experiments in the presence of an aqueous solution containing a cation, e.g. a radionuclide. The concentration of the cation in the aqueous solution is monitored and the uptake into the solid can be calculated. In contrast to previously described co-precipitation experiments, were kinetic effects at high supersaturation are used to force a thermodynamically unfavorable phase to precipitate, replacement experiments are conducted at conditions near to the thermodynamic equilibrium. For this kind of experiments, reference experiments are a prerequisite to enable a reliable and meaningful analysis of the effects during the replacement experiment.

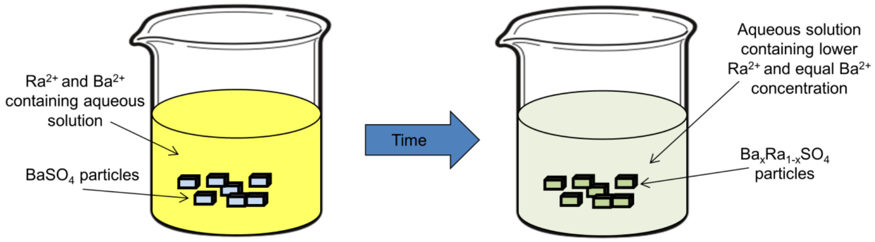

Fig. 6 **Replacement experiments of barite recrystallization in an aqueous solution containing Ra^{2+}.**

The first replacement experiments were conducted by Germann (1921) who reported the uptake of Ra into barite after he noticed that Ra in a radiumchloride solution was “lost” during the addition of barite. The Ra-containing barite solids were characterized with the emanation method and he concluded that Ra adsorption onto the barite surface took place (Germann, 1921).

Doerner & Hoskins (1925) did not only conduct co-precipitation experiments but also less recognized experiments regarding the uptake of Ra by pre-existing barite. In these studies, a $RaCl_2$ solution was added to a barite solid. After a heating of the mixture, an interaction of barite with the $RaCl_2$ solution was observed. The initial barite concentration, the digestion time and the temperature were varied in order to establish a relationship between the observed Ra^{2+} partition into the solid phase and the different experimental parameters. Doerner & Hoskins (1925) concluded that the solid phase did not reach equilibrium within five days and that sorption could not be the responsible mechanism for the uptake. Experiments without heating of the mixture did not show a perceivable Ra uptake into barite within the time frame of the experiments (4 days). The solids from these experiments were analyzed by the emanation method and Doerner & Hoskins (1925) concluded that Ra is located “inside” the particles. However, there is no statement in which form Ra is located inside the barite, whether it is e.g. a fluid inclusion or a structural uptake with a solid solution formation. Based on the utilized methods, no statements about the form in which the Ra is present inside the barite could be made and the retention mechanism is not explored. A detailed characterization of the solids and their internal microstructure is missing. The Ra uptake into barite within a rather short period of five days was also observed by Wang et al. (1993). They were able to observe a correlation between the decrease in the Ra concentration in the aqueous solution and a larger specific surface of the barite particles. However, no attempt was made to analyze the actual retention mechanism in more detail.

In their review, Grandia et al. (2008) pointed out that a mechanistic study on the interaction of Ra with pre-existing barites was missing. Such studies were started by Bosbach et al. (2010) and Curti et al. (2010) who published investigations on barite recrystallization in the presence of Ra on a time scale of up to one year. Here, an additional uptake of Ra was observed beyond the amount which could be expected purely by adsorption. Klinkenberg et al. (2014) and Brandt et al. (2015) conducted long-term studies on the Ra uptake into barite with recrystallization times up to three years within the SKIN project. Additionally, a thermodynamic model of the system was developed by first-principle calculations (Vinograd et al., 2013). Compared to the computational study of Zhu (2004) based on experimental data, the first principle calculations by Vinograd et al. (2013) are only premised on electronic configurations and then verified by experimental data available at that time.

Vinograd et al. (2013) proceeded by using the following approach: The phonon density states of $RaSO_4$ were computed using density functional perturbation theory. The regular interaction parameter of the $Ba_xRa_{1-x}SO_4$ solid solution was interpreted as the slope of the enthalpy of mixing in the limit of infinite dilution. The slope was calculated from the change in total energy in a 2 x 2 x 2 barite supercell due to the insertion of a substitutional defect of Ra (Vinograd et al., 2013).

For the calculation of the interaction parameters of the $Ba_xRa_{1-x}SO_4$ solid solution, the single defect method (SDM) was used. SDM is based on the idea that W_H is equal to the ratio of the change of enthalpy of mixing (ΔH_{mix}) and the change in molar fraction in the solid (ΔX), $\Delta H_{mix}/\Delta X$, where at $X = 0$ $H_{mix} = X(1-X)W_H$. The derivative can be approximated as $\Delta H_{mix}/\Delta X$. The change in enthalpy of mixing is calculated by density functional theory (DFT) which was applied to a supercell of $BaSO_4$ with a single substitutional defect of Ra. This means, that a 2 x 2 x 2 barite supercell with 32 atoms and a composition of $Ba_{31}Ra_1(SO_4)_{32}$ was used. The excess energy of this supercell is then calculated relatively to the mixture of 31 $BaSO_4$ and 1 $RaSO_4$. The corresponding excess energies of $BaSO_4$ and $RaSO_4$ are calculated with DFT and measured per mole of SO_4. Therefore, the excess energy is in praxis multiplied by 1/32. Therefore, $\Delta X = 1/32$. The factor 32 cancels out and the W_H is equal to the excel energy of the used supercell.

In comparison to the previous calculations of Zhu (2004), the study of Vinograd et al. (2016) used electronic configurations which do not contain any empirical values and the uncertainty is reduced (Winkler, 1999; Milman & Winkler, 1999; Dove, 2003).

Klinkenberg et al. (2014) provided the first detailed microscopic characterization of both Ra-free reference barite particles as well as Ra-containing barites after Ra uptake. Particle size distribution (PSD) analysis via SEM and a chemical analysis by ToF-SIMS were conducted. ToF-SIMS analysis showed the uptake of Ra into the crystal volume. The PSD analysis prior to and after the Ra uptake proposed that the grain size does not significantly change during the uptake. The consistent morphology of the barite particles prior to and after Ra uptake indicated that an internal, intragranular process controls the Ra uptake and solid solution formation. Already in this study, it was evident that Ra-free reference experiments are crucial for interpreting the observations made by Ra uptake experiments.

Böttcher & Dietzel (2010) remarked independently from the SKIN project that further studies were needed to understand the complex dissolution behavior of solid solutions at low temperatures to understand pathways and rates of natural processes in solid solution-aqueous solution systems. Torapova et al. (2014) conducted barite recrystallization experiments in the presence of ^{223}Ra and ^{133}Ba with a very low Ra-concentration (e.g. <10^{-13} mol/L ^{223}Ra). At these low concentrations Ra was retained by barite as well.

Brandt et al. (2015) applied thermodynamic calculations for the interpretation of the temporal evolution of the Ra concentration in batch experiments of the same type as conducted by Klinkenberg et al. (2014) and in this doctoral thesis. Different stages of Ra uptake into the solid were postulated based on these calculations (Brandt et al., 2015). The direct observation of these postulations within the solids could be made by the application of high resolution microscopy methods for the analysis of the Ra-free reference barites and the Ra-barites.

A schematic representation of the three stages described in Brandt et al. (2015) is given in Fig. 7. In stage 1, a rapid drop in the aqueous Ra concentration was observed. Then, a further drop of the aqueous Ra concentration below the calculated thermodynamic equilibrium concentration defines the beginning of stage 2. Brandt et al. (2015) suggested the nucleation of Ra-barite as a reason for the rapid drop in the aqueous Ra concentration. The further drop below the thermodynamic equilibrium concentration was explained by kinetic effects as e.g. entrapment (Brandt et al., 2015; Thien et al., 2014). Finally at stage 3, the aqueous Ra concentration approaches a plateau which is in good agreement with the calculated thermodynamic equilibrium concentration of Vinograd et al. (2013). In combination with the ToF-SIMS characterization showing the presence of Ra within the barite crystal volume (Klinkenberg et al., 2014), true solid solution formation with a structural incorporation of the Ra into the barite lattice is most likely at stage 3.

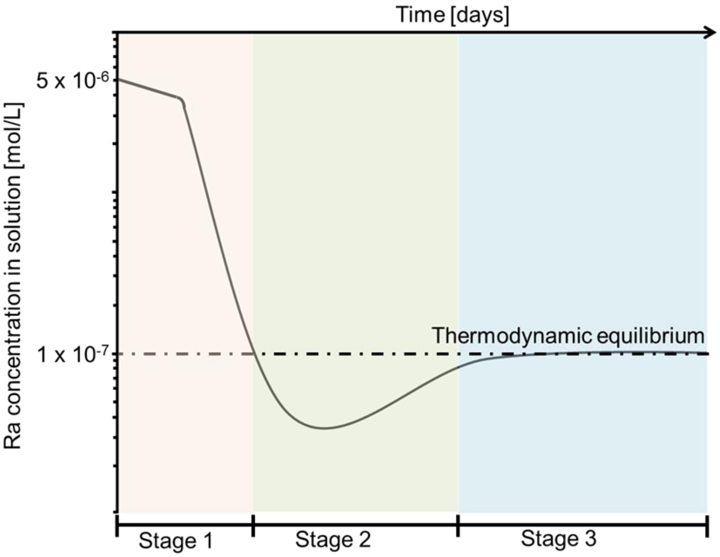

Fig. 7 Schematic evolution of the Ra concentration in the aqueous solution in the experiments of Klinkenberg et al. (2014) and Brandt et al. (2015).

Based on these new observations, new questions arose. The combination of exchanging Ra with the solution into the barite particles at room temperature with no changes in the particle shape and PSD makes an internal process most likely.

Based on the previous results, a detailed characterization of the solids from different points of the experiments could deliver the necessary information to gain a deep understanding of the Ra uptake process. The long-term analysis of the solution indicated which solids would be most interesting to characterize.

By analyzing solid samples of all stages, it would be possible to understand the role of the internal microstructure during the Ra uptake. Furthermore, a detailed chemical characterization could provide the evolution of the Ra distribution. This could possibly give further indications why more Ra than thermodynamically favorable was taken up by the barite during stage 2. Also, a description of the internal changes within the barite solids due to the Ra uptake could help to say whether the dissolution-reprecipitation process takes place as postulated of Brandt et al. (2015).

2.5 Replacement by water-mediated dissolution-reprecipitation

A complete uptake of Ra into barite was observed in the batch recrystallization experiments of 1200 days duration at ambient conditions (Brandt et al., 2015). Based on the characteristic diffusion coefficient in minerals (Zhang et al., 2010), a complete exchange of barite via solid state diffusion is not possible within this period of time.

Another possible mechanism for the replacement of mineral phases is a water-mediated dissolution-reprecipitation mechanism (Ruiz-Agudo et al., 2014). At ambient conditions, this replacement can take place within shorter time scales than solid state diffusion. The original mineral phase is then called parent phase. During the exchange, the morphology and the dimensions of the parent phase are typically maintained. This preservation of the external shape may explain the existence of mineral pseudomorphs which are often observed in nature (Schneiderhöhn, 1949; David et al., 1905; Workman & Cowperthawaite, 1963). The main prerequisite for this mechanism to take place is the presence of water. The presence of water, however, has been reported for nearly every environment on earth, even the mantle (Bell & Rossmann, 1992).

Several steps by which replacements take place have been postulated based on available experimental studies. The less stable phase dissolves during the exchange process and a more stable phase precipitates within a thin layer, the interfacial boundary layer. This starts an autocatalytic reaction where dissolution and reprecipitation are linked together (Fig. 8). During this process, the crystallographic information is transferred from the parent to the newly formed mineral phase which then possibly forms a pseudomorph by slow layer-by-layer dissolution and reprecipitation. The replacement reaction can only proceed if the contact between the interfacial boundary layer and the fluid is kept. In the reviews available on water-mediated replacement, the occurrence of connected porosity within the newly precipitated phase is mandatory to maintain this connectivity.

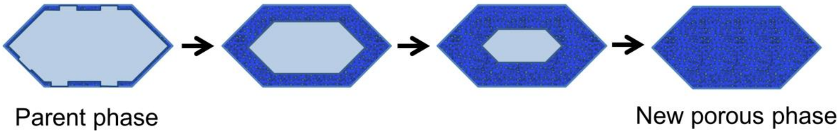

Fig. 8 **Schematic overview of the water-mediated replacement by a dissolution and reprecipitation mechanism (modified after Ruiz-Agudo et al., 2015).**

Different factors control the kinetics of a dissolution-reprecipitation reaction. A flowchart illustrating the relationship between the individual factors is presented in Fig. 9 based on the scheme in Jonas et al. (2013). The original scheme was modified and completed to properly address the important factors for the exchange of barite by a $Ba_xRa_{1-x}SO_4$ solid solution.

The bases of the replacement reaction are the conditions of the starting material and the solution. To develop a process understanding of the replacement of barite by a $Ba_xRa_{1-x}SO_4$ solid solution, the starting material has to be known in detail. The fluid pathways which are located inside the starting material influence the kinetics as well as their availability and geometry. Large availability and a good connectivity of the fluid pathways might reduce the time needed for the exchange and vice-versa. Furthermore, the internal microstructure of the starting material changes during the replacement process. Therefore, the characteristics of this new replacement product, e.g. newly generated porosity or how much of the original material is replaced change the kinetics of the reaction mechanism as well (Jonas et al., 2013).

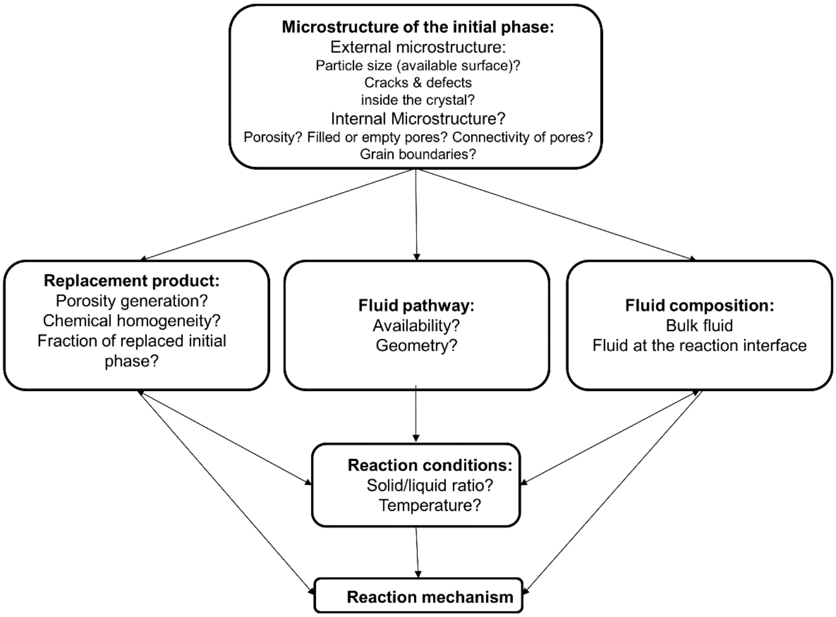

Fig. 9 Flowchart of the different factors that influence the reaction mechanism of the replacement reaction (modified after Jonas et al., 2013).

In general, porosity is considered to be an important transient feature during a water-mediated replacement via dissolution-reprecipitation (Putnis et al., 2005; Raufaste et al., 2011). At the end of a replacement process, a fluid-induced textural equilibration may take place (Ruiz-Agudo et al., 2014). This textural equilibration is a form of Ostwald ripening. The process is driven by the large interfacial energy generated by the porous structure. Ostwald ripening results in pore coarsening and in a possible loss of interconnectivity with following reduced permeability (Ruiz-Agudo et al., 2014).

2.5.1 Previous experimental work on replacement processes

The first studies on dissolution-reprecipitation were historical works on hydrothermal replacements which were not experimental but field studies. Goldsmith & Laves (1954) proposed the replacement mechanism by stating that hydrothermal feldspar-feldspar transformations may occur by the dissolution of the parent mineral and a subsequent precipitation of the new phase. In addition, Wyart & Sabatier (1958) demonstrated that a dissolution/reprecipitation process could possibly explain the weathering of labradorite with consecutive formation of orthoclase and anorthite. Furthermore, Merigoux (1968) demonstrated in his studies on the hydrothermal weathering of K-feldspars that the kinetics of the incorporation of ^{18}O into secondary Na-feldspar could be more easily explained by a replacement mechanism rather than solid state diffusion. O'Neil & Tylor (1967) proposed a new mechanism as possible alternative to the classic solid-state interdiffusion model. They suggest the existence of a thin fluid film between the interface of original and product phase. Parson (1978) stated that the replacement of orthoclase by microcline in plutonic rocks may happen by dissolution and reprecipitation.

The experimental studies of Putnis,C.V. et al. (2005), Putnis, A. (2002, 2009) and Putnis, A. & Putnis, C.V. (2007) on mineral replacement in the system KBr-KCl-H_2O then led to further experimental studies. In these studies, optically clear KBr crystals were put in contact with a saturated KCl solution. Subsequently, the replacement by KBr crystals by the propagation of a porous KCl layer towards the center of the KBr crystal was observed until complete replacement. This model system exhibits a fast recrystallization due to the difference in solubility between the two endmembers and due to the high level of supersaturation utilized in the experiments.

During the last ten years, numerous experimental studies on the replacement by coupled interfacial dissolution-reprecipitation were conducted. All of these studies are short-term studies with experimental durations of up to 49 days (Perdikouri et al., 2013). Many of the experiments were performed at elevated temperature up to 200 °C (e.g. Ruiz-Agudo et al., 2014; Pedrosa et al., 2016 a+b; Dunkel & Putnis, 2014) in order to enhance the kinetics of the replacement reaction. In some, not only the temperatures but also the pressure was elevated (Niedermeier et al., 2009; Hövelmann et al., 2010, Labotka et al., 2004; Majumdar et al., 2014). The conditions, under which the experiments were performed, make the transfer of the obtained conclusions to replacement processes in nature difficult. Furthermore, in most of these studies, millimeter size, optically clear crystals were used as starting materials (Ruiz-Agudo et al., 2015; Pedrosa et al., 2016; Pollock et al., 2011; Niedermeier et al. 2009; Hövelmann et al., 2010; Perdikouri et al., 2013; Putnis et al., 2013; Borg et al., 2014). In general, naturally occurring minerals include different impurities and defects, e.g. porosity. In addition, it has to be taken into account that natural minerals always contain impurities of other cations. In the case of barite, these could be Sr-impurities as $BaSO_4$-$SrSO_4$ also forms a solid solution (Hanor, 2000). The effect of such impurities on the dissolution-reprecipitation mechanism is to some extent unpredictable.

The studies of Klinkenberg et al. (2014) and Brandt et al. (2015) were designed to answer a scientific questions arising from the long-term safety assessment of the Swedish SKB. The experimental conditions were controlled very accurately in order to ensure that the system can be modeled. The observations made in prior studies may be explained best by a dissolution/reprecipitation mechanism. For this thesis, the previous studies of Klinkenberg et al. (2014) and Brandt et al. (2015) deliver all necessary information about the solution in detail as well as microscopic information about the solid. This offers the unique possibility to study the solids from well-characterized replacement experiments.

2.5.2 Volume changes and porosity evolution during dissolution-reprecipitation processes

The replacement of a parent mineral phase by a product phase is accompanied by changes in the porosity. Two main factors are influencing this change in porosity. The first factor is the difference in the molar volume between the parent and the product phase. In addition, the second factor influencing the change in porosity is the solubility of the two phases (Putnis & Austrheim, 2013; Ruiz-Agudo et al., 2014). Depending on the solubility, the change in porosity can either be an increase or a decrease. The solubility is determined by the grain size, fluid composition, temperature and pressure among other factors and will change during the replacement process. Large difference in solubility between parent (more soluble) and product (less soluble) phase might result in parent material loss during the reaction leading to an increased pore space in the product phase. Also an increase in molar volume can still result in a higher porosity. This was observed e.g. for the replacement of leucite by analcime (Putnis et al., 2007) or magnetite by pyrite (Qian et al., 2010). Furthermore, the strain which is related to high volume change reactions can induce fracturing which provides new pathways for fluid infiltration.

The change in porosity was defined by Pollock et al. (2011) not only regarding the molar volume but also the relative solubilities (Eq. (13):

$$V = 100 \times \left(\frac{n_p V_{m,p} - n_d V_{m,d}}{n_d V_{m,d}} \right) \tag{13}$$

where n_d and n_p are the number of moles of the parent dissolved and the product precipitated and $V_{m,d}$ and $V_{m,p}$ are the molar volumes of the dissolving and precipitating phase respectively. An extensive review on textural changes during mineral replacement by dissolution and reprecipitation is provided by Altree-Williams et al. (2015).

The change in molar volume for the exchange of barite by a $Ba_xRa_{1-x}SO_4$ solid solution can be estimated considering the change in molar volume by a complete replacement of barite by pure $RaSO_4$. Using the equation (14), the change in molar volume can be calculated using the molar volumes given in chapter 2.2 and 2.3. The precipitated and dissolved moles are set to one assuming complete replacement.

$$\Delta V = \left(\frac{1x55.87 - 1x47.95}{1x55.87}\right) = 14.17\ \% \tag{14}$$

Accordingly, the change in molar volume for the complete replacement of barite by pure $RaSO_4$ would be 14.07 %. Only limited amounts of Ra compared to the amount of $RaSO_4$ were available in the experiments and therefore, the complete exchange of barite by pure $RaSO_4$ was not possible during the experiment. Therefore, it can be concluded that the real value of change in molar volume by a replacement by a solid solution is between the number calculated for a complete exchange and zero exchange, which is the accordingly value for no change in molar volume. As remarked before, the solubilities at the interface have to be taken into account. Therefore, the calculated value can only be interpreted qualitatively.

2.5.3 Micro- and nanoscopic evidences for a dissolution-reprecipitation process

Several characteristics may indicate that a water-mediated replacement by dissolution-reprecipitation took place and therefore are useful for the identification of a replacement process:

(1) Preservation of the original morphology while changing the chemical composition or even the mineral phase (Ruiz-Agudo et al., 2014).
(2) A sharp, chemical interface between the parent and the new mineral phase (Ruiz-Agudo et al., 2014).
(3) Changes in the porosity: Depending on the difference in the molar volume between the two phases either generation of porosity or formation of cracks (Ruiz-Agudo et al., 2014).

In the previously conducted studies of Klinkenberg et al. (2014) and Brandt et al. (2015) some of these indication were observed. A detailed characterization of the morphology of the barite particles prior to and after the Ra uptake by Klinkenberg et al. (2014) showed no changes in the morphology and therefore demonstrates criterion (1). Furthermore, the ToF-SIMS depth profiles of the cited study indicated Ra uptake into the barite particle volume which excludes surface phenomena as mechanism for the Ra uptake. The criteria (2) and (3) have not been demonstrated so far. Furthermore, the available solid samples from long-term experiments also enable the observation of kinetic effects in the system. Therefore, the identification of the uptake process is a main topic to be investigated within this work.

2.6 High Resolution Methods

After the replacement of one mineral phase by another, three different microstructural characteristics indicate that the replacement took place via a dissolution-reprecipitation mechanism. Typical for this type of transformation are the preservation of the original morphology while changing the chemical composition, a sharp chemical interface between the old and the new mineral phase and changes in porosity (Ruiz-Agudo et al., 2014). All of these observations can only be made by microscopic methods. Furthermore, the internal microstructure in 3D of the samples enables a clear identification of the replacement process. This requires the use of either tomographic methods or special sample preparation prior microscopical characterization.

An overview of different microscopy methods, their resolution as well as chemical sensitivity is presented in Fig. 10. TEM methods offer the highest resolution to observe structural features. APT in contrast provides the highest chemical sensitivity at a very high spatial resolution. ToF-SIMS has a high resolution for flat samples, which is reduced for samples with an irregular morphology, e.g. powders. The relatively small barite particle size of 20 µm reduced the ToF-SIMS resolution down to the resolution presented in Klinkenberg et al. (2014).

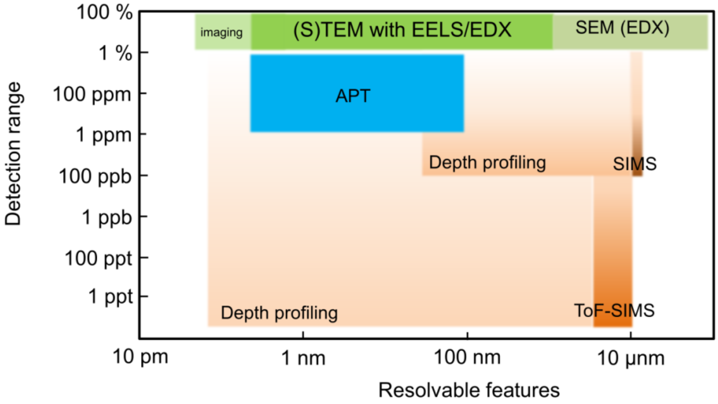

Fig. 10 Typical spatial resolution and detection range for some common microscopy techniques: (S)TEM ((Scanning) Transmission Electron Microscopy), EELS (Electron Energy Loss Spectroscopy), EDX (Energy Dispersive X-ray Spectroscopy), APT (Atom Probe Tomography), SEM (Scanning Electron Microscopy), SIMS (Secondary Ion Mass Spectrometry) and ToF-SIMS (Time-of-Flight SIMS). (Modified after Gault et al., 2012).

2.6.1 *Transmission Electron Microscopy (TEM)*

In detail, the local microstructural characterization of an electron transparent sample is possible by transmission electron microscopy. Electron microscopy can be used to identify different phases, defects in the structure or chemical variations.

Imaging modes in electron microscopy – During TEM measurements, a thin sample is transmitted by a high energy electron beam of 80 – 200 kV that allows microstructural characterization. Two fundamentally different measurement modes are possible, transmission electron microscopy (TEM) and scanning transmission electron microscopy (STEM) (Fig. 11). In TEM mode (Fig. 11 a + b), the sample is illuminated by a parallel electron wave field. After transmitting the sample, electromagnetic lenses are used to obtain an enlarged image of this electron wave field. In STEM mode, the sample is scanned with a convergent and focused beam, a so-called probe (Fig. 11 c + d). For each position of the probe, the integration of the scattered electrons is registered on the detector below the sample region. A flexible detector setup allows the selection of different contrast or scattering modes for imaging. Switching between measurement modes is possible by changing the currents of the magnetic lenses used to focus the electron beam. (Williams & Carter, 2009).

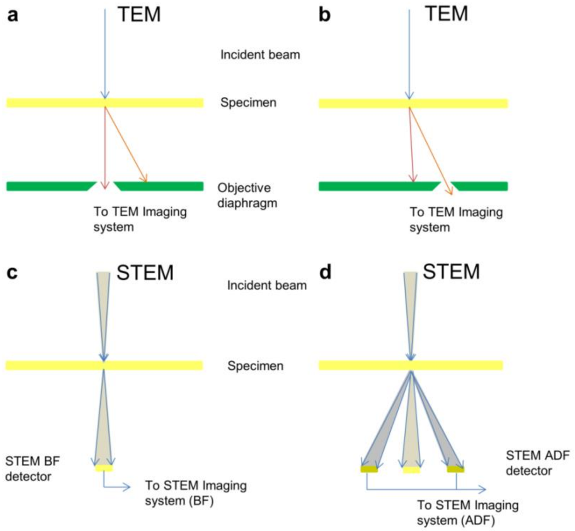

Fig. 11 Possible instrument configurations in TEM and STEM mode. a) TEM bright field. b) TEM dark field. c) STEM bright field. d) STEM HAADF dark field (modified after William & Carter, 2009).

Bright field and dark field imaging - In both TEM and STEM mode, bright field (BF) and dark field (DF) imaging can be used (Fig. 11). In TEM BF imaging, the nondiffracted signal is used to generate an image by placing the contrast aperture central into the optical axis. For the TEM dark field imaging, the contrast aperture is used to select certain areas of the diffracted beam for the image generation. For the analysis of crystalline materials, this will provide additional information on e.g. the crystal orientations of a multi-crystalline material. In STEM imaging, a BF detector uses the less diffracted parts of the electron beam for imaging. In high angle annular dark field (HAADF) mode, a ring detector is used to collect the incoherently scattered electrons.

Contrast in TEM imaging - In general, contrast is generated by the interaction of the atomic nuclei of the specimen with the electrons of the electron beam. Electron microscopy is different from light microscopy, where the interactions of the samples atoms cause a weakening of the light wave's amplitude. The adsorption in TEM depends on the energy loss and is negligible due to the high electron energy and the thin sample. Even though the beam electrons interact with the atoms of the sample, the atom core position does not change. This is called elastic interaction.

Mass thickness contrast **-** The different scattering ability of the atoms can be transferred to an image contrast by removing the strongly scattered electrons from the beam path using an aperture. The flight path of weakly scattered electrons will be almost parallel to the optical axis and therefore pass the aperture. Strongly scattered electrons will hit the aperture plate and are therefore removed from the beam path. Accordingly, strongly scattered sample areas are dark in the resulting image. There are two different contributions to this contrast which are the scattering of the electrons within the specimen and the absorption of scattered electrons at the contrast aperture.

Diffraction contrast **-** In crystalline samples, different scattering of the electrons can also be caused by diffraction. In the case of a polycrystalline material with differently oriented grains, the different crystal lattices would confine different angles with the incident electrons. Whenever Bragg's law is fulfilled by the angle between lattice planes and the electron incident direction, diffraction maxima of high intensity are produced. Accordingly, these scattered electrons will be removed by the aperture from the beam path and the corresponding grains will appear dark. This contrast is used to distinguish crystallites of different orientations or crystal structure in electron microscopic images.

High resolution imaging using phase contrast **–** The phase contrast can be utilized to obtain contrast from a sample where neither a mass thickness contrast exists nor the orientation is different within the observed area. This contrast occurs because the plane electron wave which traverses the crystal will be phase-modulated by the periodicity of the crystal. The difference between two diffracted waves is recorded and provides the phase contrast which can be used for an image generation. It is therefore possible to distinguish between positions of atom columns and areas between atom columns. Further explanation about high resolution TEM imaging can be found in Williams & Carter (2009) and Thomas & Gemming (2013).

Electron diffraction - In addition to the images in real space, the observation of the corresponding focal plane in reciprocal space is possible in both TEM and STEM mode. This direct correlation of images in real and reciprocal space is a remarkable capability of TEM analyses. The elastic scattering of the electrons from the incident electron beam by a crystalline material is concentrated in sharp peaks, the Bragg peaks.

In order to be able to observe sharp peaks, the Bragg conditions have to be fulfilled, which are:

$$n \times \lambda = 2 \times d \sin\frac{\theta}{2} \tag{15}$$

Where n is an integer, λ the wavelength of the incident electron beam, d the distance between two lattice planes and θ the angle between the incident wave and the lattice plane. For electron microscopy, the angle θ is very small and can therefore sin θ/2 equals θ/2:

$$n \times \lambda = 2 \times d\frac{\theta}{2} \tag{16}$$

(Williams & Carter, 2009; Thomas & Benning, 2014; Egerton, 2016)

Analytical possibilities in TEM - The previously described imaging and contrast modes are mainly based on the elastic interaction between the atoms of the sample with the electron of the electron beam except for HAADF contrast imaging. Elastic interactions are interactions without energy loss. Inelastic interactions with energy loss are often element specific. This means that the resulting energy loss will vary depending on the element the electron is interacting with. This allows a chemical analysis with a nano-meter resolution which is possible in HAADF STEM contrast. Further use of these inelastic interactions is taken by energy-dispersive X-ray spectroscopy (EDX) and electron energy loss spectroscopy (EELS). Furthermore, the acquisition of energy filtered TEM images is possible. EDX uses the characteristic energy that is released during the interaction of a source of X-ray excitation, i.e. the electron beam and the sample. For EELS, the energy loss of the electrons undergoing inelastic scattering is used for elemental mapping. In contrast to EDX characterization in SEM, TEM/STEM-EDX characterization offers a higher spatial resolution of the analyzed area. In SEM, bulk samples are analyzed, which therefore leads to large interaction volume within the sample. In TEM, the sample is in the shape of a very thin lamella and therefore the interaction volume is much smaller.

Transmission electron microscopy of minerals - Previously, electron microscopy has been used to study defects and microstructure of both undeformed and deformed minerals. TEM characterization studies of minerals are available on quartz, wollastonite, plagioclase feldspars, carbonates, olivine, pyroxenes and perovskites (McLaren, 2005). Moreover, some studies about TEM characterization of radionuclide containing material such as spent nuclear fuel are available (Van den Berghe et al., 2008; Ray et al., 1992). However, no studies on the characterization of radioactive sulfate minerals with electron microscopy were performed so far. Most TEM characterization studies on barite are focused on the precipitation mechanism of barite or the inhibition of this precipitation (Ruiz-Agudo et al., 2015; Bahl et al., 2014; Freeman et al., 2006; Gonzalez-Munoz, 2003).

2.6.2 *Atom Probe Tomography (APT)*

The local electrode atom probe (LEAP), is a combination of a field ion microscope and a mass spectrometer. The main components are the local counter electrode, the multi-channel plate and a position sensitive detector (Fig. 12) Field ion microscopy is based on the principle of field evaporation. Field evaporation occurs when a sufficiently high electric field is present to overcome the bonding of the surface atoms, so that they can be evaporated. In APT, the atoms are removed successively from the apex of a needle-shaped (<100 nm radius) specimen in a controlled way. An electric field of > 10 V/nm is required so that the field evaporation causes the ionization of the surface atoms in the sample. The electric field at a surface can be estimated based on the following equation:

$$F = \frac{V}{k_f \times R} \tag{17}$$

Where F is the electric field induced at the apex of the tip. The tip has a radius of curvature; R. k_f is the field factor. It is a constant based on the attributions of the tip shape and its electrostatic environment (Gomer, 1961). The setup of a local electrode atom probe is presented in Fig. 12. The complete system works under high-vacuum conditions. The specimen is cooled to a temperature of ~50 – 100 K, reducing the movement of the atoms in the tip and also minimizing the diffusion of atoms on the tip during the measurement. A standing (DC) electrostatic field is applied to the tip and pulses are used to trigger the field evaporation. These short pulses (<1 ns) can either be voltage or laser pulses.

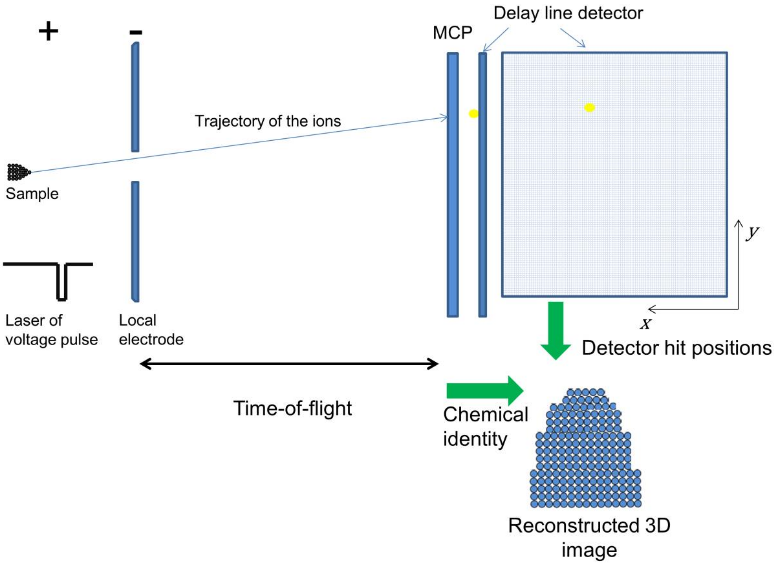

Fig. 12 Schematic overview of a local electrode atom probe (LEAP) microscope.

The barrier of field evaporation can be passed by either of them according to the following equation expressing the evaporation rate Φ_{evap}, which can be written as an Arrhenius law (18):

$$\Phi_{evap} \propto \nu_o \exp\left(-\frac{Q(F)}{k_B T}\right) \tag{18}$$

Where $Q(F)$ is the field-dependent height of the barrier, k_B is the Boltzmann constant and T is the absolute temperature [K]. The vibration of the atoms on the surface caused by thermal agitation is attributed by ν_0. The electric pulses lead to a higher field which increases the field evaporation rate whereas the laser pulse increases the temperature causing a higher field evaporation rate.

After the atoms are evaporated of the surface, they are ionized and fly onto a delay line detector. The flight time of the ions is measured. Additionally, the positions of the atoms are detected by a position-sensitive detector which provides a ~10^6 fold magnification. Accordingly, the resolution of APT is in the sub nanometer regime. Four different type of information are necessary to enable a 3D reconstruction of the specimen: the x, y and z coordinate of the detected ion and its chemical identity. The hit position of the incoming ion is detected and its position in the specimen is calculated by a back projection onto the specimen surface by an algorithm. This gives the x and y coordinates. The time-of-flight provides the mass to charge (m/n) ratio. Based on the m/n, the chemical identity can be determined. The evaporation sequence in combination with the ionic volume based on the m/n provided by ToF determines the z coordinate. The 3D reconstruction of the elemental distribution then is available for further analysis (Gault et al., 2012).

Sample preparation for APT characterization – For the APT analysis, a sample in the shape of a very sharp needle with an apex diameter of 50 – 100 nm is needed in order to enable the field evaporation of the atoms (Kelly & Larson, 2012). Nowadays, focused ion beam preparation can be considered the standard preparation approach. A wedge in the shape of an elongated prism is extracted from the bulk sample by ion beam milling and then attached to a micromanipulator. Subsequently, the wedge is transferred and mounted to a support holder, e.g. Si microchip coupon as commercially available by Cameca (Fig. 13 a), and then fixed by ion beam metal deposition of precursors. This sample part is then transformed by annular ion beam milling into a sharp needle (Fig. 13 b). Two properties of the APT tips are important for the sample preparation and the 3D reconstruction, (1) the radius of curvature, R, and (2) the shank angle, α (Fig. 13 c) (Gault et al., 2012).

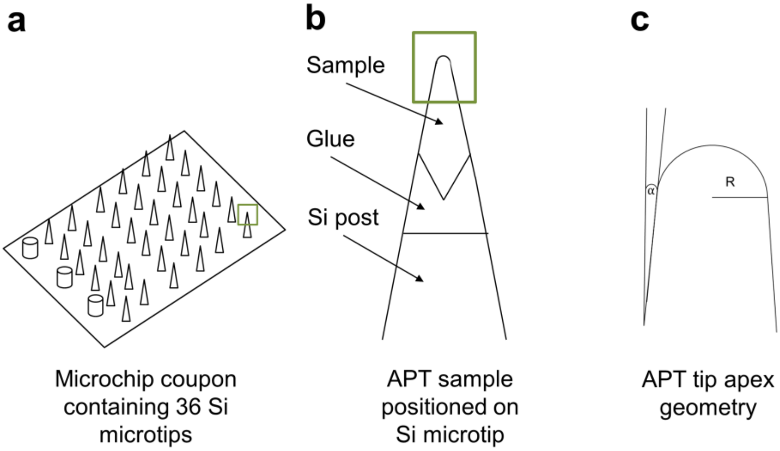

Fig. 13 APT sample geometry. The microchip coupon (a) contains several Si microtips (b) on which the samples are attached. The tip apex geometry (c) comprises the radius of curvature, R and the shank angle (α).

APT characterization of minerals - A brief summary of mineral characterization studies with APT will be presented here sorted by Mohs hardness. The characterization of rather hard minerals, e.g. zircon, is reported more frequently compared to analysis of soft minerals. Several studies on rather hard minerals as zircon (hardness on the Mohs scale: 7.5) (Valley et al., 2014; Valley et al., 2015; Piazolo et al., 2016; Cairney et al., 2015) were published. Furthermore, oxide-containing ceramics were analyzed by APT as well (Chen et al., 2009; Diercks et al., 2014). Recently, a study on arsenopyrite (hardness on the Mohs scale: 6 to 6.5) was conducted finding nano-clusters of gold (Fougerouse et al., 2016). Several studies were as well published on chiton teeth and mammal teeth consisting of apatite which has a hardness of 5 (Gordon & Joester, 2011; Gordon et al., 2012). Recently, APT characterization of human dental enamel revealed Mg-rich amorphous calcium phosphate regions (La Fontaine et al., 2016). In a study of Perea et al. (2016) the location of aluminum in zeolite was determined whereas Schmidt et al. (2016) analyzed different carbon isotopes within zeolites. Depending on the composition, the hardness of zeolites is between 5.5 and 3.The only APT characterization of a mineral with a similar hardness as barite was carried out on calcite (Mohs hardness: 3) (Perez-Huerta et al., 2016). The publication of the APT characterization of carbonate mainly concentrated on the feasibility of the measurement itself. In addition to these few studies, a study on uranium-oxidation analyzed by APT was recently published (Martin et al., 2016).

In the available literature, there are no previous studies on the characterization of barite with APT. The characterization of insulating materials as minerals is a relatively new application of APT. Therefore, every new mineral measured with APT requires the adaption of measurement parameters.

2.6.3 Correlated microscopy: Combination of APT and TEM

APT offers a chemical analysis at a very high resolution which is equally sensitive for all elements. Complementary, TEM provides structural information with highest resolution. Chemical analysis in TEM is also possible, but the commonly used techniques EELS and EDX do not provide a similar resolution as APT. Furthermore, both methods are not equally sensitive towards all elements.

Therefore, the combination of the complementary methods APT and TEM is the best option providing access to the chemical composition as well as the crystal structure. Performing both APT and TEM analyses on the same APT specimen enables a direct coupling of the structural and chemical information. Furthermore, the TEM images of the tip shape can provide substantial information for the adjustment of the 3D reconstruction of the APT data.

In the past, several approaches have been used for this correlated microscopy. Gorman et al. (2008) designed a specific jig to fix samples which is not commercially available. In 2012, Felfer et al. developed a special holder based on a TEM sample retainer that can be used for moving the grid with the attached tips between FIB, TEM and APT. This holder can be used for wire and disk-shaped samples, but it only fits into certain Jeol TEM holders which limit the analytical capabilities in the TEM.

Another approach was used by Hartshorne et al. (2014), who developed a method for the analysis of meso-scale features of several micrometers. They transferred the sample into the TEM prior to the shaping of a tip, and then moved it back into the FIB-SEM instrument for the final sharpening.

Recently, the holder developed by Felfer et al. (2012) was modified by Herbig et al. (2015) providing easier sample transfer and a lower probability of specimen breakage during the transfer between the instruments. In conclusion, no solution for an inexpensive approach in correlative microscopy with a double-tilt holder existed. Therefore, an inexpensive approach for correlative microscopy was developed in this work.

2.6.4 FIB Tomography

During a FIB tomography, serial slices of a material are first cut by a Ga^+ ion beam and are then either imaged by the electron or the ion beam. This technique allows the distinction between different phases or bulk defects within the sample volume. Different phases within the sample can be distinguished based on the contrast of the SEM image. In a segmentation step, they are assigned to a certain phase. The images are then combined and for the segmented parts, a 3D volume image can be generated. This not only allows the identification but also the visualization of the three-dimensional distribution of the internal features of a sample. The typical resolution of FIB tomography is between several tens to five nm. Therefore, this resolution is higher than that obtained by X-ray tomography. TEM tomography methods and also APT provide an even higher resolution but these techniques can only be used to analyze a very small sample volume (Holzer & Cantoni, 2011).

The larger sample volume typically analyzed by FIB tomography can be useful for the characterization of geological samples, and was utilized e.g. for the investigation of the porosity of forsterite (De Winter et al., 2009), defects in ceramics ($BaTiO_3$) (Holzer et al., 2004), pores within hydrated bentonite (Holzer et al., 2010), pores in boom clay, (Hemes et al., 2015), or porosity of compacted clay (Garboreau et al., 2016). A recent study on the distribution of porosity in 10 µm size calcite crystals has proved that the application is possible as well to fine grained mineral powders (Chang et al., 2015). No other studies on mineral particle characterization are available.

The FIB tomography offers the possibility to identify the three-dimensional distribution of phases and microstructural features, e.g. defects, within a larger sample volume e.g. within a complete barite particle of 20 µm size. In addition, the morphology and connectivity between pores can be tested.

3 Aim of this work

This work focuses on the mechanism of Ra uptake from aqueous solution into preexisting barite at near-to-equilibrium conditions. Three main questions arise from previously available studies:

- *What is the uptake mechanism of Ra uptake into barite?*
- *What is the role of the barite microstructure during the uptake?*
- *Is the Ra distribution within the solid homogeneous at equilibrium?*

Mechanism of Ra uptake - Previous experimental studies suggested the uptake of Ra and recrystallization of barite by an internal process, e.g. dissolution and reprecipitation. A recent review on stable mineral recrystallization recommends high resolution methods to gain insights into this molecular scale mechanism. Therefore, a state-of-the-art high resolution microscopic approach is used to gain a mechanistic understanding at the molecular level.

Role of the barite microstructure - A sophisticated understanding of the Ra uptake mechanism requires the knowledge about the temporal evolution of both solution and solids. Previous studies investigated the evolution of the solution in detail and provided information about the solid only at equilibrium state. Microscopic observations of this combined recrystallization and uptake process is needed to be distinguished from the general recrystallization behavior of barite at close-to-equilibrium conditions. Solid samples from different points of the Ra uptake and Ra-free reference recrystallization experiments are therefore characterized by using a variety of TEM methods for a description of the mechanism.

Ra distribution within the solid at equilibrium – In previous studies, the uptake of Ra into the solid was observed at equilibrium state. The spatial resolution of this characterization allowed no statement about the homogeneity of the Ra distribution. The observation of a homogeneous distribution at equilibrium would further support the consideration of the $Ba_xRa_{1-x}SO_4$ in the long-term safety assessment. A sophisticated STEM-EDX instrument equipped with four EDX detectors provides higher spatial resolution compared to prior studies for the analysis of the Ra distribution.

4 Materials and methods

The focus of this thesis is the solid characterization from batch barite recrystallization experiments in the presence of Ra. One of the Ra experiments and all Ra-free reference experiments were conducted by Klinkenberg et al. (2014) and Brandt et al. (2015). An additional Ra uptake experiment was conducted by the author prior to her PhD work to obtain solid samples from all stages of the experiment. Solids from different stage of Ra uptake into barite were characterized by a combination of SEM, TEM, FIB tomography and APT. Parts of these methods description were already published in Weber et al. (2016) and will not be referenced separately.

4.1 Batch experiments

The experimental setup of the batch barite recrystallization experiments which were conducted prior this thesis work followed exactly the setup of Klinkenberg et al. (2014) and Brandt et al. (2015) and are summarized in the following.

4.1.1 Barite preparation and characterization

Two different types of barite powders were used in the experiments, Sachtleben barite (SL) and Aldrich barite (AL). The commercially available SL barite is a synthetically precipitated, high purity barite (XR-HR-10 blanc fixe) from Sachtleben Chemie GmbH (Sachtleben, 2015). AL is a commercially available barite from Sigma-Aldrich of very high purity (99.998 %).

A well-defined particle size distribution and morphology was desired for all experiments. SL barite mainly consisted of grains > 10 µm. During the SEM observations particles, a significant < 10 µm, were also observed. These smaller grains were removed and only the coarse fraction of the SL barite was used. In mostly fine grained AL barite, larger particles > 30 µm were present. These particles were removed. A grain size separation was performed based on sedimentation in the Atterberg cylinder on both samples (Hirner, 2000).

After this preparation, the SL barite sample was characterized by a mean particle size of approximately 18 µm whereas the AL barite consisted of grains with a mean particle size of 0.5 µm (Fig. 14) (Klinkenberg et al., 2014). Prior to the experiments, the barites were pre-equilibrated in deionized water for six weeks.

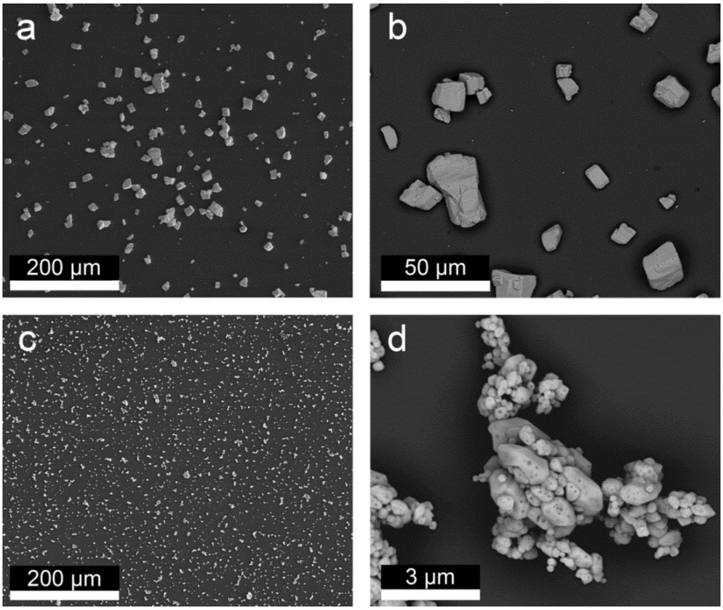

Fig. 14 Barite solid used recrystallization experiments. (a) and (b) show Sachtleben barite. (c) and (d) display Aldrich barite. Reprinted with permission from Elsevier from Brandt et al., 2015, see p. 101 of this thesis for details.

4.1.2 Experimental setup of the batch experiments

Batch recrystallization experiments of barite particles in the presence of $^{226}Ra^{2+}$ were conducted at ambient conditions (23 ± 2 °C). 10 mg of parent barite samples (Fig. 14) (SL or AL) were first equilibrated in 10 mL of 0.2 M NaCl for four weeks. Then, 10 mL of $RaBr_2$ stock solution with a ^{226}Ra concentration of 8.8 x 10^{-4} mol/L were added, resulting in a total solution volume of 20 mL with an initial ^{226}Ra concentration of 5 x 10^{-6} mol/L. This is equal to a solid to liquid ratio of 0.5 g/L. The ionic strength of the experiments was chosen to be close to 0.1 mol/L in order to resemble the repository conditions that are expected at Forsmark, Sweden (SKB, 2011). The experiments were placed on a tilt-roll mixer providing continuous moving of the suspension. A detailed overview of the experiments from which solids where available for this study is summarized in Tab. 2.

Tab. 2 Overview of the available experiments. Selected experiments marked with a diamond (♦) were carried out and discussed in Klinkenberg et al. (2014) and Brandt et al. (2015).

Name	Barite type	Initial Ra concentration [10^{-6} mol/L]	Total duration of experiment [d]
Reference SL ♦	SL	0	1192
SL 1	SL	5	1345
SL 2 ♦	SL	5	898
Reference AL ♦	AL	0	1345
AL ♦	AL	5	883

Sampling procedure - The sampling procedure for aqueous and solid samples was taken from Klinkenberg et al. (2014) (Fig. 15). In regular time intervals of several days, 0.5 mL of the aqueous solution were sampled from the experiment after a settling time of 1 h. In order to ensure complete solid separation, the aqueous sample was subsequently filtered through an ultrafilter (MWCO = 10,000 Da; Advantec, Taipei, Taiwan).

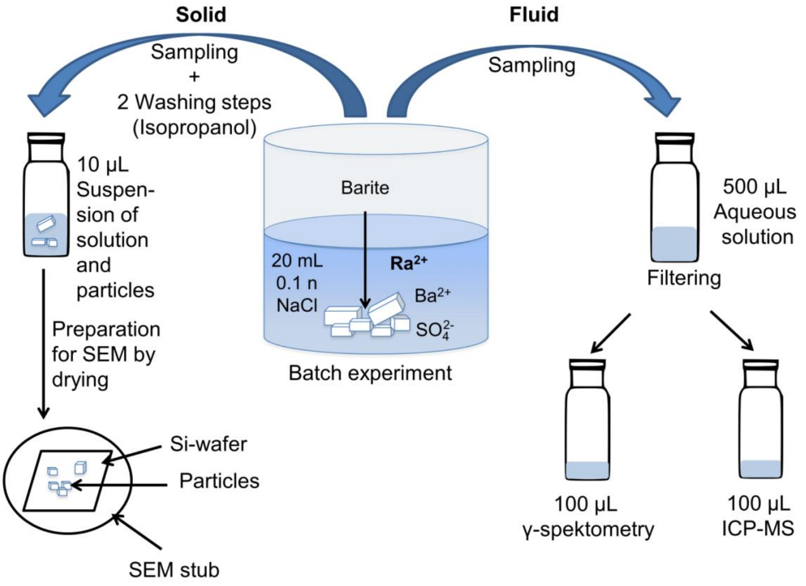

Fig. 15 Experimental setup and sampling procedure for the batch barite recrystallization experiments in the presence of Ra.

γ-Spectrometry - The Ra concentration in the solution was determined by gamma-spectrometry using a N_2-cooled high purity Ge-detector (Canberra, USA). The intensity of the Ra peak at 186 keV was determined using the “Gamma-W” software for

Windows (Version 2.55, Interaktive Spektrum Analyse, Dr. Westmeier, Gesellschaft für Kernspektrometrie mbH) and converted into concentration units (mol/L).

ICP-MS analysis - For the determination of the Ba concentration in solution an ICP-MS ELAN 6100 DRC (PerkinElmer SCIEX, Waltham, USA) instrument was used. The samples were diluted with a factor 1:100 and acidified with 0.1 M HNO_3.

4.1.3 SEM sample preparation and selection of solids for characterization

Solids were collected as a 10 µL suspension (Fig. 15). Then, the solids were washed in two steps with isopropanol to prevent the precipitation of NaCl, $BaSO_4$ and $RaSO_4$ artifacts. The suspensions were dried on a Si-wafer. Prior to FIB preparation, the samples were covered with a carbon coating of approximately 20 nm thickness using a Quorum Q150T E sputter coater (Quorum Technologies Ltd., U.K.) to minimize the charging of the samples during SEM analysis.

The SL barite samples were analyzed prior to the AL barite as the higher average grain size facilitates the FIB preparation. An overview of analyzed solid samples of SL 1 and SL 2 and the according Ra concentrations in solution is presented in Tab. 7 of the appendix. Solids taken from the Ra-free reference experiments were analyzed after 1 day, 126 days, 505 days and 898 days of recrystallization to be able to distinguish between effects of Ra uptake from pure barite recrystallization.

4.1.4 Image analysis of FIB cross-sections

The evolution of macropores within the barite samples was evaluated by image analysis. SEM images of FIB-cross sections were manually converted into binary images of the internal features (Fig. 16). Then, the same SEM image of the particle was manually converted into a binary image of the particle area.

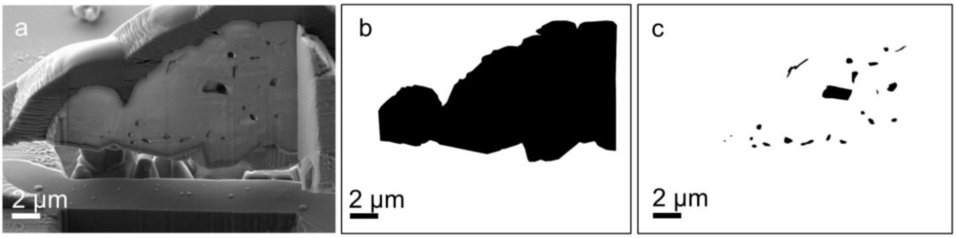

Fig. 16 Image analysis of FIB cross-sections. In the SEM image (a), first the particle are is marked and converted into a binary image (b). Second, the pores are highlighted and a binary image is constructed as well (c).

The particle size analysis of ImageJ was used to determine the areas covered in both images and obtain values for the areas of the particles and the internal features. The ratio of the internal features area to complete particle area was calculated.

4.2 Characterization methods

In the following paragraph, the measurement parameters for APT, TEM, correlated APT and TEM and for FIB tomography are presented.

4.3.1 Atom Probe Tomography (APT)

Prior to this work, no publications about APT characterization of sulfates in general or barite in particular were available. Therefore, the APT operating conditions had to be adjusted to barite. Barite is an electric insulator and has a low thermal conductivity (Horai, 1971), which requires the use of the laser mode in APT analysis.

The APT measurements were performed using a LEAP 4000X HR instrument equipped with a laser of 355 nm wavelength (Kelly & Larson, 2012). The mass resolving power of this instrument is more than 1000 full width half maximum (FWHM) at mass-to-charge (m/n) = 27 for a 100 nm wide field-of-view. The specimens were cooled during the measurement to a base temperature of 50 K. For each measurement, several instrumental parameters had to be modified in order to maintain the maximum specimen yield while keeping the background low. The base voltage was maintained in order to achieve evaporation of 0.002 to 0.005 atoms per pulse. The laser energy was adjusted to 55 pJ. A low pulse frequency of either 100 or 150 kHz was chosen to allow the heavy Ba-atoms to reach the detector within the designated timeframe prior to the next pulse. The Cameca IVAS software version 3.6.8 was applied for the data analysis. To reconstruct the sample volume in a tomographic distribution of the elements from the available time-of-flight data, either the radius of curvature or the threshold for the initiation of electric field evaporation needs to be known (Kelly & Larson, 2012). The threshold for field evaporation can be calculated based on the shank angle. In all measurements, the shank angle was estimated from SEM observations of the respective APT tips for the 3D reconstruction.

60 % of all measured tips fractured during the measurement which was probably due to the presence of macropores inside the tips. However, reasonably large datasets of > 30 Mio. ions were collected.

4.3.1 Transmission Electron microscopy

Basic characterizations as preliminary TEM-BF imaging and SAED were conducted using a Phillips CM 20 microscopy operated at 200 kV. Then, a FEI Tecnai G^2 electron microscope operated at an accelerating voltage of 200 kV was applied to record SAED pattern, TEM and STEM images (ER-C et al., 2016a). For the acquisition of the STEM images a high-angle annular dark-field (HAADF) detector setup was used. The HAADF contrast intensity is proportional to the atomic numbers accumulated in the sample volume traversed by the electron beam for thin samples. Therefore, it provides to a certain degree information about local variations of the chemical composition, the sample thickness and the density (Williams & Carter, 2009).

Most images were collected in HAADF STEM contrast. Diffraction pattern were collected in TEM mode. The information from SAED diffraction pattern obtained in this mode is more straight-forward than from diffraction pattern from STEM due to high complexity of STEM diffraction pattern. Therefore, electron diffraction in TEM mode is more commonly used in general to analyze the crystal structures and was also utilized in this doctoral study.

High resolution analysis of the barite microstructure was performed using a FEI Titan T instrument at 200 kV accelerating voltage (ER-C et al., 2016b). Element distribution maps were obtained by EDX with an FEI Titan G^2 80-200 electron microscope equipped with an EDX system in the ChemiSTEM^{TM} design (FEI Company, The Netherlands). This design comprises four large-area, windowless SDD detectors in an annular orientation called Super-X^{TM} geometry around the sample area (ER-C et al., 2016c). The electron microscope was operated at 80 kV accelerating voltage with a 500 pA probe current. The TEM investigations were particularly challenging because barite exhibited a relatively low stability under the high-energy electron irradiation. It disintegrated within seconds under exposure to the high current densities needed for high-resolution imaging. By adjusting the STEM setup to reduced probe currents of less than 500 pA and applying 80 keV primary electron energy, a longer acquisition of EDX maps up to several minutes was possible.

4.3.1 Correlated microscopy: Electron microscopy and APT

The small diameter of APT tips of 50 – 100 nm makes the APT tip electron transparent in the TEM at 200 kV. Therefore, the correlation of electron microscopy and APT can be used to identify both structural and chemical features at the same tip. The barite sample was prepared as a sharp needle on a modified Omniprobe TEM-grid

(Oxford instruments, U.K.) (Fig. 17) for the correlation of electron microscopy and APT. The middle port of the Omniprobe grid was pre-sharpened by ion beam milling (30 kV/21 nA) using a FEI Helios NanoLab 460F1 FIB-SEM (FEI Company, The Netherlands) (Fig. 17 d). After a standard lift-out procedure, a part of the wedge was fixed with conductive Pt to the port of the TEM grid (Fig. 17 e). Subsequently, the barite chunk was shaped into a sharp needle by applying an annular milling pattern with successively reduced currents (30 kV/0.23 nA to 30 kV/20 pA). A final low kV polishing step (5 kV/4 pA) removed possible amorphization and damage by the Ga^+ beam.

The correlated microscopy was conducted in two steps. First, the tip was characterized with electron microscopy using the FEI Tecnai G^2 electron microscope (FEI, The Netherlands) at 200 kV. HAADF STEM images were collected to improve the reconstruction parameters after the measurement of the tip.

After the STEM characterization, the Omniprobe grid was transferred into a modified TEM grid holder (Zeiss Microscopy, Germany). The TEM-grid holder was modified by trimming the SEM stub pin to a thickness of 2 mm instead of the original 3.2 mm. This modification allowed the insertion of the TEM grid holder into the standard device for sample transfer within the LEAP 4000X HR APT instrument, the puck. Subsequently, the sample was examined using the LEAP 4000X HR (Cameca, Madison, USA) at 50 K base temperature, 55 pA laser power, 0.05% detection rate and 100 khZ pulse energy. The 3D reconstruction based on the HAADF STEM image was performed with IVAS 3.6.9.

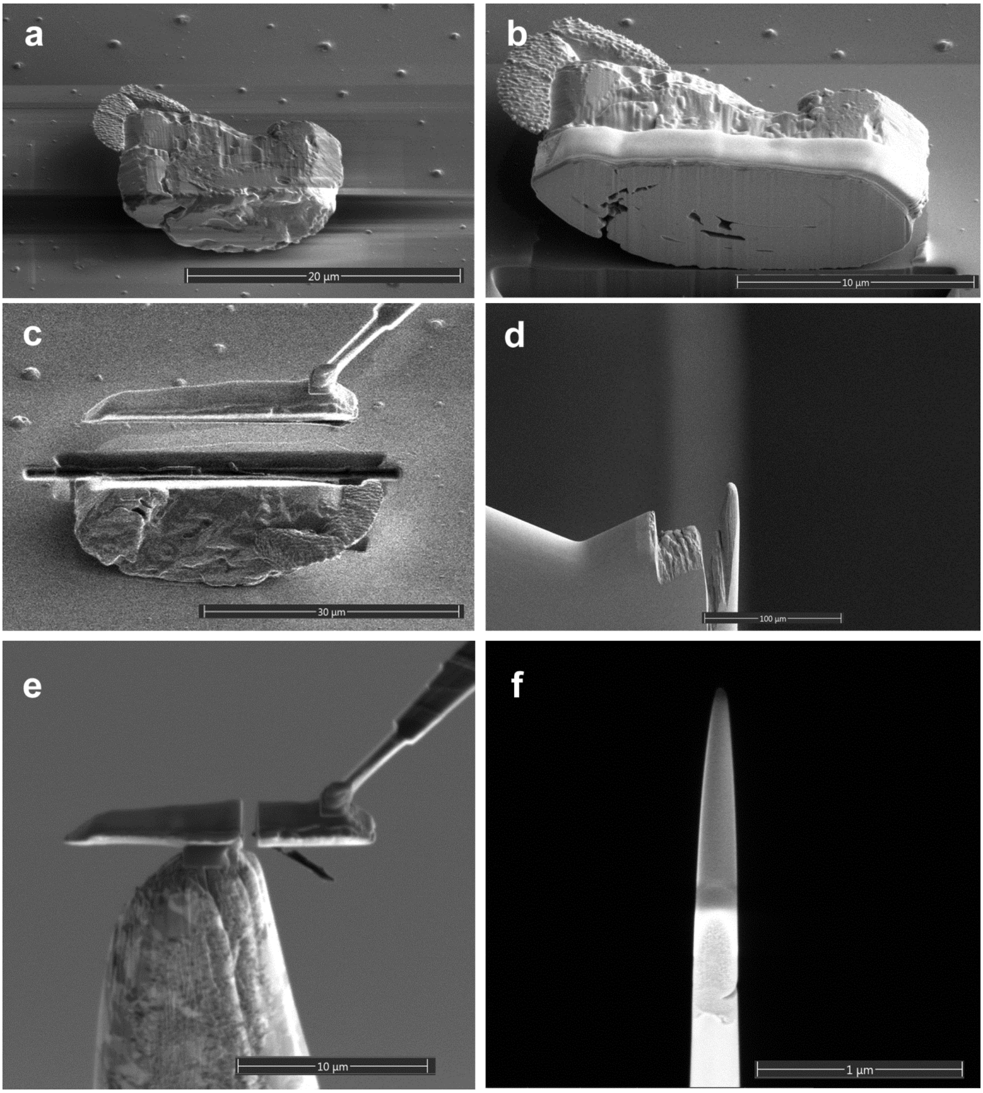

Fig. 17 **FIB preparation of barite tips for the characterization by correlated APT and electron microscopy. The particle chosen for the preparation (a) is covered with a protective Pt layer and a cross-section is cut (b). A wedge is lifted out of the barite (c). The Omniprobe grid was prepared prior to the (d) for the attachment of the barite wedge (e). The final tip shape after the annular milling is presented in (f).**

4.3.1 FIB Tomography

The three-dimensional distribution of macropores within barite particles was addressed by FIB tomography using a FEI Helios NanoLab 460F1 FIB-SEM (FEI, The Netherlands) instrument. Slices of barite were cut parallel to the longest axis of the particle and investigated using secondary electron (SE) images (ER-C et al., 2016d). A Pt-layer of (approximately 10 µm x 20 µm) was deposited using first the electron beam (~200 nm thickness) and second the ion beam (~1 µm) to protect the area of interest of the bulk barite sample during this slice-and-view procedure.

A 30 kV/ 2.5 nA current was set to cut two trenches on both sides of the particle. Subsequently, a third trench from the front of the area of interest was milled to expose the first segment of the slice-and-view section. In total, 734 slices of approximately 20 nm were prepared by ion beam milling using a current of 2.5 nA. Each cross-section was imaged with the mirror detection (MD) mode and by a through-the-lens back-scattered (TLD-BS) detector using a 2 kV/ 0.4 nA electron beam with a pixel size of 7.68 nm.

One challenge in analyzing insulating samples with FIB-SEM tomography is the charging of the sample. Due to the charging, distortion in the image occurs. Sometimes, the impregnation of a sample can reduce the charging and help to analyze the porosity in case of connected pores (Holzer et al., 2004). For the barite particles, this was not possible due to their small size. Furthermore, heating during the impregnation could possibly have causes changes in the internal microstructure. After the completed measurement, the segmentation of the pore space was performed manually.

The SEM images were combined as a stack into a single three-dimensional volume by the tools available in the AVIZO 9.0.0 software package. Subsequently, the pore space was segmented using the same software package for the TLD-BS images.

5 Results and discussion

In the following, the adopted FIB preparation procedures are explained in detail. Subsequently, reference samples taken from the initial barites as well as from Ra-free experiments are compared to determine possible pathways for Ra into the barite crystal volume, to determine the role of the internal barite microstructure during Ra uptake and to explain the evolution of the Ra concentration with time observed in the Ra uptake experiments. Parts of the internal microstructure characterization of the initial barite were already published in Weber et al. (2016). These results will be explained here in more detail without referencing each paragraph of Weber et al. (2016) to it.

5.1 Adaption of FIB preparation to barite samples

The experiments were conducted within a controlled area which also comprises a SEM-FIB instrument. SEM characterization of FIB cross-sections could be easily used as a first step of the internal microstructure characterization. The sample preparation possibilities offered by the FIB instrument enabled further characterization methods. The size reduction due to the preparation also reduced the activity of the prepared sample which made the transport in other facilities on the campus easier.

In total, three different FIB preparation procedures were adapted for the characterization of barite with electron microscopy and APT:

(1) Conventional cross-section lamellae preparation
(2) Plan-view lamella
(3) Needle shaped specimen called APT tips for APT analysis

TEM lamellae were prepared in two different orientations in order to receive three-dimensional microstructural information of the barite. For TEM characterizations, the sample must have a thickness in the nm-scale. The actual required thickness actually required depends on the applied accelerating voltage, the chemical composition of the sample and which features to be analyzed (Williams & Carter, 2009). The barite exhibited a high sensitivity towards the Ga^+ beam. Therefore, special care was used to fulfill the thickness requirements during the FIB preparation. The milling conditions of the different working steps adopted in this study are summarized in Tab. 3.

Different types of FIB instruments were utilized depending on the availability and on the suitability of the equipment for the desired preparation procedure. For the radioactive $Ba_xRa_{1-x}SO_4$ solids, a Zeiss NVision SII N40 FIB instrument located in a controlled area was used. In the separate sections on each preparation procedure, the applied FIB instrument is specified. Where crucial, details on the properties of the FIB instruments are given in the descriptions of the preparation procedure.

Tab. 3 Adapted milling currents for the FIB preparation of barite TEM lamellae. Reprinted with permission from Elsevier from Weber et al., 2016 (see p. 101 of this thesis for details).

Working step	Milling conditions	Sample tilt
Cross-section TEM lamellae		
Cut out of the lamella < 1.5 µm		
Trapezia	30 kV, 300 pA	
Rectangle	30 kV, 300 pA	1.0°
Thinning of the lamella < 100 nm		
Step 1	30 kV, 80 pA	1.0°
Step 2	30 kV, 40 pA	0.8°
Step 3	30 kV, 60 pA	0.6°
Low kV polishing	2 kV, 25 pA	2.0°
Plan-view TEM lamellae		
Cut out of the wedge	30kV, 6.5 nA	
Thinning of the lamella < 100 nm		
Step 1	30 kV, 460 pA	1.5°
Step 2	30 kV, 280 pA	1.2°
Step 3	30 kV, 93 pA	0.8
Low kV polishing	5 kV, 47 pA	2.0

5.1.1 Preparation of cross-section lamellae

After drying of the suspension on the Si wafer, the barite particles were mostly laying on the (001) face. The cross-section lamellae were extracted from these particles perpendicular to the surface. Well-established procedures were applied for this preparation (Gianuzzi & Stevie, 1999; Mayer et al., 2007) using a SEM-FIB instrument. To obtain cross-sections of maximum area, the cross-sections were cut with an orientation parallel to the longest particle axis. A protective layer of either carbon (C) or platinum (Pt) was deposited with a thickness of approximately 3 µm on the surface to protect the area of interest from Ga^+ beam damage. Then, a 1.5 µm thick slice was cut out of the bulk material and attached to the middle post of an Omniprobe TEM-grid (Oxford instruments, U.K.) (Fig. 18 a). Depending on the sample properties, two different attachment positions were used (Fig. 18 b + c).The attachment at the side of the lamella was utilized for stable samples whereas the attachment on top of the middle post was used for unstable, weaker samples.

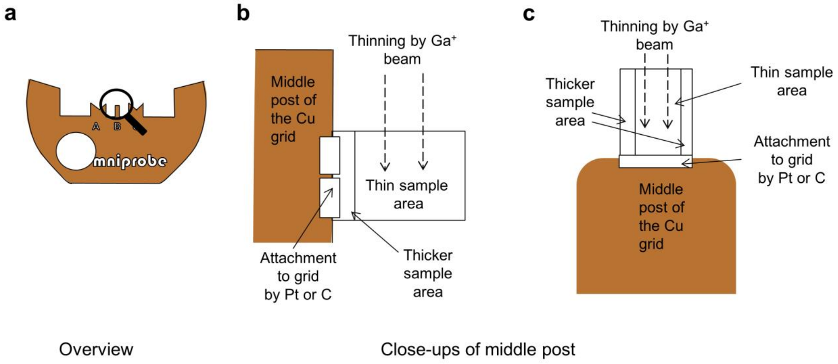

Fig. 18 Scheme demonstrating two ways of fixing the lamella to the Cu omniprobe grid (a): attachment to the side (b), attachment on top of the middle post (c).

After the fixation on the grid, the lamella was thinned. Three different steps with reduced inclination angle and beam current were applied to reach a thickness of < 100 nm (Tab. 3). Then, the preparation was finalized with a low kV polishing to remove amorphization and Ga implantation at the sample surface. Finally, the thinned cross-section lamella had a size of 15 ± 5 µm x 7 ± 5 µm. It was electron transparent in most areas.

5.1.2 Preparation of plan-view TEM lamella

A second lamella orientation was prepared to find out whether the features observed in cross-section lamellae are distributed within the barite particle volume. The orientation parallel to the crystal surface was chosen, which is called plan-view lamella. This preparation procedure requires a FIB with a flip-stage. Therefore, a FEI Helios Nanolab 400S (FEI Company, The Netherlands) dual beam instrument equipped with the necessary flip-staged was applied (ER-C et al., 2016e). In general, the preparation procedure was based on Stevie et al. (1998).

In contrast to the cross-section preparation, in the plan-view preparation procedure a thick wedge is removed from the particle. For this, a protective Pt layer with a thickness of 1 µm was deposited on a selected rectangular surface area of the particle (Fig. 19 a). The selected area of 4 µm x 20 µm defined the target size of the final lamella. Then, a wedge of the barite was cut out by milling rectangular regions on three sides of the previously deposited area (Fig. 19 b). Subsequently, the wedge is connected with Pt to an in situ Omniprobe nanomanipulator (Oxford Instruments, U.K.). The stage, on which the Cu Omniprobe grid was attached, was flipped by 90° and the barite wedge was connected to the grid with Pt (Fig. 19 c + d). Then, two new Pt layers were deposited on a selected area of the wedge in order to prevent the target volume from beam damage and Ga implantation during the final milling steps (Fig. 19 d + e). To shape the sample into a lamella of ~20 nm thickness, the upper and lower parts of the wedge were milled in several steps (Tab. 3). Finally, a low kV polishing step was performed to reduce the damages by the Ga beam like amorphization and Ga implementation.

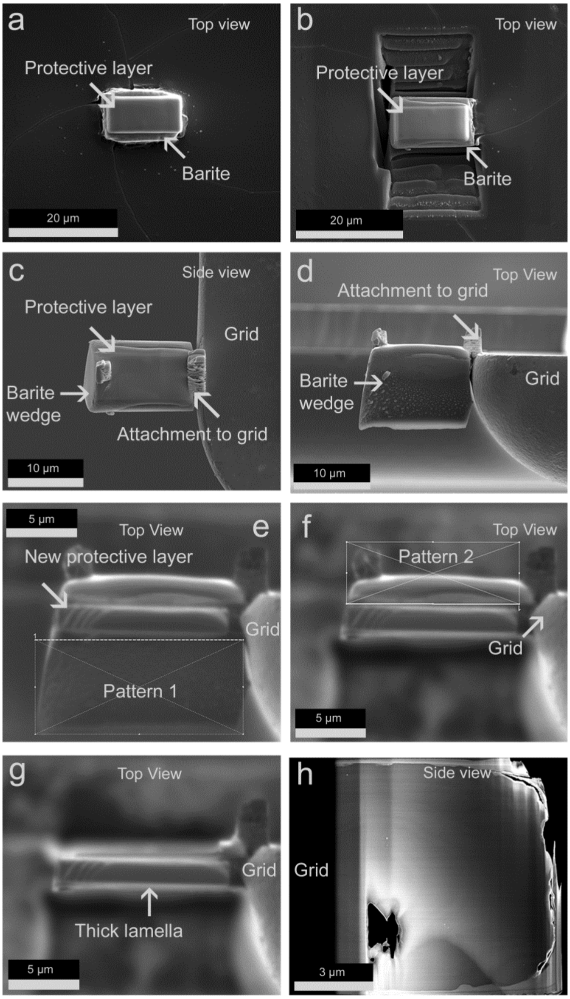

Fig. 19 Plan-view preparation. First, a protective Pt layer (a) is deposited on the barite particle as shown in top view. Trenches are cut out (b) near the barite particle. (d) displays the wedge attached to the grid in side view and the top view is presented in (e). Two patterns are milled as presented by (e) and (f). The thick lamella prior to the final thinning is displayed in (g). The final lamella is presented in (h).
Reprinted with permission from Elsevier from Weber et al., 2016 (see p. 101 of this thesis for details).

5.1.3 Preparation of APT tips

APT tips were prepared using a FEI Helios 600 dual beam instrument. The basic procedures of Miller et al. (2005 & 2007), Miller & Russel (2007) and Thompson et al. (2007) were adopted. In this preparation procedure, the barite particles had to be fixed to the substrate with Pt, similar to the previous TEM lamellae preparation. This was followed by depositing a protective Pt layer of 180-220 nm thickness (5 kV/120 pA) on a rectangular region of interest sized 2 µm x 20 µm. Below this region of interest, a barite wedge was cut out on three sides (20 kV/0.79 nA).

After attaching the wedge with Pt to an in situ nano-manipulator (Omniprobe, Oxford Instruments, U.K.), the final connection was removed (Fig. 20a). Subsequently, the wedge was attached to one of the Si post of a 22-array coupon (Cameca Scientific Instruments, USA) with Pt and 1 – 2 µm thick segments were cut off as displayed in Fig. 20 b. This procedure was repeated until the complete wedge was cut into different parts and distributed over different posts. Then, each wedge was shaped into a tip and sharpened using an annular milling pattern. The inner and outer diameter was stepwise reduced as well as the beam current (30 kV/0.23 nA to 30 kV/20 pA). A variety of beam currents had to be used to shape the sample segments into sharp needles as the segments exhibited different reactions towards the ion beam milling. This behavior already indicated inhomogeneous properties of the barite. The obtained tips had an apex radius of 25 – 40 nm as presented in Fig. 20 c.

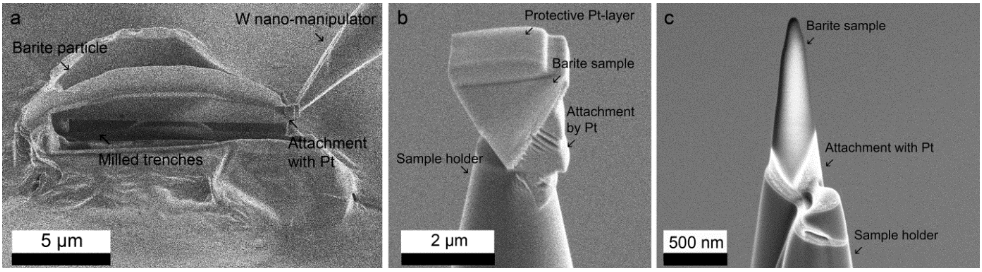

Fig. 20 Stages of the APT tip preparation. a) Milling of trenches and attachment of nano-manipulator to the sample b) sample chunk attached to the sample holder c) sample ready for measurement in APT, final radius is ~70 nm. Reprinted with permission from Elsevier from Weber et al., 2016 (see p. 101 of this thesis for details).

5.2 Internal microstructure of the initial barite

The internal microstructure of the SL barite was extensively characterized because it is the reference to all of the later samples recrystallized in the presence of Ra and without Ra. The internal microstructure of the AL barite was characterized as well to identify whether the observed microstructure of the SL barite is typical for barite in general.

5.2.1 SEM observations of the internal barite microstructure

Eleven cross-sections were successfully prepared from representative SL barite particles (Fig. 21) and SEM images were recorded. In these SEM images, the most prominent feature is a crystallographic oriented system of contrast variations indicating the presence of a layered structure. The nearly euhedral particles exhibited these layers in a systematic arrangement parallel to the outer particle surfaces (Fig. 21). In principle, these contrast variations could result from chemical variations, crystal defects leading to orientation variations or density variations. Density variations such as nano-scale porosity have been described in the literature, e.g. for feldspars (Ruiz-Agudo et al., 2014). Within the error of the measurement, SEM-EDX mapping of the cross-sections indicated no compositional zoning within the error of the measurement. In previous studies on natural barite, a layered structure in combination with a homogeneous barium sulfate composition within the error of the measurement were reported as well (Frondel, 1935; Luedeking & Wheeler, 1891; Parr & Chang, 1935). Another report regarding layered structures inside barite was provided by Jamieson et al. (2016). In their study, the layered structure was identified by optical microscopy to consist of micrometre scale aqueous fluid inclusions (Jamieson et al., 2016).

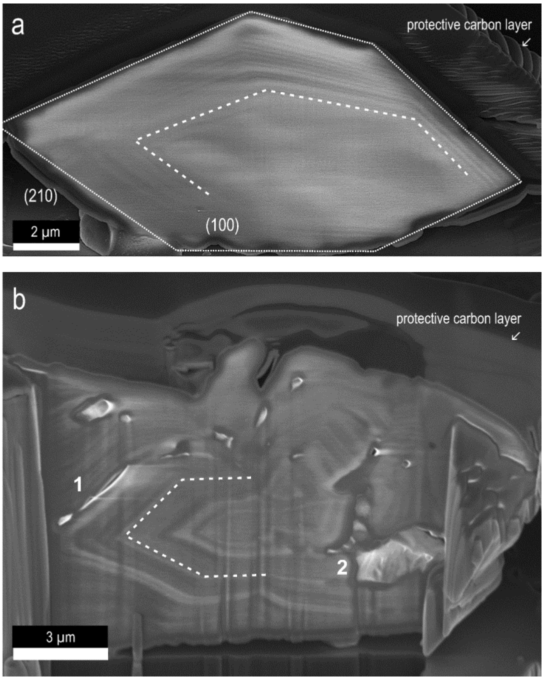

Fig. 21 FIB cross-sections of the SL barite particles. The particle shape is either (a) nearly euhedral or (b) blocky. A solid line marks the outer crystal faces in (a). In both images, the layered structure is indicated by a dashed line. The particle in (a) does not contain any macropores whereas a variety of them are present in (b). Some are elongated (1) tracing the layered structure and others are (2) larger and randomly oriented.
Reprinted with permission from Elsevier from Weber et al., 2016 (see p. 101 of this thesis for details).

In addition to the layered structure, macropores of irregular shape and a few micrometers in diameter were present in most (64 %) FIB cross-sections. About 36 % of the characterized cross-sections did not reveal any macropores. It is possible that the existing macropores were not visualized in the cross-section as a cross-section only represents a 2D image of a 3D particle. Untypically, the macropores were observed in an elongated shape, located along the track of the layered structure (Fig. 21 b). It remains unclear whether they initially contained gaseous or fluid inclusions due to opening of the macropores under high-vacuum during FIB milling. No precipitates were detected in the opened macropores in SEM images or by EDX mappings.
In nature, barite minerals have been reported to contain micrometer-scale fluid inclusions (Bodnar, 2014; Böhlke & Irwin, 1992; Rajabzadeh, 2007; Wilkinson, 2001; Jamieson et al., 2016). These fluid inclusions could potentially correspond to the macropores observed in the SL barite. Correlating natural barite and the synthetic SL barite seems reasonable as both the SL barite and most of the natural barites,

are likely to have formed by precipitation from an aqueous solution under similar conditions. The precipitation of natural barite is often induced by mixing of fluids originating from the alteration of silicate, carbonate, and sulphate minerals in sedimentary, metamorphic and igneous rocks (Hanor, 2000). The micrometre-size fluid inclusions in natural barites are often lens-shaped and contain no daughter minerals (Bodnar, 2014; Böhlke & Irwin, 1992; Rajabzadeh, 2007; Wilkinson, 2001). In addition, Rajabzadeh (2007) reported fluid inclusions matching the cleavage planes of the barite. This feature could possibly correspond to the elongated pores observed here (Fig. 21 b). In summary, these observations may present additional indications that the macropores observed in the cross-sections may indeed have contained a fluid prior the FIB-milling.

5.2.2 Selected Area Electron Diffraction of the initial barite

Electron diffraction patterns were acquired from a very thin TEM lamella in order to determine whether the layered structure observed in SEM could be caused by variations of the crystal orientations. The area containing several layers (Fig. 22 a) exhibits an electron diffraction pattern of $BaSO_4$ in the orientation of the [001] zone axis (Fig. 22 b). The absence of any additional reflexes observed in this pattern suggests a single crystalline, coherent structure without twins, grain boundaries, or other large scale defects. Minor variations of the crystal orientation between the different layers could still have been hidden in the average, large-scale diffraction pattern of Fig. 22 b.

Additional diffraction patterns were obtained from small selected areas of the crystals, ideally just originating from one type of layer. A sufficiently small area selecting aperture selected and SAED pattern were recorded across the layered structure. The sequence of the recorded SAED pattern is displayed in Fig. 23. The circles in Fig. 23 a mark the positions at which the diffraction patterns were recorded. The corresponding diffraction patterns registered at the respective positions are displayed in Fig. 23 b1 - b8. These patterns show crystalline $BaSO_4$ in [001] orientation as well. Through the sequence of these eight patterns, no significant variation of beam excitations and beam positions was detected. Therefore, it can be concluded that the contrast variation in the SEM and TEM images cannot be attributed to variations of the crystal orientation.

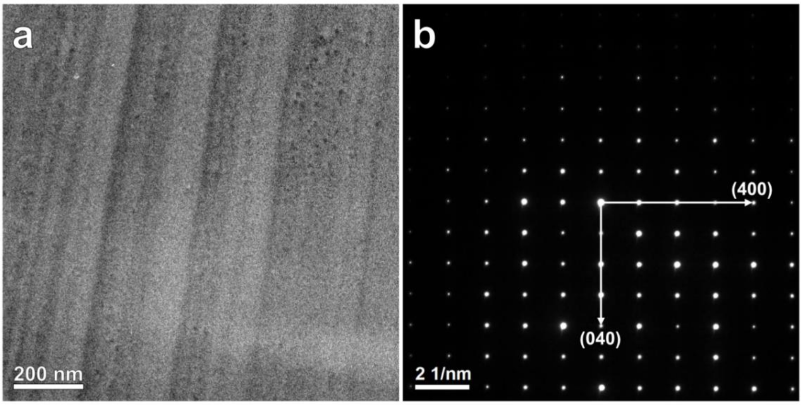

Fig. 22 Electron diffraction analysis. (a) HAADF STEM image of the initial SL barite showing several dark and bright layers. (b) Electron diffraction pattern recorded from a large area of a thin barite lamella.
Reprinted with permission from Elsevier from Weber et al., 2016 (see p. 101 of this thesis for details).

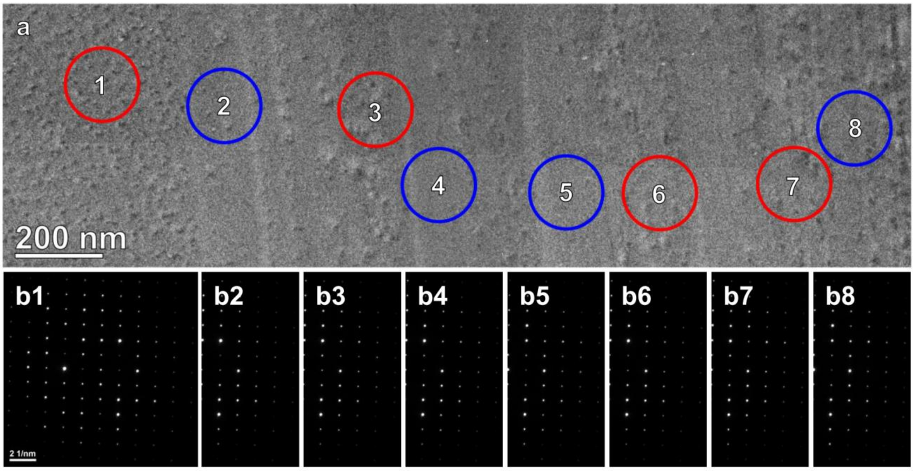

Fig. 23 Selected Area Electron Diffraction experiment. (a) HAADF STEM image of the layered structure with circles marking the positions of a sequence of SAED experiments. Blue circles mark homogeneous brighter layers, whereas red circles mark areas of layers containing a high density of dark spots. (b1) - (b8) electron diffraction patterns recorded from the respective areas marked in (a).
Reprinted with permission from Elsevier from Weber et al., 2016 (see p. 101 of this thesis for details).

5.2.3 Scanning Transmission Electron Microscopy of the initial barite

A HAADF STEM image of a complete cross-section lamella prepared from a blocky particle oriented with the [001] crystal zone axis along the viewing direction is depicted in Fig. 24. The cross-section lamella contains a macropore in its centre. The presence of a macropore in the centre of a barite solid was observed also in other FIB cross-sections. The aforementioned layered structure appears as crystallographically oriented layers of lower and higher intensity. A density of 2 - 3 dark zones per micrometre with irregular thickness and distance can be observed for the strongest contrast variations.

The signal variations were not observed in elemental maps of the same area which were simultaneously recorded. This finding is in agreement with the preceding SEM observations. All TEM lamellae of the initial SL barite exhibited this layered structure in HAADF STEM images independent from the sample thickness. The three-dimensional nature of the layered structure was confirmed by analyzing lamellae prepared in different directions: plan-view and cross-section. Both lamellae showed the layered structure.

HAADF STEM images taken at higher magnification (Fig. 25) indicate the existence of structural differences between the alternating layers on the nanometer scale. Nearly circular regions of low HAADF intensity are visible in different sizes and numbers. They can be interpreted as pores or inclusions of low-Z material in the barite matrix. The bright zones contain larger pores of 10 - 70 nm diameters in a low density, whereas the dark zones comprise a very high density of smaller, few nanometers pores.

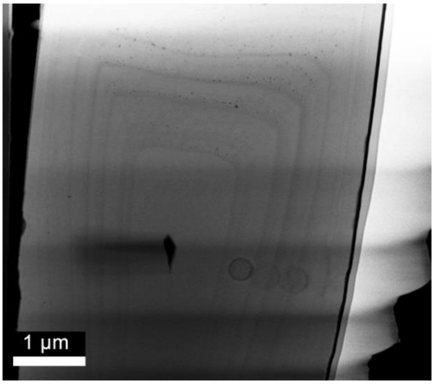

Fig. 24 HAADF STEM image of the SL barite. A layered structure of alternanting low and high intensity is clearly visible. The black region in the center is a macropore. The round features on the right of this pore are due to damage by the electron beam. Inhomogeneous ion beam thinning caused horizontal global thickness variations as well as the curtaining effect on the left side of the macropore.

Reprinted with permission from Elsevier from Weber et al., 2016 (see p. 101 of this thesis for details).

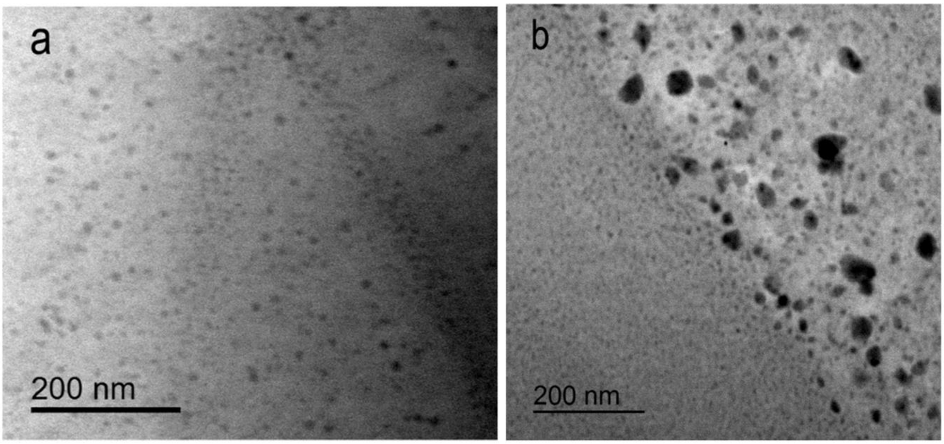

Fig. 25 HAADF STEM images of the initial SL barite. a) The lamella shows an upside down V-shaped layered structure. Thickness variations in the lamella cause the intensity variation from the left to the right side of the image. b) Interface between a dark zone (left) and a bright zone (right) of the layered structure in a barite plan-view lamella. In both images, the bright layer contains larger pores in a lower density, while the dark layer shows a very high density of smaller pores.
Reprinted with permission from Elsevier from Weber et al., 2016 (see p. 101 of this thesis for details).

As there was neither a secondary phase nor variations of compositions and orientation detected by EDX and electron diffraction, the lower HAADF intensity indicates the presence of nano-scale porosity. These pores are distributed across the complete crystal volume. In conclusion, the crystallographic layers of dark and bright intensity apparent in SEM and STEM images are due to variations of the pores' density and size. The electron microscopy data alone cannot deliver enough information to determine whether these pores are empty or contain material of low scattering power.

5.2.4 Atom Probe Tomography of the initial barite

APT characterization of the initial SL barite was conducted to identify the filling of the observed nano-scale pores. Due to the superior chemical resolution even chemical inhomogeneities which are not observable with EDX were detected. The measured mass-to-charge ratio spectra of the SL barite are dominated by a peak at m/n = 69 (Fig. 26). Theoretically, this peak can correspond to two ionic species, $^{138}Ba^{2+}$ and $^{69}Ga^{+}$. $^{69}Ga^{+}$ could originate from the FIB preparation procedure. Therefore, the first thousands ions of the characterization were omitted during the data analysis and reconstruction process. Accordingly, the peak was assigned only to

$^{138}Ba^{2+}$ because the other Ba^{2+} peak intensities were also detected in the expected natural ratios of the Ba isotopes. As the $^{138}Ba^{2+}$ peak at m/n = 69 constitutes 81 - 95 % of the total detected Ba amount in the sample, it was used for the display of the 3D reconstructions in Fig. 27. Furthermore, the mass-to-charge ratio spectra exhibited clear signals of species containing sulfur and oxygen. The presence of H_2O, Na and Cl in minor amounts was also suggested by additional peaks.

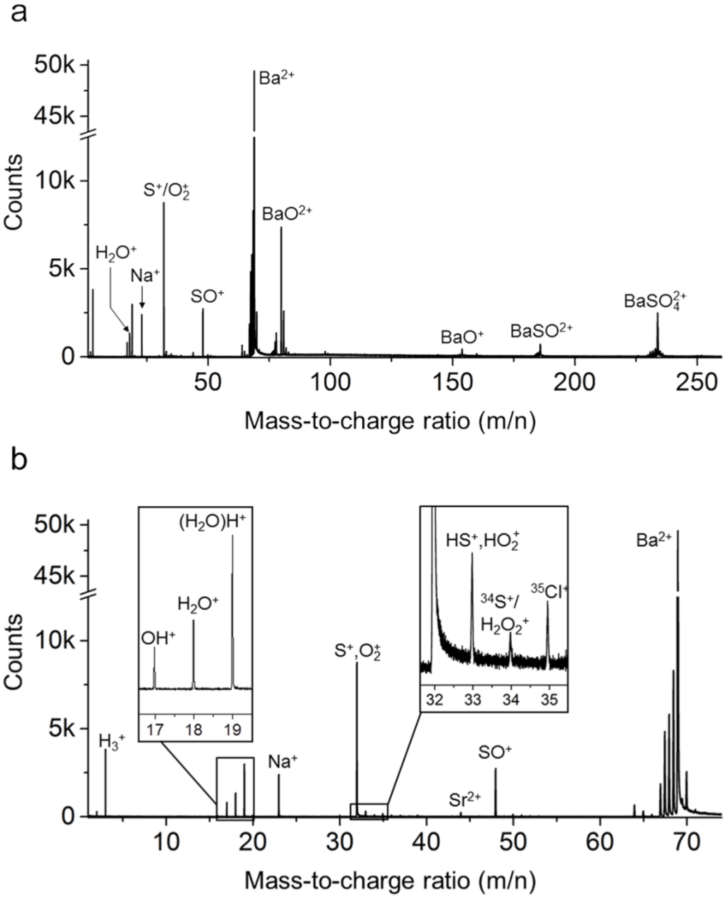

Fig. 26 APT mass-to-charge ratio spectrum of barite. The typical APT mass-to-charge ratio spectrum (a) of the analyzed barite is dominated by the Ba^{2+} peak at m/n = 69. Other strong peaks are marked, such as those of H_2O^+ and Na^+ ions. The lower region of the mass-to-charge ratio spectrum (b) displays two insets showing the variants of ionic water species and the region from m/n = 32 to 35, containing signals of sulfur and chlorine ions.
Reprinted with permission from Elsevier from Weber et al., 2016 (see p. 101 of this thesis for details).

All observed peaks and their assignments to specific ions for both measurements presented here are displayed in Tab. 9 of the appendix. The mass range in both measurements is different due to the application of different pulse rates. The presence of many Ba-containing species, e.g. BaO^+, $BaSO^+$ and $BaSO_4^+$, was observed. The formation of molecules during the measurement of complex materials by APT has been previously reported for other materials as semi-conductors or dielectrics, e.g. in APT characterization of different apatites (Gordon et al., 2012).

The assignment of some peaks to specific ionic species is ambiguous. In the lower region of the spectrum three strong and sharp peaks around m/n = 18 where identified which stem from water species as highlighted by the left inset of Fig. 26 b. The existence of these peaks is interpreted as signals of water being present in the sample. The interpretation that $BaSO_4$ is not the source of oxygen in the water species is based on the anti-correlation of the 3D distribution of these signals with the Ba signal (Fig. 27). This excludes the alternative explanation of a hydride formation of oxygen stemming from $BaSO_4$. In the current APT literature, such hydride formation is discussed as an artifact. This occurs predominantly in the first stages of the APT measurement due to outgassing of the stainless steel vacuum chamber (Gault et al., 2012; Miller & Forbes, 2014). In contrast, in the data evaluated in this study, a very strong peak of hydrogen and water species was observed consistently during the complete course of the measurement. This observation is in a good agreement with other studies where the specimen contained oxygen and hydrogen components (Gordon et al., 2012).

A minor Sr^{2+} peak at m/n = 43 and 44 with a peak height of about 0.5 % compared to the strongest Ba^{2+} peak is also present in the spectrum. This suggests the presence of a low amount of Sr in some of the samples. As $BaSO_4$ and $SrSO_4$ form a solid solution and have a large affinity for each other, this impurity can be observed in synthetic and natural barite crystals (Hanor, 2000).

A severe ambiguity exists for the two major components O and S because the respective two main ionic species S^+ and O_2^+ have the same mass-to-charge ratio of m/n = 32. A second sulfur peak at m/n = 34 with 5 % intensity of the main sulfur signal is expected based on the natural ratios of stable isotopes. Only a small peak was observed at m/n = 34 (Fig. 26). This indicated that the peak at m/n = 32 is mainly due to O_2^+. Another oxygen peak would be expected at m/n = 16 for single charged O^+. This peak may be missing in all of our measurements, probably because of the instrument parameters chosen for this analysis. The sulfur content of the barite is therefore mainly measured as a component of SO_x^{n+} and $BaSO_x^{n+}$ ionic molecules (Fig. 26). The presence of water complicates the solution of these ambiguities by using natural isotopic ratios in this particular material. Water adds additional interferences with the pure elemental signal and a diversity of hydrides may form.

At first glance, the assignment of an ionic species to the peak at m/n = 70 is also ambiguous. Candidates with this mass-to-charge ratio are H_2Ba^{2+}, HGa^+ and Cl_2^+. For the assignment of this peak to chlorine, peaks with a significant intensity at m/n = 72 and 74 would be anticipated due to the expected contribution of 25 % of the ^{37}Cl isotope according to its natural abundance. As these two peaks are not present in the spectra, chlorine was excluded to be the origin of the peak at m/n = 70. The assignment of the peak to HGa^+ is not reasonable, as this component would be expected to be preferentially located close to the surface of the tip sample. No location preference was observed in the 3D reconstruction for the ions at m/n = 70. In conclusion, only H_2Ba^+ remains as a possible explanation. The assignment of this peak to H_2Ba^+ is further supported by the weak peak at m/n = 69.5, which could correspond to HBa^{2+}.

Previously undetected inhomogeneities in the element distribution of Ba, Na and H_2O were observed in the 3D reconstruction of the APT data for the SL barite samples, which are clearly visible in the reconstructions displayed in Fig. 27 a + c. Integrated concentration profiles calculated in the direction of the arrow of the cylindrical sub-volume perpendicular to the layers are presented in Fig. 27 c + d. They exhibit a prominent sequence of alternating layers of anti-correlated Ba and H_2O intensity. The H_2O signal is very low in these profiles, in the order of 1 % of the $BaSO_4$ signal. The partial correlation of the H_2O and Na intensities indicated different concentrations of Na in the individual inclusions. An association of Cl in fluid inclusions with Na is possible, although the Cl signal observed here was too week to produce a significant correlation. The remarkably low Cl yield is likely a result of the very low probability of Cl forming a positively charged ion. The size of the layers of alternating chemical composition observed in the profiles is between 20 and 200 nm, which are coherent with the size of layers of alternating HAADF intensity observed in STEM images (Fig. 25).

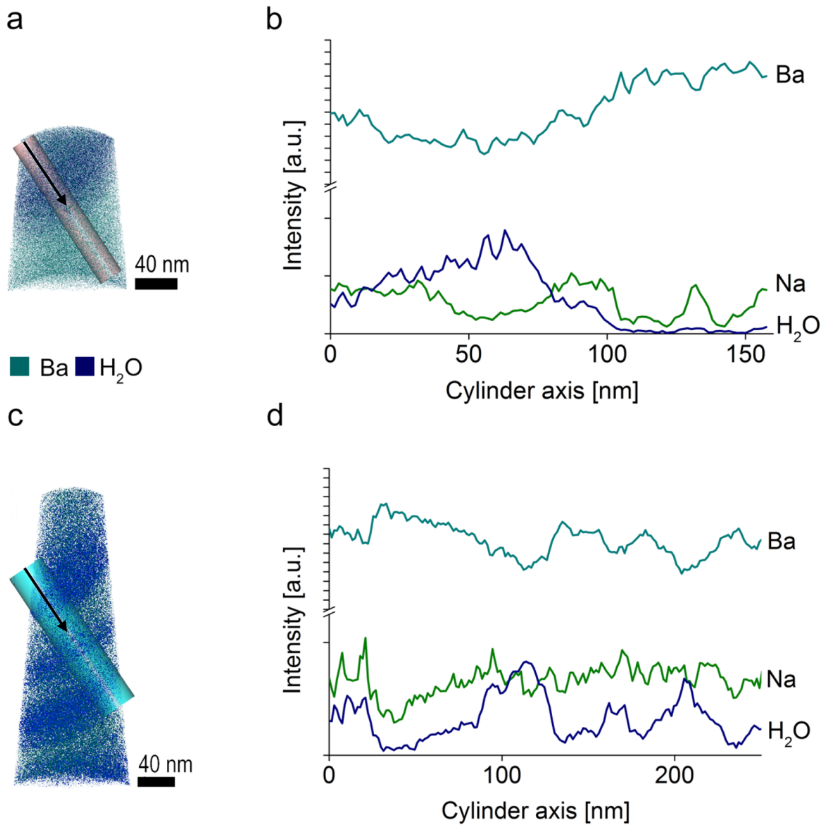

Fig. 27 3D elemental composition reconstructions of two APT measurements of the SL barite. A layered structure due to chemical variation is displayed: (a) and (c) reconstructions with selected Ba and H_2O ions, (b) and (d) integrated intensity profiles calculated with a perpendicular orientation to the layered structure along the axis of a cylinder sub-volume. The profiles indicate an anti-correlation of the Ba and H_2O concentration across the layered structure. The Na signal is at least partially correlated to the H_2O signal in (d).
Reprinted with permission from Elsevier from Weber et al., 2016 (see p. 101 of this thesis for details).

The observed clusters of higher local H_2O concentration in the 3D reconstruction, which match the nano-scale pores observed previously in HAADF STEM images, had a diameter of less than 10 nm. The exact determination of the size is difficult as the change in material and density causes local magnification effects (Vurpillot et al., 2000) which have also been reported, e.g. for gold nanoparticles in arsenopyrite (Fougerouse et al., 2016).

Thus, based on the H_2O concentration variations, it can be concluded that the nano-scale pores are filled with water. In addition to these nano-scale pores, the HAADF image also showed larger pores, which cannot be observed in the reconstructed 3D distribution of elements. The APT analysis of these samples may not have been successful due to the tendency of larger pores to cause the samples to break during the APT analysis. The layered structure detected in HAADF STEM images and the layers observed in APT reconstruction are consistent with the presence of low Z-elements, like Na, Cl and H and O, which would produce a lower HAADF signal in comparison to the $BaSO_4$ matrix. Therefore, regions showing a reduced HAADF intensity in STEM images (Fig. 25) would correspond to regions of higher H_2O as well as to the lower Ba concentration in the 3D reconstruction and in the profiles (Fig. 27). In conclusion, the findings of the STEM and APT measurements are consistent. It is evident that the barite particles contain not only macropores, but also nano-scale pores filled with water and NaCl.

5.2.5 FIB tomography of the initial barite

The connectivity of the observed macropores inside the barite particles was determined via FIB tomography (Fig. 21). So far, the use of FIB tomography is not an established characterization tool for particle characterization as reflected by the low number of publications (e.g. Chang et al., 2015; Winter et al., 2016). For that reason, the optimal measurement conditions were identified first to provide a reliable sample milling and the highest contrast between pores and barite matrix. For these test measurements a random sample of the same material and similar shape can be used. In this study, a barite particle sampled after 127 days of Ra-free recrystallization was used for the test measurements. After the optimal settings were successfully identified, a complete particle of the initial barite was characterized by FIB tomography.

Pores within the test barite surface were observed in SEM images (Fig. 28) indicating the presence of internal pores or defects within the barite crystal volume. Inside the barite, a network of pores was detected in the test FIB tomography. The pores are partially connected and crystallographically oriented similar to what was observed in 2D FIB cross-sections (Fig. 21). Three macropores were also visible on another barite surface depicted in SEM images (Fig. 29 a) which appeared similar to those observed in the test measurement. The observation of these pores may have been related to the presence of an inner macroporosity with a connection to the outside of the particle. The FIB tomography presented in Fig. 29 b (top view of the reconstructed barite particle) and in Fig. 29 c (the side view) pointed to the existence of a network of macropores. The majority of the macropores inside the particle formed a large macropore. Some parts of this large macropores but also some of the other macropores were oriented parallel to the outer crystal surfaces, similar to those observed in the test barite sample. Due to this crystallographic orientation, the walls of the pore space may have exhibited different reactivities, similar to the different reactivities of outer crystal surfaces (Lasaga & Lüttge, 2001; Fischer et al., 2014).

Based on the image analysis of the 2D FIB cross-sections, an average area-based porosity of 2 – 4 % was estimated. After the segmentation of the pore space it is evident that in this particle, the proportion of macroporosity was higher in comparison to the average area-based porosity. Therefore, the particle has a high internal surface which is contact with the bulk solution. This network of macropores may be interpreted as a pathway for Ra into the barite via diffusion in the aqueous solution. The fact that not all macropores are connected to the bulk fluid proposes that the Ra uptake into the barite might not be homogeneous in specific barite particles and might also vary from particle to particle.

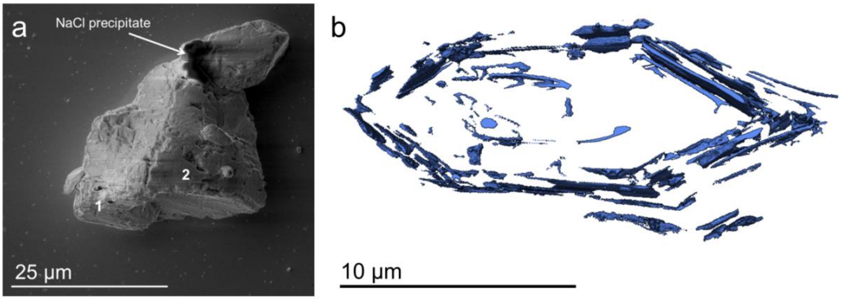

Fig. 28 SEM image of the barite particle used for the test FIB tomography (a). Pores in the barite surface (1) and (2) are visible. The reconstructed pore volume of the particle shows that the pores are oriented parallel to crystallographic orientations (b).

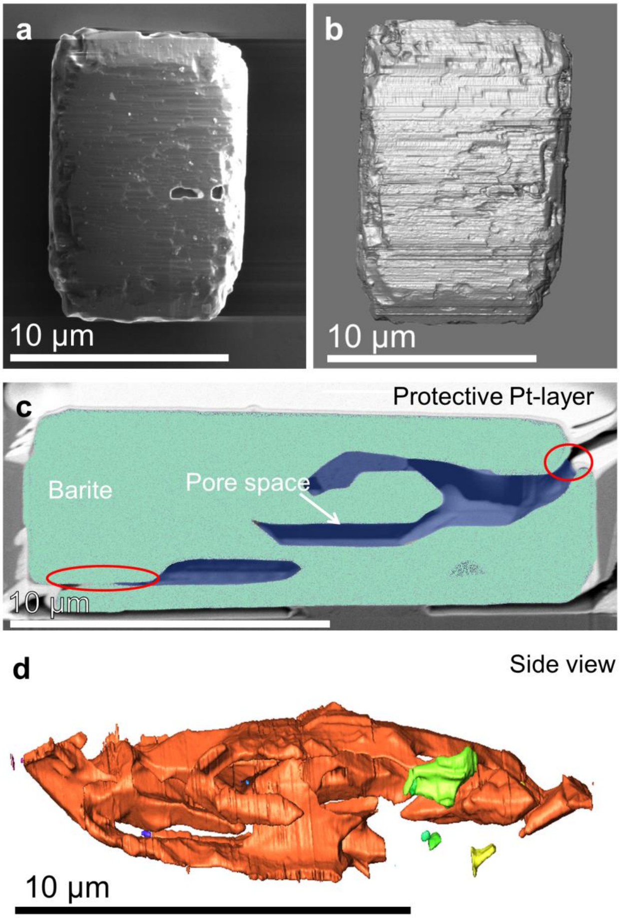

Fig. 29 **FIB tomography of an entire SL barite particle. Three pores are visible in the top view SEM image of the SL barite particle (a) which indicates the presence of internal porosity. The reconstructed particle (b) based on the segmentation of the barite material shows the same shape. In (c), a FIB cross-section is presented. The selected barite material is highlighted in blue and the pore space in orange. The orange circles mark open macropores which connect the internal porosity with the bulk fluid. The segmented pore volume is given in (d); connected pores have the same color.**

About one third of the SL barite cross-sections did not contain any macroporosity. The results of the FIB tomography may not be valid for all SL barite particles. Therefore, the difference in the internal microstructure might be a reason for varying kinetics of the experiments in Brandt et al. (2015).

5.2.6 Correlated microscopy of the initial barite by STEM and APT

The correlation of transmission electron microscopy and APT provides high resolution structural information in combination with high spatial resolution chemical information. The correct 3D reconstruction in APT is based on a detailed knowledge of either the sample shape or the electrical field required for field evaporation of the analyzed material. In this doctoral study, the electrical field needed for field evaporation of barite was not known. Therefore, the reconstruction relied on a detailed knowledge of the sample shape prior the destructive APT analysis. In order to verify that the FIB reconstructions in Fig. 27 are correct, a barite tip was characterized with STEM imaging followed by an APT characterization. The correlated microscopy characterization (Fig. 30) reveals the same layered structure as previously observed during APT characterization of SL barite (Fig. 27).

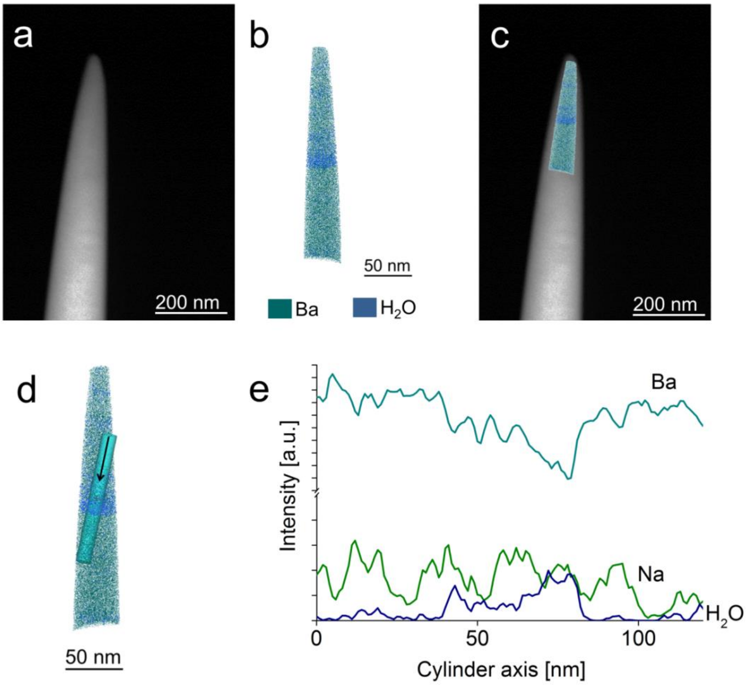

Fig. 30 Correlated microscopy of SL barite. The HAADF image (a) presents the tip shape. In the 3D element reconstruction (b), the layered structure which was observed in the prior APT characterizations of the initial SL reference barite is visible as well. The overlay of the HAADF image and the APT reconstruction is presented in (c). A concentration profile in the direction of the arrow (d) is given in (e) showing an anti-correlation of Ba and H_2O content. The Na-concentration does not correlate to any other components.

5.2.7 High resolution transmission electron microscopy of the initial barite

Stacking faults and point defects can enhance the migration speed of a cation into a solid (e.g. Takamizawa et al., 2016). Therefore, defects in the barite structure could possibly enhance the Ra uptake. To check whether any stacking faults or point defects were present within the initial barite; high resolution bright field (BF) TEM images were obtained using an aberration-corrected TEM instrument. Due to the high sensitivity of the barite towards the electron beam, the barite sample was easily damaged by the electron beam. The disintegration of the barite sample under the electron beam was too fast to perform any aberration correction leading to a reduced resolution of the obtained HR-TEM images compared to the instrument capabilities.

For HR TEM imaging, the TEM lamella has to be very thin. The barite samples were challenging to prepare by FIB, therefore only very few locations on the lamella were thin enough for HR imaging. The regions were located near the edges of the lamella or around the pores. The edges of the particle and the pores are also the areas where the presence of defects is more likely.

The expected atomic order in the orientation of the lamella was calculated (Fig. 31 a) and compared to the observed order in the high resolution BF TEM images (Fig. 31 b). The presence or accumulation of defects in some regions could cause the contrast changes, which might look similar to the layered structure observed in the reference barite. No defects in the crystal lattice were detected.

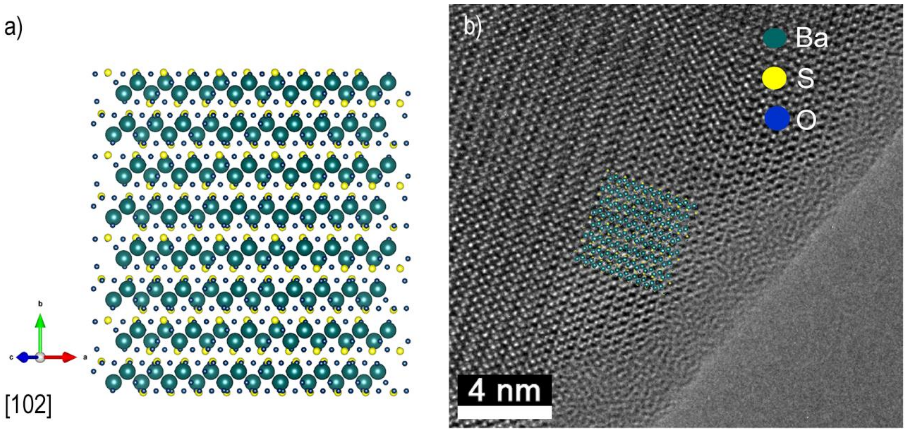

Fig. 31 **High resolution TEM BF imaging of barite. (a) shows the expected order of atoms in the lamella orientation [102] based on the structural data of Jacobson et al. (1998) calculated with the Single Crystal-Diffraction extension of CrystalMaker. In (b), the TEM BF contrast image presents the order of atoms with an overlay of calculated order.**

5.2.8 Possible origins of the fluid inclusions in the initial barite

The observed fluid filled nano-scale pores and macropores could either stem from the synthesis procedure of the barite or may have formed inside during the equilibration treatment prior the use in the uptake experiments. To distinguish between these two possibilities, barite samples were characterized prior the equilibration by SEM analysis of FIB cross-sections and STEM characterization. The analysis of these barites showed a similar internal microstructure as the initial barite after equilibration (figures are presented in the appendix, p. 137). Therefore, it was concluded that the porosity inside the barite samples results from the synthesis procedure. According to the manufacturer, the barite particles were synthesized by a precipitation routine (Sachtleben, 2015).

Different explanations for the existence of the internal porosity are discussed in the available literature. Recently, nano-scale porosity in barite crystals has been observed by in-situ time-resolved TEM investigations on barite crystal growth (Judat & Kind, 2004; Ruiz-Agudo et al., 2015). Based on non-classical nucleation path theory, these studies concluded that the small pores remain from a proceeding growth mechanism including the combination of molecular growth and oriented self-assembly of nano-crystals from a supersaturated aqueous solution. Subsequently, a final internal recrystallization process leaves nanometer size pores, which can be filled by a residual liquid. According to the studies, the size and density of the pores depend on the initial level of supersaturation. In the work presented here, barite crystals of 20 µm size were characterized, whereas Ruiz-Agudo et al. (2015) reported nano-porosity in in particles of a few µm.

Regardless of these non-classical nucleation theories, the defects could also result from a synthesis at a high supersaturation. A synthesis under these conditions is therefore very likely. The homogeneous nucleation of barite, i.e. the direct precipitation from solution, requires very high supersaturation (Kashichiev & van Rosmalen, 2003; Poonoosamy et al., 2016). Furthermore, precipitation from high supersaturation also reduces the synthesis time, which is more cost-efficient. The spontaneous formation of unfilled cores of nm to µm size during crystal growth was previously reported, e.g. in potassium dihydrogen phosphate crystals (Zaitseva & Carman, 2001; De Yoreo et al., 2002). Also, the entrapment of solution during crystal growth has been known as a possible origin of the nano-scale fluid inclusions inside minerals (Mullin, 2001). A sketch of this fluid entrapment process is presented in Fig. 32 a. It takes place by hopper crystal growth which is common during rapid crystal growth (Minkoff & Lux, 1974; Jamveit & Andersen, 1992) (Fig. 32 b).

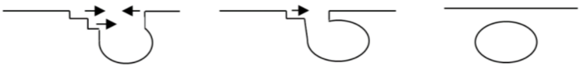

Fig. 32 Literature model of the formation of fluid inclusions during mineral growth. The possible incorporation of fluid inclusions during mineral growth (Modified after Mullin, 2001).

It could also be possible that sodium chloride interacts with the step edge during crystal growth and becomes incorporated as impurity. The incorporation could lead to a defect formation in the form of unfilled cores or nano-scaled pores. The initial NaCl concentration has a strong effect on the step velocities and morphologies. Recently, the study of Godinho & Stack (2015) strengthened this theory further by demonstrating that the overall crystal morphology and growth rate are affected by the NaCl concentration.

5.2.9 Identified pathways for Ra uptake into barite

Different potential pathways for Ra into the barite crystal volume were identified by the application of a variety of high resolution microscopy methods. The barite particles contain macropores of several µm in size, some of which are in contact with the bulk fluid. They are partially interconnected and therefore provide a possible pathway for Ra to enter the barite particles by diffusion within the aqueous solution. Subsequently, Ra could then be taken up into the barite by a dissolution-reprecipitation process from the inside of the barite particle.

In addition, the barite particles contain a layered structure of nano-scale fluid filled pores. Due to the open macropores and the nano-scale fluid filled pores, the barite particles have a relatively high internal pore surface area, which may increase particle reactivity and capability for the uptake of cations. These nano-scale pores inside the barite particles might be ideal nucleation sites for a $Ba_xRa_{1-x}SO_4$ solid solution. Several observations from earlier experimental studies suggest that nano-scale pores might behave differently compared to larger particles, but similar to what has been observed for nano particles (Reviews on this from Stack, 2015; Anovitz & Cole, 2015).

The detailed characterization of the internal microstructure of the barites after recrystallization and a comparison to the internal barites microstructure after Ra uptake is needed in order to identify the details of a dissolution-reprecipitation process (p. 28).

5.2.10 Internal microstructure of AL reference barite

The AL barite was characterized using SEM imaging of FIB cross-sections and TEM. To prepare TEM lamellae from the particles, they were covered with a thick protective Pt layer. This layer did not only prevent Ga^+ ion beam damage but also acted as glue holding the individual particles together. In comparison to the TEM lamellae preparation for the SL barite samples, the AL barite TEM lamellae preparation was complicated due to the small particle size (Fig. 33). Already in the SEM images of the FIB cross-sections (Fig. 33 b), pores inside barite particles were observed. These pores further complicated the FIB preparation as they lead to the curtaining effects (Fig. 33 c). The small particle size and high porosity cause a high instability of the TEM lamella. Therefore, the FIB preparation of the APT tips from the AL barite was not feasible.

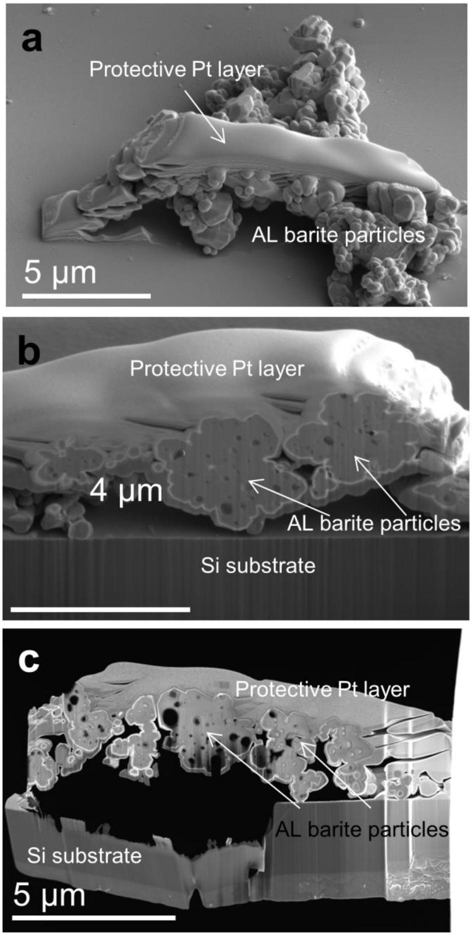

Fig. 33 **FIB preparation of AL barite particles. The AL barite particles were covered with a protective Pt layer (a), which did not only percent ion beam damage but also connected the individual particles (b). To obtain higher stability, the Si substrate was also extracted from the bulk sample and attached to the TEM grid. The electron transparent lamella is presented in (c).**

The HAADF STEM contrast images of the AL barite sample show dark areas within the particles (Fig. 34). EDX spectra show a homogeneous $BaSO_4$ composition indicating that no secondary phase is present within the barite particles. Therefore, the AL barite can be assumed to contain nano-scale pores similar to the SL barite. Inside AL barite, the pores have a size of several 100 nm and are not oriented in any crystallographic direction. The pores inside AL barite are larger than in the SL barite relatively to the particle size. Therefore, it is less likely that they result from the precipitation process. In contrast to SL barite, particles grown together were present in the AL barite samples already at the beginning of the recrystallization experiment.

Here, pores were found along the grain boundaries. This could be due to inclusion of the pores during intergrowth of the particles.

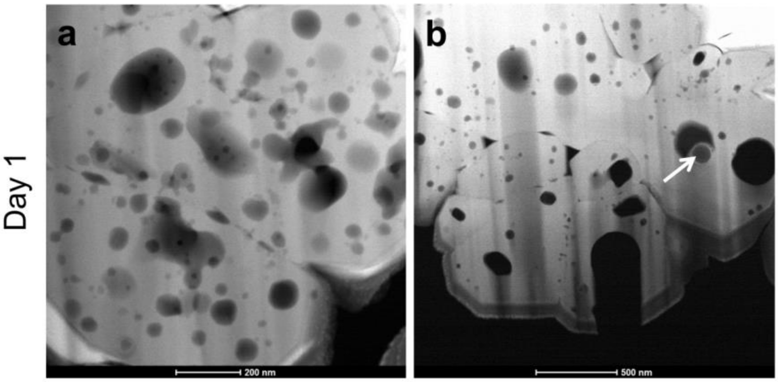

Fig. 34 HAADF STEM characterization of the AL barite. The AL barite contains many internal pores (a), of which some are concentrated along grain boundaries. Some of the pores inside the AL barite are filled with precipitates as pointed onto by the arrow (b).

Clear grain boundaries are visible between the different barite particles. Grain boundaries can act as pathway for fluids to enter a crystal (Jonas et al., 2013; Etschmann et al., 2014); therefore in the AL barite the grain boundaries decorated with nano-scale pores may be the pathway for the Ra to enter the barite.

5.2.11 Changes of the internal microstructure due to barite recrystallization

The effect of different recrystallization times on the internal barite microstructure of SL and AL barites was investigated. SL barite samples were characterized after 127 days, 505 days and 898 days of recrystallization using SEM, STEM and TEM. In addition, APT characterization of the SL barite after 898 days was obtained. The AL barite samples recrystallized for 405 days were analyzed using SEM, STEM and TEM.

SEM observations of changes in the SL barite microstructure - The barite surface roughness was qualitatively observed by SEM imaging. The initial barite exhibited a rough surface with many pores (Fig. 26a,d). Two directions of growth lamellae were observed, which were perpendicular to each other on the {100} and {210} planes. After 127 days of recrystallization, the barite surface began to smoothen (Fig. 26b,e). Less surface pores were present and the different growth lamellae thickened. After 898 days of recrystallization, the barite surface was even smoother (Fig. 26f,c). Less pores and irregularities in the surface were revealed and also the growth lamellas were not as clearly defined as at the beginning of equilibration of 898 days.

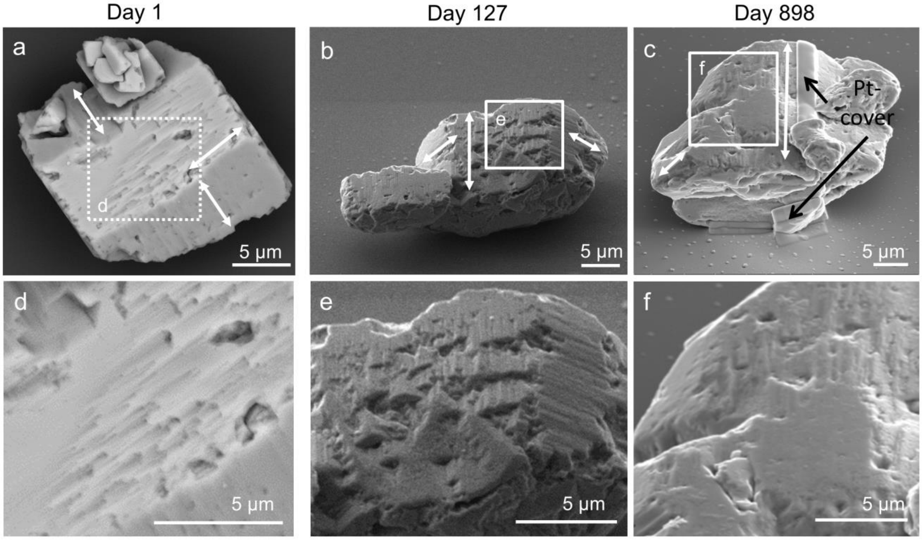

Fig. 35 Smoothing of the barite surface over a recrystallization time of 898 days. At day 1, the SL barite particle surface (a) shows many pores, at higher magnification (d), growth lamellas are visible. After 127 days of recrystallization, the barite surface starts to smoothen (b) and thicker growth lamellas were observed (e). After 898 days of recrystallization (c), the barite surface is partially smooth (f).

The smoothing of the surface can be considered as a free energy driven process of Ostwald ripening.

Similarly to the recrystallization experiments of barite presented here, Heberling et al. (2016) conducted calcite recrystallization experiments in the presence of ^{45}Ca. They concluded that the reduction of the free energy caused a change in surface roughness by recrystallization and Ostwald ripening. In the studies of Curti et al. (2010) and Bosbach et al. (2010), barite recrystallization experiments were performed in presence of a radioactive tracer ^{133}Ba, which offers the opportunity to observe the barite’s recrystallization dynamics. In these experiments performed with the same SL type barite, the complete barite particles recrystallized within 100 days was observed. The barite crystals characterized in the present work recrystallized completely about eight to nine times during the 898 days of duration of the experiment when in contact with ^{133}Ba tracer. Surface smoothening is expected in this context.

Scanning electron microscopy of SL barite FIB cross-sections - No significant changes with time at day 127, 505 and 898 were observed in SEM images of the cross-sections performed on the reference barite samples (Fig. 36 a-c). Macropores were visible inside the barite particles. Some of them were crystallographically oriented (Fig. 36 a + b). The layered structure was still clearly visible in all cross-sections after 898 days. Therefore, it is most likely that the nano-scale porosity is present inside the majority of the barite particles after equilibration. The SEM images of the FIB cross-section obtained from barite particles recrystallized for 898 days showed that the barite particles grew together (Fig. 36 c).

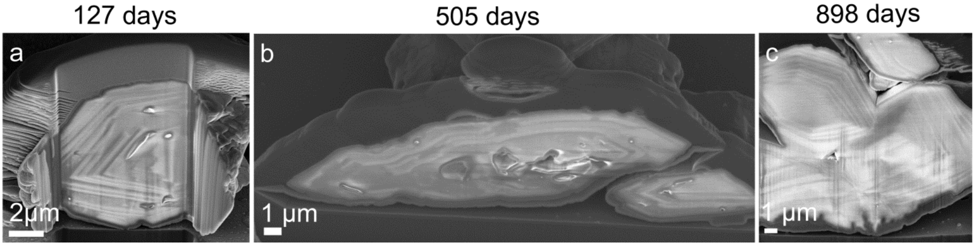

Fig. 36 Cross-section of Ra-free reference SL barite particles after different recrystallization times. The layered structure inside the SL barite is still well visible (a) after 127 days. After 505 days of recrystallization (b), the layered structure is still present as well as internal macropores. The SL barite particles grow together after 898 days (c) while enclosing fluid which forms a new pore.

SEM image analysis of SL barite FIB cross-sections - The evolution of the macroporosity was analyzed in detail by image analysis of FIB cross-sections to identify whether the macroporosity inside the barite changes during recrystallization. By a semi-quantitative analysis of the proportion of area-based porosity of the complete particle area in a cross-section was determined. By this approach, the conversion of the qualitatively easily with the human eye observed change in porosity into numbers was intended. Images obtained from FIB cross-sections from day 1, 127, 505 and 898 were analyzed. The area-based porosity is given in Tab. 4. No error is specified here as the determination is only semi-quantitative and aims at identifying a possible trend and not a quantification of the pore space. No significant changes in the area-based porosity were observed. The average number of pores which was counted remained stable over the 898 days of recrystallization. The maximum area-based porosity which was determined among the analyzed cross-sections indicated the bandwidth of porosity. The minimum area-based porosity is zero porosity for all recrystallization times.

Tab. 4 Evolution of macroporosity inside Ra-free reference barite particles based on image analysis.

Day	Number of analyzed cross-sections	Area-based porosity [%]	Number of pores per particle	Maximum area-based porosity [%]
1	11	1.50	5.9	6.8
127	11	1.70	10.0	5.0
505	5	2.30	6.0	7.2
898	11	2.00	9.8	7.4

Scanning Transmission Electron Microscopy of the SL barite - STEM characterization was performed on barite samples after different recrystallization times (127 days, 505 days and 898 days) in order to identify changes within the internal microstructure at the nano-scale. The layered structure was still clearly visible in most of HAADF STEM images (Fig. 37 a, b, c). No change in thickness of the layers was observed.

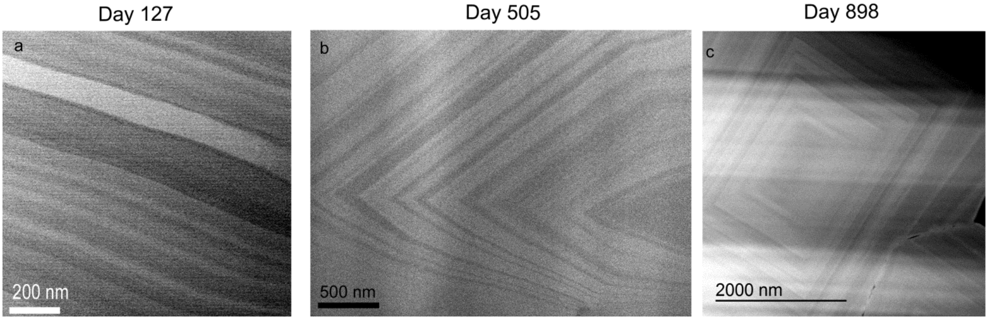

Fig. 37 HAADF STEM images showing the preservation of the internal microstructure during barite recrystallization after 127 days (a), 505 days (b) and 898 days (c) of recrystallization. Horizontal features which are visible in (c) stem from varying thinning strength of the ion beam during preparation.

The lamella of day 898 was prepared from the cross-section in Fig. 36 c. It consists of several particles. In all of these particles, the layered structure was visible. Only in one of the particles the layered structure was not present. During the intergrowth of the particles, a pore of several nm size was formed. A mismatch between the orientations of the particles is visible (Fig. 36 c).

Atom Probe Tomography of the SL barite after recrystallization- An APT characterization of the SL barite reference sample after 898 days of recrystallization was performed to find out if the nano-scale pores are still filled with NaCl and H_2O after recrystallization. During the APT characterization, 34.4 Mio. ions were detected. The mass-to-charge ratio spectrum of the reference SL barite sample recrystallized for 898 days is presented in Fig. 38 a. Similar to the mass spectra of the initial reference barite (Fig. 26), the mass spectrum is dominated by a peak at m/n = 69. This peak can either be attributed to Ga^+ or Ba^{2+} based on the expected natural isotopic abundances. Also in this measurement, the other Ba^{2+} isotope peaks were observed in their expected natural abundances. Therefore this peak at m/n = 69 was fully assigned to Ba^{2+}. The further peak assignment was done based on the consideration explained in the previous measurement. A table of all detected peaks is included in the appendix (Tab. 10). Clear signals of species containing sulfur and oxygen were detected as well. The presence of H_2O and Na was also confirmed by the spectrum. Minor amounts of Sr^{2+} were observed similar to the two previous measurements. In contrast to the initial sample, no peak for chlorine (m/n = 35 for $^{35}Cl^+$) was detected in this spectrum (Fig. 38 b).

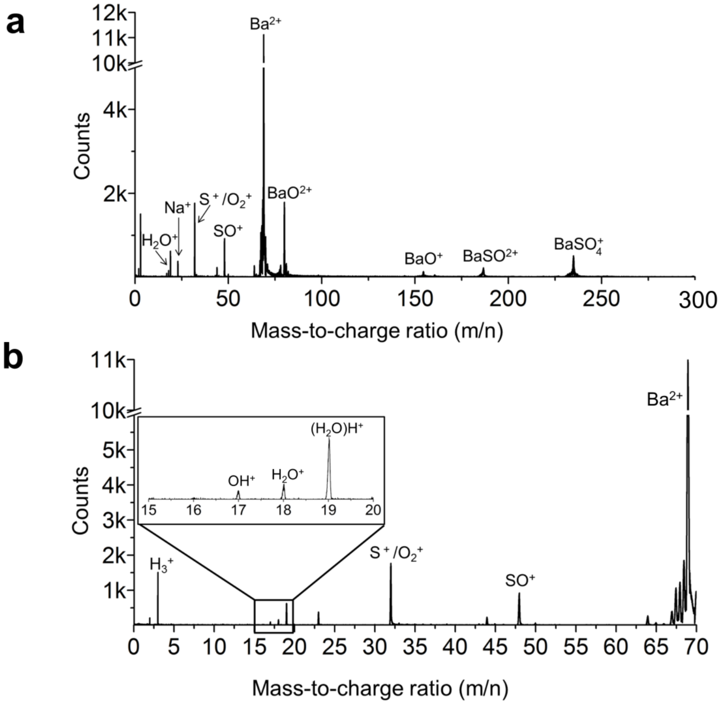

Fig. 38 Mass-to-charge ratio of the Ra-free reference barite after 898 days of recrystallization. The dominant peak is Ba^{2+} at m/n = 69 (a). Other strong peaks are marked. Lower region of the mass-to-charge-spectrum and the magnified inset (b) show water species.

An inhomogeneous distribution of Ba, Na and H_2O was observed within the 3D reconstruction of the APT characterization (Fig. 39 a). An integrated concentration profile of the cylindrical sub-volume in the direction of the arrow is presented in Fig. 39 a. The inhomogeneities, similar to the observations in the reference barite, were also detected. The intensity of the Na and H_2O signal is anti-correlated with the Ba intensity. In this measurement, no layered structure was observed, but two regions with different thickness can be distinguished. Each of these regions is about 50 nm thick. Based on the available APT data it cannot be concluded, whether the thicker regions inside the barite are due to choosing a barite sample with thick layers inside or by thickening of the layers with recrystallization time. However, the TEM data indicates that in average the thickness of the layers stayed the same.

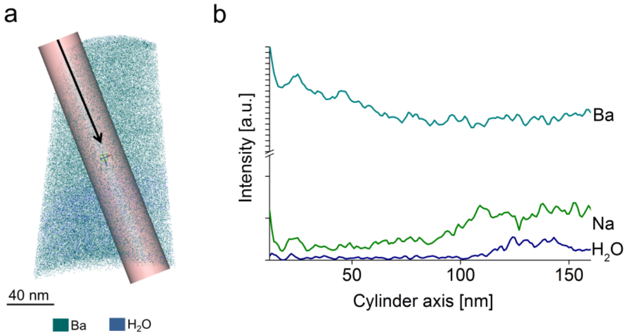

Fig. 39 **APT characterization of a Ra-free barite reference sample after 898 days of recrystallization. The 3D reconstruction of the sample volume (a) shows an inhomogeneous Ba distribution and a H_2O-rich layer. The concentration profile of the cylinder volume in (a) is given in the direction of the arrow in (b) showing clearly a layer with a higher Na and H_2O concentration.**

Scanning Transmission Electron Microscopy of the AL barite – STEM HAADF contrast images were collected of AL barite particles recrystallized for 405 days in a Ra-free solution (Fig. 40). No significant changes of the internal microstructure were observed. The particles formed aggregates similar to the aggregates observed at the AL barite of day 1. Pores of nm-scale size are contained within the complete particles. No pores at the grain-boundaries were observed. Overall the number of pores seemed to be smaller. To support this impression, the analysis of further AL barite particles would be necessary as well as an image analysis similar to the one performed on the SL barite.

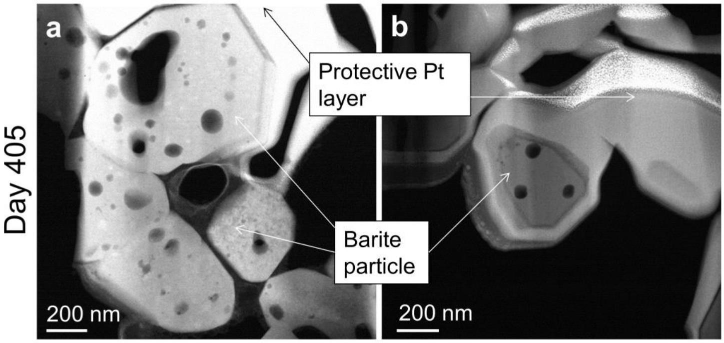

Fig. 40 HAADF STEM images of the Ra-free reference AL barite after 405 days recrystallization. Several particles are grown together (a). Pores are visible within the complete particles. In the upper particle the pores (a) are crystallographically oriented. Other AL barite particles (b) show pores which are not crystallography oriented.

Internal microstructural changes with recrystallization time – Based on the results obtained by SEM, STEM and APT, it is evident, that the layered structure consisting of nano-scale pores is still present within the SL barite samples after 898 days of recrystallization in aqueous solution. Despite the fact that several complete recrystallizations can be assumed based on the ^{133}Ba exchange data of Bosbach et al. (2010) and Curti et al. (2010), the observations made in this doctoral study indicate that the internal microstructure remains the same.

Therefore, it could be either that the ^{133}Ba provides a driving force which triggers the barite recrystallization or that the fluid inclusions remain stable despite several complete recrystallizations. This could be due to a slow recrystallization at close-to-equilibrium conditions, which proceeds layer by layer. A similar process occurs during a pseudomorphic replacement, when the crystallographical information is transferred from one phase to another by this layer-by-layer recrystallization (Ruiz-Agudo et al., 2013 a+b, 2016; Pinto et al., 2009, 2010; Alvarez-Lloret et al., 2010; Morales et al., 2013). Also the AL barite exhibits an unchanged internal microstructure after 405 days of recrystallization which is comparable to the one observed at day 1.

In the literature, several studies report that the barite crystals in the marine environment can be treated as closed systems (Jamieson et al., 2016; Paytan et al., 1996; Zielinski et al., 2001; Widanagamage et al. 2014, 2015). A closed system is by definition a system which has no matter transfer between the inside and the outside of the system but energy transfer. The barite investigated by Curti et al. (2010), Bosbach et al. (2010), Klinkenberg et al. (2014) and Brandt et al. (2015) would be not defined as a closed system as the incorporation of ^{133}Ba and ^{226}Ra was observed in these previous studies (Curti et al., 2010; Bosbach et al., 2010; Klinkenberg et al., 2014; Brandt et al., 2015).

In their study, Paytan et al. (1996) analyzed barites from equatorial Pacific sediment cores and reported no Ra exchange with porewater after the burial of the sediment. Therefore, it was concluded that barite behaves as a closed system in the pelagic layer of the ocean. Prior to the study of Paytan et al. (1996), Church & Bernat (1972) and Borole & Somayajulu (1977) reported Ra, Th, U and Pb contents in barite samples and concluded the rapid exchange between pore water and barite. Authors have also estimated the remobilization rates for these elements after burial. The previous results of Church & Bernat (1972) and Borole & Samayajulu (1977) were attributed by Paytan et al. (1996) to the use of a mild leaching procedure which left an oxyhydroxide coating on the marine barites and therefore may have led to false exchange rates. More detailed studies on dating barite precipitates with Ra isotopes also assumed barite is a closed system (Naehr et al., 2000; Noguchi et al., 2004; Zielinski et al., 2001; Griffith & Paytan, 2012).

A recent review on stable mineral recrystallization in aqueous media discussed the missing thermodynamic driving force during mineral recrystallization (Gorski & Fantle, 2016). Furthermore, the authors suggested the detailed characterization of the solids by high resolution methods to identify subtle changes within the recrystallized mineral phases.

5.3 Changes in the internal microstructure due to Ra uptake

Solid samples from previous experiments on Ra uptake into barite conducted by Klinkenberg et al. (2014) and Brandt et al. (2015) were available for detailed microscopic characterization. An additional Ra uptake experiment was started in 2012 by the author in preparation of this PhD study. This experiment is called SL 1 and the experiment by Brandt et al. (2015) and Klinkenberg et al. (2014) is called SL 2.

A typical evolution of the Ra concentration in solution was recognized (Fig. 41). Three stages were assigned to the Ra uptake processes based on the uptake kinetics (Brandt et al., 2015). These uptake stages depend on the Ra concentration in solution and not directly on the duration of the experiment. Klinkenberg et al. (2014) concluded that the replacement takes place by an internal exchange. This is further elaborated by Brandt et al. (2015), where a dissolution-reprecipitation mechanism was proposed. The most reliable way to identify an internal mechanism is by analysis of the internal microstructure.

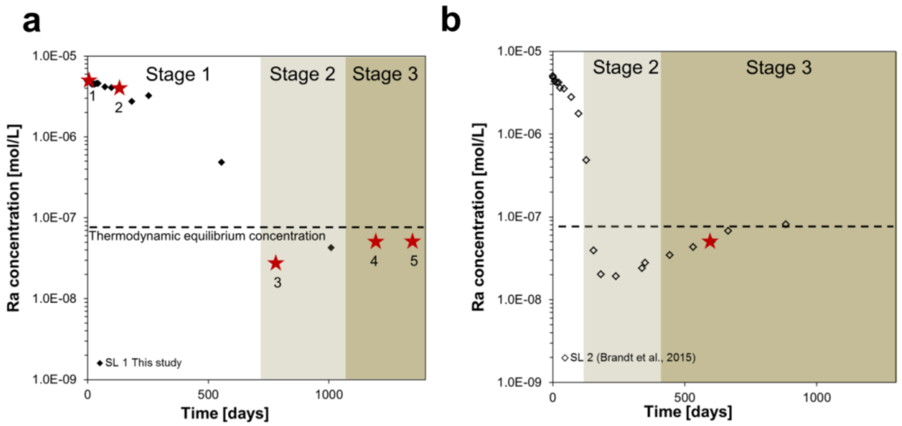

Fig. 41 **Different stages of Ra uptake for SL 1 and SL 2. (a) shows the analyzed samples from experiment SL 1. The black diamonds mark the available samples; red stars indicate the analyzed samples. (1) is sampled on day 1, (2) at day 126, (3) at day 779, (4) at day 1192 and (5) at day 1345. Note that only SEM characterization of FIB cross-section was performed on the samples of (5). (b) presents the analyzed samples of SL 2. The empty diamonds highlight the available samples, the red star specifies the analyzed sample (day 602).**

Barite solids samples from each stage were characterized by SEM imaging of FIB cross-sections, TEM, STEM, SAED and STEM-EDX. For each sampling day, at least two TEM lamellae were prepared and analyzed. Depending on the experiment; the assigned stages of Ra uptake have different durations. This was interpreted to be related to kinetic effects, e.g. the induction time for nucleation (Brandt et al., 2015). Three stages in uptake kinetics can be distinguished in the evolution of the aqueous Ra concentration with time as depicted in the Fig. 41 a + b. In the first stage a drop in the Ra concentration is observed. In some point Ra concentration in the solution becomes lower than the thermodynamically defined equilibrium concentration (stage 2). By the end of the stage 2 the Ra concentration in solution reaches thermodynamic equilibrium again and remains constant over the rest experimental time (stage 3). An overview of all analyzed samples, corresponding Ra-concentration and analysis methods is presented in Tab. 5.

Tab. 5 Overview of all analyzed samples from Ra uptake experiments.

Sample	Day	Ra concentration in solution [mol/L]	Stage	Analysis method
SL1	1	4.90E-06	1	SEM images of FIB cross-sections, TEM characterization, STEM-EDX mapping
SL1	2	4.91E-06	1	SEM images of FIB cross-sections
SL1	126	4.03E-06	1	SEM images of FIB cross-sections, TEM characterization, TEM-EDX
SL1	779	2.82E-08	2	SEM images of FIB cross-sections, TEM characterization, STEM-EDX mapping
SL1	1192	5.20E-08	3	SEM images of FIB cross-sections, TEM characterization, STEM-EDX mapping
SL1	1345	5.20E-08	3	SEM images of FIB cross-sections
SL2	602	5.03E-08	3	SEM images of FIB cross-sections, TEM characterization, STEM-EDX mapping

5.3.1 Scanning electron microscopy observations of changes in the barite microstructure due to Ra uptake

The surface of Ra-barite solids from the different stages was characterized by SEM imaging (Fig. 42). Different effects on the barite microstructure from recrystallization and Ra uptake were observed. No rapid changes within the internal microstructure were detected during the first two days by SEM imaging of FIB cross-sections (see Appendix, Fig. 56). At the middle of stage 1 (day 126), the surface of the barite particle shows many pores and is very irregular. The particles remained well separated. This result is similar to the Ra-free reference barites recrystallized for 127 days.

At stage 2, the particles started growing together and form chains (Fig. 32b). Mostly they were attached to each other either on the {210} surfaces or at the {100} surfaces. During the Ra uptake and barite recrystallization until stage 3, the barite surface is smoothened. Less pores than before are visible. When equilibrium is approached in stage 3, long chains of particles have formed, which produce a complex three-dimensional structure. Furthermore, the reattachment of small particles is visible (Fig. 42 c). This feature was not observed during the recrystallization of the Ra-free reference barite. In addition, the particles' shape is closer to a euhedral shape than at the beginning of equilibration. In Fig. 42 c the particle marked with an arrow highlights a hollow barite particle.

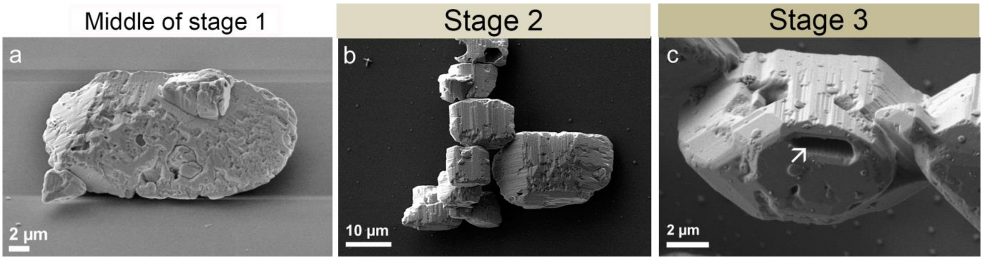

Fig. 42 SEM images showing the effects of recrystallization of barite SL 1 in the presence of Ra. At the end of stage 1 (a), the crystal surfaces are very rough and many pores are visible. The Ra-barites start growing together and show smoothing of the crystal surfaces at the stage 2 (b). The particle shape evolves more towards euhedral barite shape. The hull of an empty particle is visible. At the stage 3 (c), the Ra-barite particles are grown together. Crystal surfaces are smoother with new precipitates on them; the arrow indicates a hole.

The observed effects of the recrystallization of barite in the presence of Ra are (1) smoothening of the particle surface and (2) transformation towards a more euhedral habitus. Both effects minimize the free energy of the overall system. Heberling et al. (2016) observed the same effects during for calcite recrystallization and attributed them entirely to Ostwald ripening.

SEM images of the Ra-barite particles at stage 3 (Fig. 42 c) demonstrates that the particles form chains, which are several 100 µm long. These particles mostly attach at the {210} crystal face. The particles form three-dimensional arrangements. Chain formation of particles in colloidal size, usually nm or µm range, was already observed for gold particles (Thiele et al., 1962) or in Ludox® colloidal silica (Deželić et al., 1959) and has been extensively studied during the past decades. It was demonstrated, that the geometry of these particle aggregates can be predicted, namely by methods based on fractal geometry (Sutherland, 1970; Meakin, 1992). Klinkenberg et al. (2014) reported that such growing together in an oriented way of the particles was only observed in the Ra-barites and not in the reference Ra-free barite. It has to be taken into account that the observations of Klinkenberg et al. (2014) were made on SL barite samples recrystallized for 443 day. Therefore, it is possible, that the chain formation was not evident yet at that time in the reference experiment. In some of the reference experiments, Ra-free barite particles were observed to grow together after a recrystallization time of 898 days (Fig. 36).

5.3.2 *SEM observations of the FIB cross-sections*

FIB cross-sections of Ra-barite from all three stages of recrystallization were prepared by FIB and then depicted with SEM (Fig. 43). At the beginning of stage 1, the morphology of the both Ra-free reference SL barite and the Ra-barite still appeared to be very similar. The layered structure consisting of nano-scale fluid filled pores occurred in both samples (Fig. 43 a + b). In addition, some particles contained macropores. At the middle of stage 1, the layered structure began to disappear and many macropores were observed (Fig. 43 c + d). This may be interpreted that the nano-scale pores coalesced, forming new macropores. Some of the macropores had a hexagonal cross-section shape. At stage 2, the macropores were elongated and oriented parallel to the outer particle surfaces.

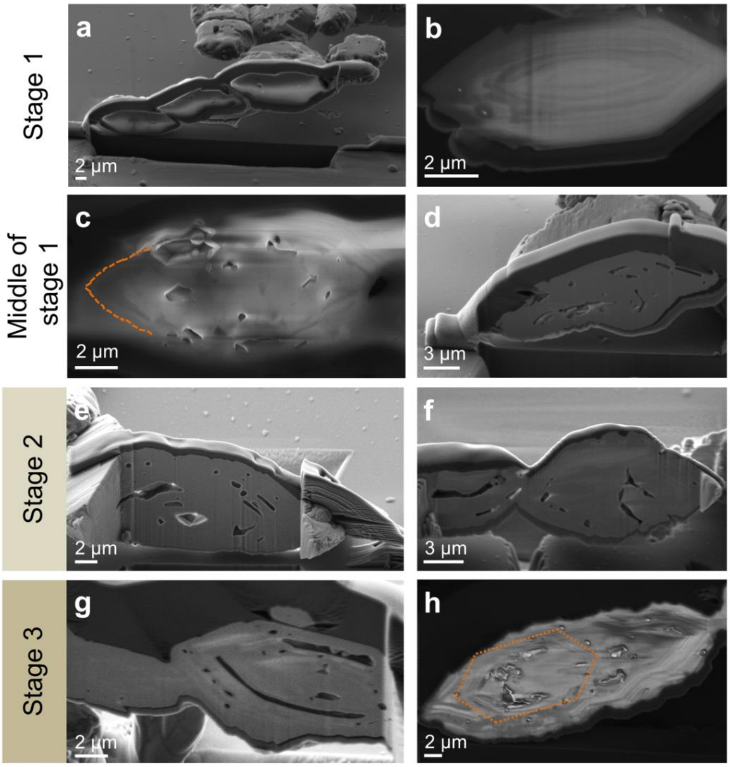

Fig. 43 **Cross-sections of Ra-barites from different stages. In stage 1, particles with macropores (a) are present as well as particles with a layered structure (b). This layered structure starts to disappear in the middle of stage 1 (c) and more elongated pores can be observed (d). At stage 2, hollow barite cores are observed (e) as well as particles growing together (f). At stage 3, the macropores grow together (g) as well as particles marked by an orange dotted line are completely grown together to new particles (h).**

The semi-quantitative image analysis of the macroporosity exhibits a trend for the Ra uptake experiments (Tab. 6). In general, the average area-based porosity is higher compared to the Ra-free recrystallization experiments. Also the number of pores is in average higher than for the analyzed solids from the Ra-free reference experiments. The maximum area-based porosity for the solids from the Ra uptake experiments is higher as well. Here, the maximum area-based porosity at the beginning of stage 1 is of particular interest as it is already high at this point compared to the reference SL barite. Already for the Ra-free reference SL barite it was observed that the porosity determined from 2D cross-section analysis is to some degree not providing completely reliable information about the amount of pores determined in 3D cross-sections.

Tab. 6 Evolution of area-based macroporosity during Ra uptake based on semi-quantitative image analysis.

Stage	Number of analyzed cross-sections	Area-based porosity [%]	Number of pores per particle	Maximum area-based porosity [%]
Start of 1	9	3.5	3.4	18.6
Middle of 1	12	6.6	7.0	22.3
2	4	3.7	15.0	7.3
3	25	2.3	10.4	19

5.3.3 Scanning Transmission Electron Microscopy

HAADF STEM images were collected from the Ra-barite samples taken at the end of stage 1, stage 2 and stage 3 (Fig. 44). The Ra-barite at the middle of stage 1 still showed some remains of the layered structure (Fig. 44 a + b). At higher magnification, the nano-scale pores appear to accumulate in thicker layers and coalesce (Fig. 44 c). At stage 2, the layered structure cannot be recognized anymore. Contrast differences are visible but they cannot be attributed to a layered structure (Fig. 44 d – f). Furthermore, the macroporosity increased. In Fig. 44 f, an area of bright contrast is connecting two of the macropores. As the HAADF STEM contrast is related to the mass and density of the analyzed material, this area might contain heavier elements than Ba, e.g. Ra. Many chains in Ra-barite particles grown together were observed at stage 3 (Fig. 43 c + g). Both particles in Fig. 44 g consist of a massive rim and a core having nano-scale pores. The left particle is magnified in the inset of Fig. 44 g. This insets shows that a massive rim and a porous interior. In addition to the nano-scale pores without any orientation, some elongated nano-scale pores are oriented parallel to the outer particle surfaces, similar to what was visible in FIB cross-sections (Fig. 43 c).

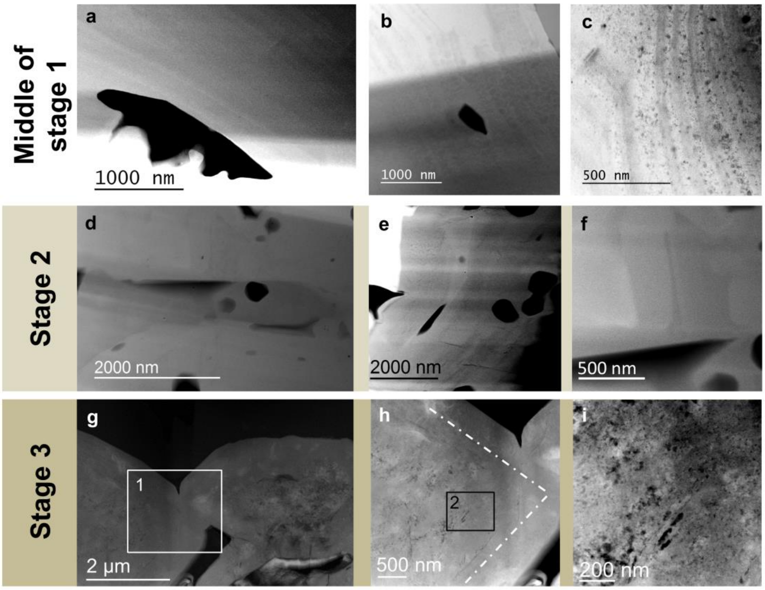

Fig. 44 **HAADF STEM images of the Ra-barite sampled at different stages of recrystallization. The Ra-barites from the middle of the stage 1 clearly displays a layered structure (a) and (b). At higher magnification (c), it is visible that the layers consist of larger nano-scale pores similar as observed in the beginning of stage 1. At stage 2, no layered structure can be observed anymore (d) – (e). Contrast changes are visible but not due to nano-scale porosity. At the stage 3 (g), a massive outer rim is visible. The area (1) is magnified in (h) showing this massive rim. The particles contain newly formed nano-scale porosity in the area (2) which is magnified in (i).**

Several particles which are grown together are presented in HAADF STEM contrast in Fig. 45. As the particles exhibit different contrast, it can be concluded that these particles have different crystal orientations. The upper particle shows three macropores and several smaller pores. The inset which is enlarged in Fig. 44 b shows the inclusion of pores during the intergrowth of particles. In these particles, no layered structure is visible anymore. In contrast to the particles in Fig. 44 g and h, no rim is visible.

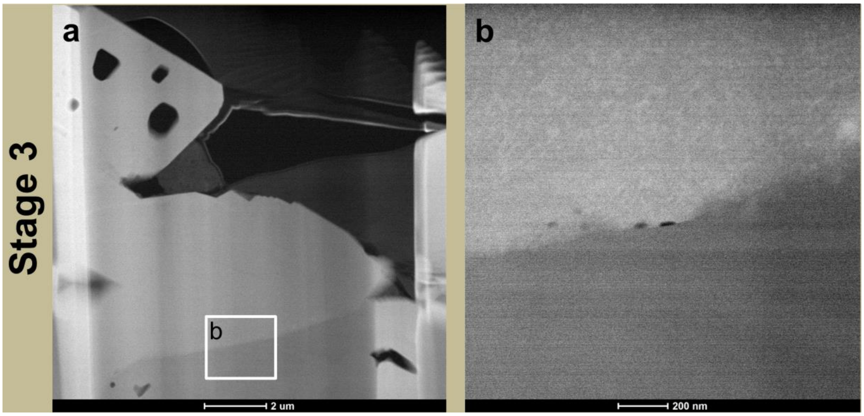

Fig. 45 **HAADF STEM images of Ra-barites (SL1) of stage 3 presenting intergrowth of particles (a) and inclusion of pores (b). The different HAADF contrast of the two grains indicates that the particles have different orientations.**

5.3.4 Transmission Electron Microscopy

In addition to the HAADF STEM contrast images (Fig. 46 b + c) of a Ra-barite at the middle of stage 1, images in TEM BF contrast of the same lamella were acquired (Fig. 46). The lamella consists of two barite particles, which seems to be grown together. At higher magnification, the intergrowth of two particles can be confirmed (Fig. 46 b).

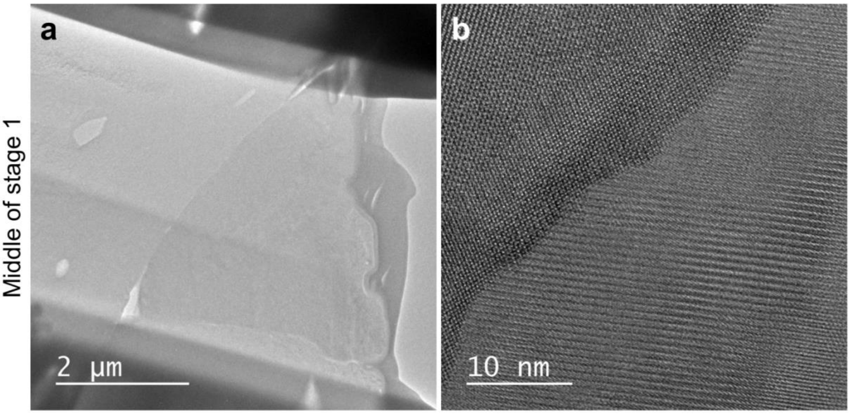

Fig. 46 **TEM BF contrast images the SL 1 Ra-barite from the middle of stage 1. The TEM lamella (a) consists of two different particles. Pores inside the material may be distinguished as bright areas within the material. The interface between the two particles (b) shows an intergrowth at higher resolution.**

5.3.5 *Single Area Electron Diffraction*

SAED patterns from the barite solids sampled at the different stages of Ra uptake were recorded (Fig. 47). SAED patterns from the solids sampled at the end of stage 1 and at stage 3 did not exhibit any additional reflexes or any defects (Fig. 47 a + c). In contrast, the pattern acquired from the solids at the stage 2 showed additional reflexes (Fig. 47 b). The lamella of this sample was prepared from a particle obtained by intergrowth of several particles which explains the occurrence of several reflexes. The main orientation of the lamella was determined.

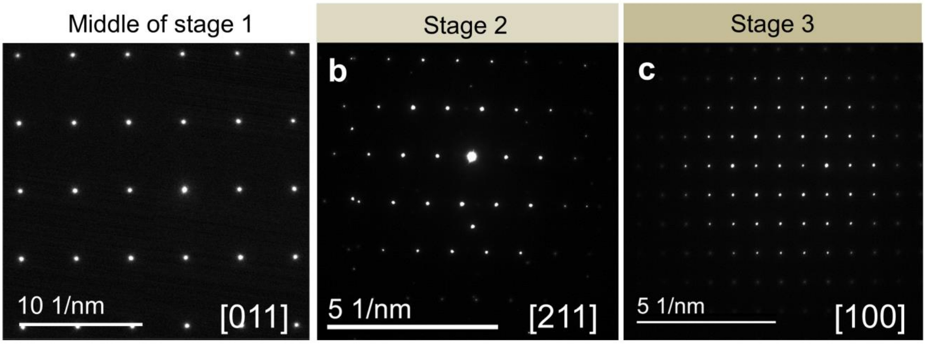

Fig. 47 SAED pattern from Ra-barite at different stages of recrystallization. The SAED pattern (a) from the solid sampled from the middle of stage 1 shows no additional reflexes compared to the Ra-free reference barite. In the SAED pattern of the Ra-barite from stage 2 (b) several additional reflexes are present due to intergrowth of several particles. SAED pattern (c) from a Ra-barite from stage 3 exhibited no additional reflexes.

5.4 Changes in the Ra distribution

The temporal evolution of the Ra distribution within the SL barite was examined in order to gain a deeper understanding of the uptake mechanism. Probably due to the increase in macroporosity, APT characterization was not possible. Several attempts of characterizing the Ra-containing samples of stage 2 and 3 with APT were done. The APT tips broke very fast and therefore, STEM-EDX characterization was conducted using a FEI Titan G^2 ChemiSTEM^{TM} instrument with Super-EDX^{TM} geometry. The EDX signal is increased by the higher number of EDX detectors of four which are annular oriented around the sample.

5.4.1 STEM-EDX Mappings

First, samples from the middle of stage 1 (day 126) were characterized. At this point in time of the experiment, already 19 % of the Ra in solution was taken up into the barite. This amount of Ra was not detectable in STEM-EDX measurements. Either the local Ra concentration was below the detection limit of the STEM-EDX or the Ra is still inside the fluid filled pores of the barite. These pores would possibly have been opened during the FIB milling.
At stage 2, Ra was inhomogeneously distributed. In Fig. 48 a HAADF STEM image of a Ra-barite from stage 2 is presented. Areas of different contrast were visible in HAADF contrast (Fig. 48 a + b). Differences in HAADF contrast can result from different masses or densities of the analyzed material or thickness variations within the lamella. The lamella (Fig. 48) has thick bars at the edge of the lamella due to the FIB preparation used for porous samples. This thick edge is represented in Fig. 48 a as a very bright area in the upper part of the image.

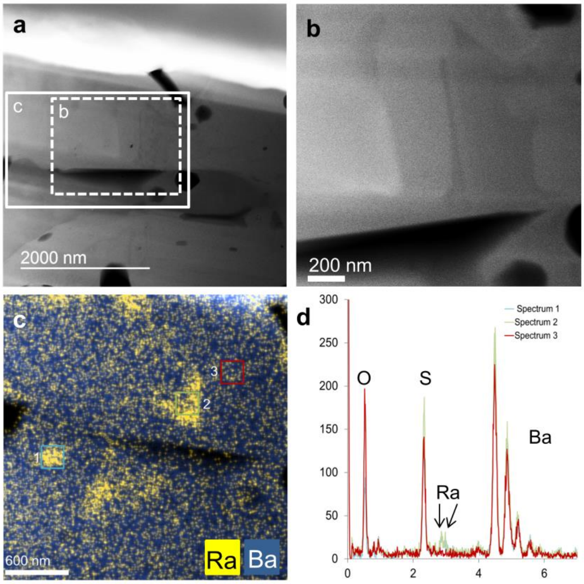

Fig. 48 **Inhomogeneous Ra distribution within barites sampled at stage 2. The first HAADF image (a) gives an overview of the barite sample. The mapping area is highlighted as well as the enlarged region presented in (b). Three different spectra of the regions indicated by colored squares in (c) are shown in (d).**

The other contrast variations, which can be found in the lower part of Fig. 48 a, are probably not originating from variations in the sample thickness. The magnified region highlighted by the dashed box marked with b in Fig. 48 a is displayed in Fig.

48 b. Areas of different contrast are present. In addition to this enlarged region, the area of the STEM-EDX mapping is highlighted by a box in Fig. 48 a as well. Regions of higher Ra concentration are visible in the STEM-EDX mapping (Fig. 48 c). They are located next to a macropore. Therefore, the macropores may be a reactive site by which Ra is taken up into the barite volume. Furthermore, it is evident that the brighter areas of the HAADF image match the regions of higher Ra-concentration.

An inhomogeneous Ra distribution within the barite sample SL 1 at stage 2 was also observed in a second lamella (Fig. 49). The HAADF STEM image also indicated by differences in contrast that there might be some inhomogeneities present similar to the sample presented in Fig. 48. The bright area in this sample is located between two pores. The EDX mapping demonstrates that the Ra distribution is not only inhomogeneous but that its distribution also matches the HAADF contrast differences. The spectra of two areas are given in Fig. 49 c. The spectra of the Ra-rich area clearly contained a Ra peak whereas the area without Ra did not show any peak.

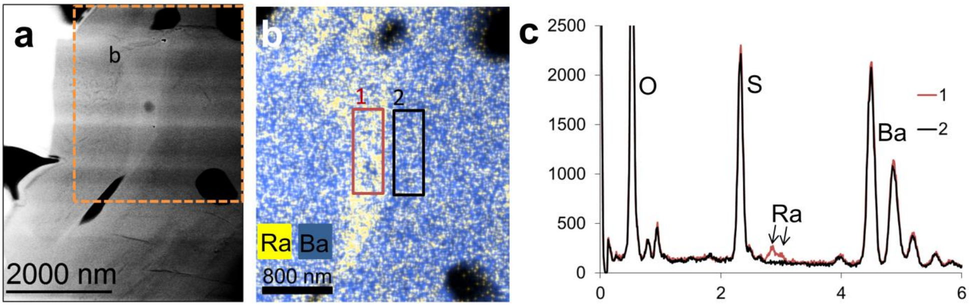

Fig. 49 **HAADF STEM contrast indicating inhomogeneities in the Ra distribution. The brighter areas in the HAADF STEM images (a) are Ra-rich regions as visible in the STEM-EDX mapping (b) of the orange marked area in (a). The spectra over the two areas marked in (b) are presented in (c) showing a clear peak for Ra for the area 1 but no peak for area 2.**

Ra distributed around macropores was observed (Fig. 50 a). Here, the Ra was distributed in a circular shape around one of the macropores (right upper corner), similar to a rim. In addition to this rim around one of the macropores, the other macropore shows Ra-rich areas next to it. These areas have circular shape. As the images of a TEM lamella only present a two-dimensional image, the areas marked with 1 and 2 in Fig. 50 could also be part of a rim around a macropore which is in the three-dimensional space above the plane of the TEM lamella.

The rim structure might be explained by a dissolution-reprecipitation process. Already Perdikouri et al. (2013) observed that a fluid which is enclosed inside a crystal continues to react. This might be what can be observed here as well. The round distribution of the Ra around the macropores might be explained in this way: at the beginning, the macropores was connected to the bulk fluid which was Ra-rich. Subsequently, a Ra-rich phase precipitated. Then, the following fluid did not contain as much Ra as before. Therefore, barite with less Ra-content precipitated.

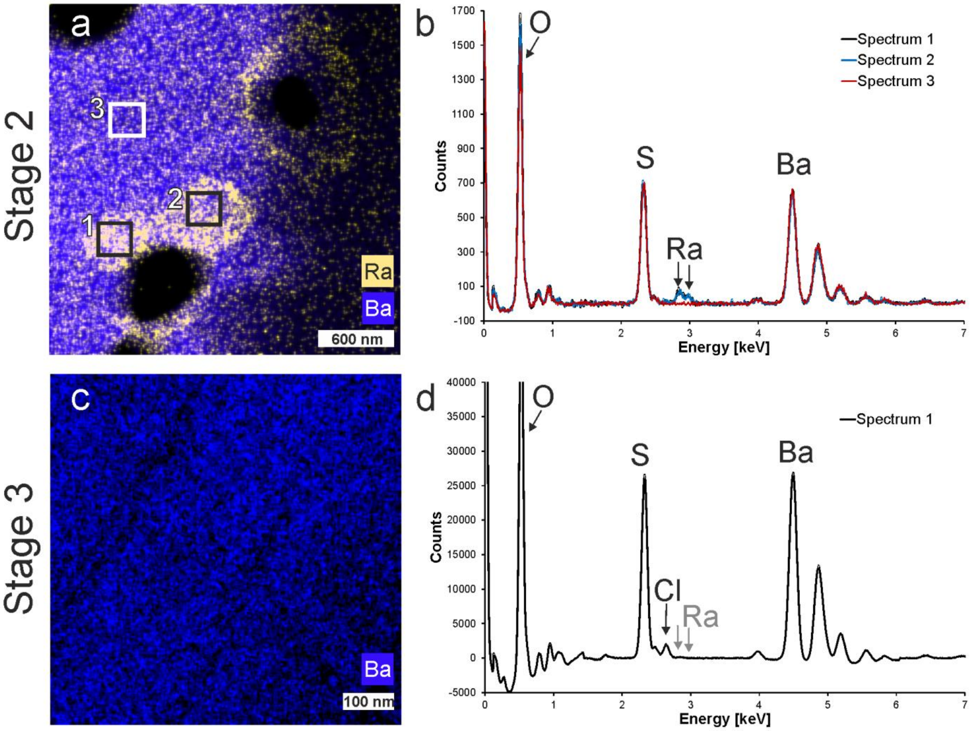

Fig. 50 **Ra distribution within the barite at stage 2 and stage 3. Inhomogeneities are evident in the Ra-distribution (yellow) at stage 2 (a). The spectra for the three different regions in (a) are displayed in (b). The spectra 1 and 2 clearly show a peak for Ra, whereas the spectrum 3 does not show any Ra peak. The STEM-EDX mapping (c) for Ba (blue) at stage 3 displays no inhomogeneities. Also in the EDX spectrum (d) over the complete area, no Ra peak is detected.**

Eventually, the macropores may have been disconnected from the bulk solution and the macropores remained. Chemical inhomogeneities in Ra-barite were also observed in nature (Randa et al., 2010). Another possibility of inhomogeneous incorporation could be entrapment of Ra-rich phases during rapid barite growth (Thien et al., 2014). In contrast to this theory based on rapid growth, inhomogeneous gold distribution within arsenopyrite was explained by Fougerouse et al. (2016) with slow growth.

At stage 3, no Ra was detected by STEM-EDX. Based on the Ra concentration in solution, the expected Ra concentration at a homogeneous distribution was determined to be 60 ppm. This concentration is below the detection level of EDX. Therefore, its distribution can be interpreted to be homogeneous within the sensitivity of this method. NaCl precipitates inside the barite sample were observed in STEM-EDX mappings. The HAADF contrast image of stage 3 (Fig. 50 c) demonstrates that several small pores are located along a fracture inside the barite. It cannot be determined whether these pores caused the fracture or whether have accumulated along the fracture.

The results of this study are in good agreement with the study of Herberling et al. (2016) on ^{45}Ca uptake into calcite. They assign the driving forces of the recrystallization to the Ostwald ripening process which reduces the free energy in the system. Three different ways of minimization of the free energy are possible: the decrease in particle roughness, the transformation towards a more stable crystal habitus and the increase in particle size. In this study on Ra uptake into barite the changes in the internal microstructure were identified. These observations further strengthen the role of the Ra incorporation in providing an additional driving force for recrystallization despite its small concentration.

The radioactive characteristics of ^{226}Ra could be one possible reason for its role as additional driving force. The Ra-rich regions observed in stage 2 exhibited a Ra-concentration of 5 ± 2 at% Ra and therefore the alpha decay of Ra would probably cause damages in the crystal lattice. Weigl & Trinkl (1968) reported in their study a rapid reduction of the crystallinity of $RaCl_2$ within days during their experiments.

In addition, radionuclides which undergo an alpha-decay can cause an alpha-recoil. In the process of alpha-recoil, a radioactive daughter is mobilized from its position by the energy of an alpha-decay (Sun & Semkow, 1998). The atomic nucleus emits an alpha particle during this alpha-decay while releasing an ionizing energy of 4-6 MeV. Due to the law of momentum conversation, the emitted alpha particle and the recoiling nucleus will have a defined energy after the decay. Most of the kinetic energy is transferred into the alpha particle due to its smaller mass. Accordingly, the recoiling nucleus will have a kinetic energy in the order of 100 keV (Sun & Semkow, 1998). This energy transfer is to the decay product is high enough to shift atoms located close to the surface out of the mineral, either into pore space or the aqueous solution (Fig. 51).

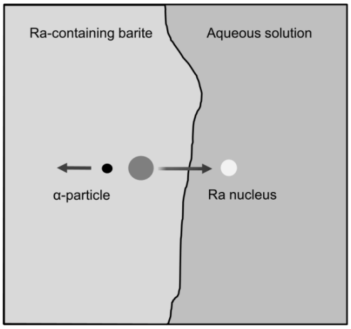

Fig. 51 Alpha-recoil of ^{226}Ra in Ra-barite (Modified after Eggeling et al., 2013).

Eggeling et al. (2013) analyzed fluids of two geothermal sites within the upper Rhine Graben which showed disequilibrium of the radioactive elements dominated by Ra. They proposed the alpha-recoil of Ra originating from Th as a possible reason (Eggeling et al., 2013).

6 Conclusion

Deeper insights into the mechanism of Ra uptake into pre-existing barite were gained by characterizing barite and Ra-barite samples with a state-of-the-art high resolution microscopic approach. Three questions were addressed regarding the Ra uptake process: (1) The internal microstructure of the initial barite, (2) the role of the internal microstructure and (3) the evolution of the Ra distribution within the barite during the Ra uptake.

Internal microstructure of the initial barite

Two different barite types (AL and SL barite) were examined using a combination of SEM, FIB, TEM and APT methods. Substantial method development was required for the material characterization because barite and Ra-containing barite were examined by this approach for the first time. First, the internal microstructure was accessed by cutting cross-sections into the barite with a FIB instrument. Subsequently, SEM images were recorded of the cross-sections. The distribution of macropores within the barite particle volume was examined by FIB-tomography. Then, the solids were characterized by a combination of various TEM techniques and APT. Both characterization methods required a highly sophisticated FIB sample preparation. Therefore, the sample preparation procedure was tailored for the barite and the Ra-containing barites.

The SL barite particles were single crystals as identified by electron diffraction. No further defects were observed in the SL barite structure by high resolution BF TEM imaging. HAADF STEM images exhibited a crystallographically oriented layered structure inside the SL barite particles. The layered structure consisted of nano-scale fluid inclusions. These enlarged the available internal surface. Therefore, a possible dissolution-reprecipitation process may be enhanced. In addition, open macropores of several micrometer size were present within the SL barite samples. These macropores were distributed within the complete barite crystal volume. In addition, they were partially connected. Therefore, they provided a direct pathway for Ra to enter the barite particles by diffusing within the aqueous phase. The AL barite sample also contained pores of a round shape. Some of these pores were located along the grain boundaries. Due to the small particle size, no further investigations could be performed on the connectivity or filling of the pores within the AL barite.

The entrapment of fluid inclusions during mineral precipitation was observed previously for various minerals. Therefore, both nano-scale fluid filled inclusions as well as macropores may be entrapped during the barite precipitation and particle growth.

In addition, studies available in literature report a similar microstructure for natural barite as observed in this doctoral study. In conclusion, the SL and AL barite used in the experiments of Curti et al. (2010), Klinkenberg et al. (2014) and Brandt et al. (2015) may be considered representative for other barites as well.

Role of the barite microstructure during the Ra uptake

The internal microstructure of Ra-free barite samples recrystallized for different periods of time was characterized. No changes were identified in the internal barite microstructure of both, the AL and SL barite samples, for recrystallization times of up to 898 days. With increasing recrystallization time, the surfaces of the particles became smoother, reducing the free energy in the total system. This free energy reduction is part of an Ostwald ripening process. Studies by Curti et al. (2010) and Bosbach et al. (2010) using a ^{133}Ba tracer postulated the complete exchange of SL barite particles within ~100 days. Either ^{133}Ba provided in these experiments a substantial driving force for recrystallization or the fluid inclusions inside the barite were stable despite complete barite recrystallization.

The complete Ra uptake experiment duration was divided into three stages based on the evolution of the Ra concentration in the aqueous phase. SEM and TEM characterization of SL barites from all stages was carried out. In the presence of Ra, the surface of the SL barite crystals became smoother, similar to the SL barite samples of the Ra-free recrystallization experiments. The overall porosity of the barite crystals changed in several steps. At the beginning, the nano-scale fluid inclusions disappeared, probably due to coalescing to new macropores. This is also part of an Ostwald ripening process driven by the minimization of the free energy in the system. Later, the Ra-barite particles contained a banked rim with no porosity and an inner core of nano-scale porosity. In addition, the amount of macroporosity increased temporarily and was then reduced again.

Changes in the Ra distribution

In all three stages of Ra uptake, chemical analyses by STEM-EDX were conducted. A characteristic evolution of the Ra distribution within the solids with time was observed. During stage 1, no Ra was noted in the solid at the detection limit of STEM-EDX despite a significant reduction of the aqueous Ra concentration. Ra may have migrated within the aqueous phase into the barite samples and may be still contained within the macropores. During stage 2, Ra was distributed inhomogeneously within the barite crystals. It was concentrated in a rim shape around some macropores. Several macropores were not surrounded by a Ra-rich rim, probably because they were not connected to the surrounding aqueous solution. During stage 3, the Ra concentration was below the detection limit of STEM-EDX. Accordingly, the Ra distribution can be interpreted to be homogeneous at this scale. Thermodynamic equilibrium was reached at stage 3 as proposed by the homogeneous Ra distribution in the solid and the stable aqueous Ra concentration.

Mechanism of Ra uptake into barite

The recrystallization of barite in the presence of Ra was noted to be completely different compared to pure barite recrystallization. The uptake of Ra caused fundamental changes within the Ra microstructure. Despite its low concentration, Ra was a thermodynamic driving force which triggered the complete barite to recrystallize. This significant difference may be explained by the radioactive properties of ^{226}Ra. The radiation damage possibly caused by the alpha-decay of ^{226}Ra enhances the microstructural changes.

Based on the available results, the Ra uptake into barite is proposed to be controlled by two different mechanisms operating at the same time. The first one is Ostwald ripening of the porosity inside the barite, the barite particles surface and the barite particles themselves which is driven by the free energy minimization. The second one is an autocatalytic dissolution-reprecipitation process caused by the chemical imbalance between the solid and the aqueous phase.

Different stages of the Ra uptake were observed (Fig. 52). During the first stage, Ra migrated within the aqueous phase into the open macropores and reached the inside of the barite crystals. At the same time, the barite crystals started to recrystallize in order to minimize their free energy. The alpha-recoil of the Ra may have enhanced this process. When Ra reached the inside of the barite crystal, an autocatalytic dissolution-reprecipitation process may have started. The dissolution-reprecipitation process led to an uptake of Ra into barite in larger quantities than estimated from the calculated thermodynamic equilibrium concentration. This might take place by entrapment (Thien et al., 2014). The barite samples appeared to continuously recrystallize during this complete process. In the third stage, the dissolution and reprecipitation process continued and the Ra distribution within the barite SL sample homogenized by continuous recrystallization.

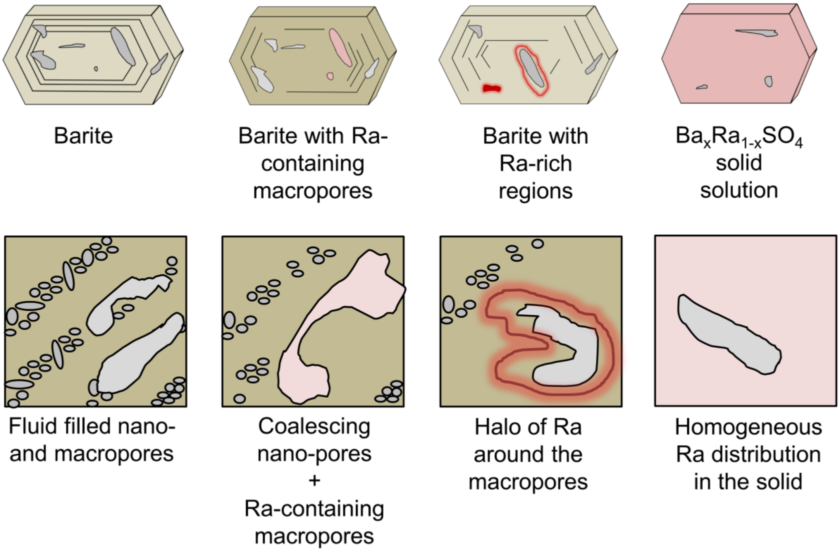

Fig. 52 Description of Ra uptake process in three stages. The evolution of internal microstructure in the presence of Ra is presented in the microscopic scale at the top and the nano-scale at the bottom.

The replacement proceeded from a partial replacement inside of the SL barite particle to a complete replacement of the barite particle volume. In contrast, the water-mediated replacement process as described in literature takes place from the outside of the parent phase to the inside (Fig. 53 a). At first sight, this seems contradictory. The surface of the SL barite is enlarged when taking the open macroporosity inside the SL barite into account. Internal parts of the SL barite are accessible to the surrounding aqueous Ra-containing phase (Fig. 53 b).

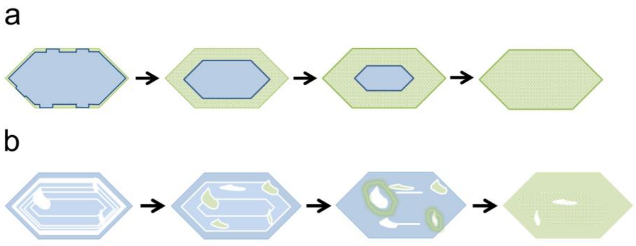

Fig. 53 Different models of water-mediated replacement. The literature model of dissolution-reprecipitation (modified after Ruiz-Agudo et al., 2014) assumes the replacement from the outside to the inside of the crystal (a). The model of replacement from the inside takes the internal microstructure of the starting material into account (b).

In previous studies on replacement processes macroscopically inclusion free minerals were used. In this doctoral thesis, the complex internal microstructure of the initial reference SL barite was identified. This internal microstructure enables the Ra uptake from the inside of the SL barite particle by a dissolution-reprecipitation process resulting in a homogeneous $Ba_xRa_{1-x}SO_4$ solid solution.

7 Outlook

The characterization methods developed in this doctoral thesis are useful tools for the analysis of a variety of mineral samples with highest spatial resolution. The characterization of sulfates and other soft minerals on the molecular scale becomes possible using these methods. The elaboration of completely new questions would be feasible with these high resolution methods regarding e.g. recrystallization mechanism and the mechanism of dissolution-reprecipitation. Several reviews have remarked that high resolution analyses are necessary for the further investigation of these research questions (see Reviews of Ruiz-Agudo et al., 2014 and Gorski et al., 2016).

Furthermore, the analysis of similar barite samples would be possible from experiment under different conditions, e.g. elevated temperatures or different barite types. The mechanism of Ra uptake into barite can be further elaborated by the analysis of the solids from Ra uptake experiments using the AL barite. TEM lamellae preparation methods were established in this doctoral thesis for Ra-free AL barites. These methods are available for the preparation of the Ra-containing AL barite samples. APT characterization may not be possible due to the small particle size. However, the formation of new, large crystals was observed in Klinkenberg et al. (2014). FIB preparation on these larger crystals may be successful.

In nature, Sr is often present in the same system as barite and Ra. The formation of the ternary $(Ba,Ra,Sr)SO_4$ solid solution is possible based on thermodynamics. Laboratory experiments and the microscopic methods developed in this work could provide further insights into the effect of Sr onto the Ra uptake.

The alpha-emission of the ^{226}Ra is most likely to cause radiation damage in the barite structure which has an influence on the crystallinity and might cause changes in the internal microstructure. The TEM characterization performed in this doctoral thesis showed no defects in the crystal structure after Ra uptake. It has to be considered that the FIB lamellae preparation from the Ra-barites was extremely challenging. No FIB lamellae which were thin enough for HR-TEM analyses were obtained from Ra-containing samples. A further development of the preparation procedure could possibly lead to thinner samples and enable the application of HR-TEM investigations.

An alternative method for the investigation of the radiation damage could be the use of bulk analysis methods. Previous studies in literature have shown that it is possible to analyze the crystallinity of a sample in comparison to a reference sample and to identify changes by (Fourier transformed) Raman spectroscopy (e.g. Taylor & Zografi, 1998; Nielsen et al., 2002). The radiation damage distance could be calculated with stopping and range of ions in material (SRIM) software. The necessary E_d values for barite could be calculated by atomistic modeling similar to e.g. Ji et al. (2016).

8 List of figures

Tab. 3, Fig. 19, Fig. 20, Fig. 21, Fig. 22, Fig. 23, Fig. 24, Fig. 25, Fig. 26, Fig. 27 and Tab. 9 were reprinted from Nano-structural features of barite crystals observed by electron microscopy and atom probe tomography, Vol. 424, Weber, J., Barthel, J. Brandt, F., Klinkenberg, M., Breuer, U., Kruth, M., Bosbach, D., Chemical Geology, 51-59, 2016 with permission from Elsevier.

Fig. 14 was reprinted from Replacement of barite by a $(Ba,Ra)SO_4$ solid solution at close-to-equilibrium conditions: A combined experimental and theoretical study, Vol. 155, Brandt, F., Curti, E., Klinkenberg, M., Rozov, K., Bosbach, D., Geochimica et Cosmochimica Acta, 1-15, 2015 with permission from Elsevier.

9 List of tables

10 References

2015, Dritte Verordnung zur Änderung der Trinkwasserverordnung in UBA, ed.

Alexander, W. R., and McKinley, L., 2011, Deep geological disposal of radioactive waste, Elsevier, 300 p.

Altree-Williams, A., Pring, A., Ngothai, Y., and Brugger, J., 2015, Textural and compositional complexities resulting from coupled dissolution–reprecipitation reactions in geomaterials: Earth-Science Reviews, v. 150, p. 628-651.

Álvarez-Lloret, P., Rodríguez-Navarro, A. B., Falini, G., Fermani, S., and Ortega-Huertas, M., 2010, Crystallographic control of the hydrothermal conversion of calcitic sea urchin spine (*Paracentrotus lividus*) into apatite: Crystal Growth & Design, v. 10, no. 12, p. 5227-5232.

Amelinckx, S., 1953. A dislocation mechanism for the growth of hopper crystal faces and the growth of salol crystals from solution and from the melt: The London, Edinburgh, and Dublin Philosophical Magazine and Journal of Science, v. 44, no. 350, p. 337-339.

Ames, L. L., McGarrah, J. E., and Walker, B. A., 1983, Sorption of trace constituents from aqueous solutions onto secondary minerals. II. Radium: Clays and Clay Minerals, v. 31, no. 5, p. 335-342.

Ames, L. L., McGarrah, J. E., and Walker, B. A., 1983, Sorption of uranium and radium by biotite, muscovite, and phlogopite: Clays and Clay Minerals, v. 31, no. 5, p. 343-351.

Anovitz, L. M., and Cole, D. R., 2015, Characterization and analysis of porosity and pore structures: Reviews in Mineralogy and geochemistry, v. 80, no. 1, p. 61-164.

Asl, S. M., Jafari, M., Sahamiyeh, R. Z., and Shahrokhi, V., 2015, Geology, geochemistry, sulfur isotope composition, and fluid inclusion data of Farsesh barite deposit, Lorestan Province, Iran: Arabian Journal of Geosciences, v. 8, no. 9, p. 7125-7139.

Bahl, S., Lochab, S., Pandey, A., Kumar, V., Aleynikov, V., Molokanov, A., and Kumar, P., 2014, Characterization and luminescence studies of Eu doped Barite nanophosphor: Journal of Luminescence, v. 149, p. 176-184.

Baisden, P., and Atkins-Duffin, C., 2011, Radioactive waste management, Handbook of nuclear chemistry, Springer, p. 2797-2835.

Bell, D. R., and Rossman, G. R., 1992, Water in Earth's mantle: the role of nominally anhydrous minerals: Science, v. 255, no. 5050, p. 1391.

Bennett, D. G., and Gens, R., 2008, Overview of European concepts for high-level waste and spent fuel disposal with special reference waste container corrosion: Journal of Nuclear Materials, v. 379, no. 1–3, p. 1-8.

BGR, 2007. Endlagerung radioaktiver Abfälle in Deutschland Untersuchung und Bewertung von Regionen mit potenziell geeigneten Wirtsgesteinsformationen.

Blount, C. W., 1977, Barite solubilities and thermodynamic quantities up to 300 - 0 C and 1400 bars. American Mineralogist, v. 62, p. 9-10.

Bodnar, R. J., Lecumberri-Sanchez, P., Moncada, D., and Steele-MacInnis, M., 2014, 13.5 - Fluid Inclusions in Hydrothermal Ore Deposits A2 - Holland, Heinrich D, in Turekian, K. K., ed., Treatise on Geochemistry (Second Edition): Oxford, Elsevier, p. 119-142.

Böhlke, J. K., and Irwin, J. J., 1992, Brine history indicated by argon, krypton, chlorine, bromine, and iodine analyses of fluid inclusions from the Mississippi Valley type lead-fluorite-barite deposits at Hansonburg, New Mexico: Earth and Planetary Science Letters, v. 110, no. 1, p. 51-66.

Bonotto, D. M., 2015, ^{226}Ra and ^{228}Ra in mineral waters of southeast Brazil: Environmental Earth Sciences, v. 74, no. 1, p. 839-853.

Borg, S., Liu, W., Pearce, M., Cleverley, J., and MacRae, C., 2014, Complex mineral zoning patterns caused by ultra-local equilibrium at reaction interfaces: Geology, v. 42, no. 5, p. 415-418.

Borole, D., and Somayajulu, B., 1977, Radium and lead-210 in marine barite: Marine Chemistry, v. 5, no. 3, p. 291-296.

Bosbach, D., Boettle, M., and Metz, V., 2010, Experimental study on Ra^{2+} uptake by barite ($BaSO_4$). Kinetics of solid solution formation via $BaSO_4$ dissolution and $Ra_xBa_{1-x}SO_4$ (re) precipitation: Swedish Nuclear Fuel and Waste Management Co., TR-10-43.

Bosbach, D., Hall, C., and Putnis, A., 1998, Mineral precipitation and dissolution in aqueous solution: in-situ microscopic observations on barite (001) with atomic force microscopy: Chemical Geology, v. 151, no. 1, p. 143-160.

Böttcher, M. E., and Dietzel, M., 2010, Metal-ion partitioning during low-temperature precipitation and dissolution of anhydrous carbonates and sulphates.

Brandt, F., Curti, E., Klinkenberg, M., Rozov, K., and Bosbach, D., 2015, Replacement of barite by a (Ba, Ra) SO_4 solid solution at close-to-equilibrium conditions: A combined experimental and theoretical study: Geochimica et cosmochimica acta, v. 155, p. 1-15.

Brown, P. L., Ekberg, C., Ramebäck, H., Hedström, H., and Matyskin, A., 2015, Solubility of Radium and Strontium Sulfate across the Temperature Range of 0 to 300° C, Uranium-Past and Future Challenges, Springer, p. 553-564.

Brown, W. B., Vincent, M., Trollope, K., and Hillier, I., 1992, Van der Waals and charge-transfer complexes of molecular oxygen and water: Chemical physics letters, v. 192, no. 2-3, p. 213-216.

Bruno, J., 2007, Chemical thermodynamics of solid solutions of interest in radioactive waste management: a state-of-the-art report, OECD Publishing.

Bruno, J., and Ewing, R. C., 2006, Spent nuclear fuel: Elements, v. 2, no. 6, p. 343-349.

Burnett, W. C., Peterson, R., Moore, W. S., and de Oliveira, J., 2008, Radon and radium isotopes as tracers of submarine groundwater discharge–results from the Ubatuba, Brazil SGD assessment intercomparison: Estuarine, Coastal and Shelf Science, v. 76, no. 3, p. 501-511.

Cairney, J. M., La Fontaine, A., Trimby, P., Yang, L., and Piazolo, S., 2015, Quantitative microstructural analysis of geological materials by atom probe: understanding the mechano-chemical behaviour of zircon: Microscopy and Microanalysis, v. 21, no. S3, p. 1317-1318.

Carvalho, F., Chambers, D., Fernandes, S., Fesenko, S., Goulet, R., Howard, B., Kim, C., Martin, P., Moore, W., and Phaneuf, M., 2014, The environmental behaviour of radium: revised edition. IAEA technical reports series no. 476.

Chałupnik, S., Franus, W., Wysocka, M., and Gzyl, G., 2013, Application of zeolites for radium removal from mine water: Environmental Science and Pollution Research, v. 20, no. 11, p. 7900-7906.

Chang, E. P., Williamson, G., and Evans, J. S., 2015, Focused Ion Beam Tomography Reveals the Presence of Micro-, Meso-, and Macroporous Intracrystalline Regions Introduced into Calcite Crystals by the Gastropod Nacre Protein AP7: Crystal Growth & Design, v. 15, no. 4, p. 1577-1582.

Chen, Y. M., Ohkubo, T., Kodzuka, M., Morita, K., and Hono, K., 2009, Laser-assisted atom probe analysis of zirconia/spinel nanocomposite ceramics: Scripta Materialia, v. 61, no. 7, p. 693-696.

Church, T. M., and Bernat, M., 1972, Thorium and uranium in marine barite: Earth and Planetary Science Letters, v. 14, no. 1, p. 139-144.

Curie, M., 1904, Recherches sur les substances radioactives, Gauthier-Villars.

Curie, M., 1911, Radium and the new concepts in chemistry: Nobel lecture.

Curie, P., and Curie, M., 1898, On a new radioactive substance contained in pitchblende: Comptes Rendus, v. 127, p. 175-178.

Curti, E., 1999, Coprecipitation of radionuclides with calcite: estimation of partition coefficients based on a review of laboratory investigations and geochemical data: Applied Geochemistry, v. 14, no. 4, p. 433-445.

Curti, E., Fujiwara, K., Iijima, K., Tits, J., Cuesta, C., Kitamura, A., Glaus, M., and Müller, W., 2010, Radium uptake during barite recrystallization at 23±2 C as a function of solution composition: an experimental 133 Ba and 226 Ra tracer study: Geochimica et Cosmochimica Acta, v. 74, no. 12, p. 3553-3570.

David, S. T. W. E., Taylor, T. G., Woolnough, W. G., and Foxall, H. G., 1905, Occurrence of the pseudomorph glendonite in New South Wales, William Applegate.

Davis, J. A., Fuller, C. C., and Cook, A. D., 1987, A model for trace metal sorption processes at the calcite surface: Adsorption of Cd2+ and subsequent solid solution formation: Geochimica et Cosmochimica Acta, v. 51, no. 6, p. 1477-1490.

De Yoreo, J. J., Burnham, A. K., and Whitman, P. K., 2002, Developing KH_2PO_4 and KD_2PO_4 crystals for the world's most power laser: International Materials Reviews, v. 47, no. 3, p. 113-152.

Deželić, G., Wrischer, M., Devide, Z., and Kratohvil, J., 1960, Electron microscopy of Ludox colloidal silica: Kolloid-Zeitschrift, v. 171, no. 1, p. 42-45.

Diercks, D. R., Gorman, B. P., Manerbino, A., and Coors, G., 2014, Atom Probe Tomography of Yttrium-Doped Barium–Cerium–Zirconium Oxide with NiO Addition: Journal of the American Ceramic Society, v. 97, no. 10, p. 3301-3306.

Diercks, D. R., Tong, J., Zhu, H., Kee, R., Baure, G., Nino, J. C., O'Hayre, R., and Gorman, B. P., 2016, Three-dimensional quantification of composition and electrostatic potential at individual grain boundaries in doped ceria: Journal of Materials Chemistry A, v. 4, no. 14, p. 5167-5175.

Doerner, H. A., and Hoskins, W. M., 1925, Co-precipitation of radium and barium sulfates Journal of the American Chemical Society, v. 47, no. 3, p. 662-675.

Dove, M. T., 2003, Structure and dynamics: an atomic view of materials, Oxford University Press.

Dritte Verordnung zur Änderung der Trinkwasserverordnung (TrinkwV 2001). Bundesgesetzblatt Teil I, 2015, Nr. 46 (25.11.2015).

Dunkel, K. G., and Putnis, A., 2014, Replacement and ion exchange reactions of scolecite in a high pH aqueous solution: European Journal of Mineralogy, v. 26, no. 1, p. 61-69.

Egerton, R. F., 2016, Physical principles of electron microscopy: an introduction to TEM, SEM, and AEM, Springer Science & Business Media.

Eggeling, L., Genter, A., Kölbel, T., and Münch, W., 2013, Impact of natural radionuclides on geothermal exploitation in the Upper Rhine Graben: Geothermics, v. 47, p. 80-88.

EPA, U. E. P. A., 2000, Radionuclide Final Rule in Agency, U. E. P.

Ernst Ruska-Centre for Microscopy and Spectroscopy with Electrons, 2016a. FEI Tecnai G2 F20. Journal of large-scale research facilities, 2, A77.

Ernst Ruska-Centre for Microscopy and Spectroscopy with Electrons, 2016b. FEI Titan 80-300 TEM. Journal of large-scale facilities, 2, A41.

Ernst Ruska-Centre for Microscopy and Spectroscopy with Electrons, 2016c. FEI Titan G2 80-200 CREWLEY. Journal of large-scale research facilities, 2, A43.

Ernst Ruska-Centre for Microscopy and Spectroscopy with Electrons, 2016d. FEI Helios NanoLab 460F1 FIB-SEM. Journal of large-scale research facilities, 2, A59

Ernst Ruska-Centre for Microscopy and Spectroscopy with Electrons, 2016e. FEI Helios NanoLab 400S FIB-SEM. Journal of large-scale research facilities, 2, A60.

Etschmann, B., Brugger, J., Pearce, M., Ta, C., Brautigan, D., Jung, M., and Pring, A., 2014, Grain boundaries as microreactors during reactive fluid flow: experimental dolomitization of a calcite marble: Contributions to Mineralogy and Petrology, v. 168, no. 2, p. 1-12.

EU, 2011. European Commission Staff Working Paper, Radioactive waste and spent fuel management in the European union. Brussels, 22.8.2011.

Ewing, R. C., Whittleston, R. A., and Yardley, B. W., 2016, Geological disposal of nuclear waste: a primer: Elements, v. 12, no. 4, p. 233-237.

Felfer, P. J., Alam, T., Ringer, S. P., and Cairney, J. M., 2012, A reproducible method for damage-free site-specific preparation of atom probe tips from interfaces: Microscopy research and technique, v. 75, no. 4, p. 484-491.

Fenter, P., McBride, M. T., Srajer, G., Sturchio, N. C., and Bosbach, D., 2001, Structure of Barite (001)− and (210)−Water Interfaces: The Journal of Physical Chemistry B, v. 105, no. 34, p. 8112-8119.

Fesenko, S., Zeiller, L., and Voigt, G., 2009, Site characterization and measurement strategies for remediation purposes: Radioactivity in the Environment, v. 14, p. 41-119.

Fischer, C., Kurganskaya, I., Schäfer, T., and Lüttge, A., 2014, Variability of crystal surface reactivity: What do we know?: Applied Geochemistry, v. 43, p. 132-157.

Fougerouse, D., Reddy, S. M., Saxey, D. W., Rickard, W. D., van Riessen, A., and Micklethwaite, S., 2016, Nanoscale gold clusters in arsenopyrite controlled by growth rate not concentration: Evidence from atom probe microscopyk: American Mineralogist, v. 101, no. 8, p. 1916-1919.

Freeman, S. R., Jones, F., Ogden, M. I., Oliviera, A., and Richmond, W. R., 2006, Effect of benzoic acids on barite and calcite precipitation: Crystal growth & design, v. 6, no. 11, p. 2579-2587.

Frondel, C., 1935, American Mineralogist, v. 20, no. 12, p. 853-862.

Gaboreau, S., Robinet, J.-C., and Prêt, D., 2016, Optimization of pore-network characterization of a compacted clay material by TEM and FIB/SEM imaging: Microporous and Mesoporous Materials, v. 224, p. 116-128.

Gault, B., Moody, M. P., Cairney, J. M., and Ringer, S. P., 2012, Atom probe microscopy, Springer Science & Business Media. 411 p.

Germann, F. E., 1921, Adsorption of Radium by Barium Sulphate: Journal of the American Chemical Society, v. 43, no. 7, p. 1615-1621.

Giannuzzi, L. A., and Stevie, F. A., 1999, A review of focused ion beam milling techniques for TEM specimen preparation: Micron, v. 30, no. 3, p. 197-204.

Glynn, P., 2000, Solid-solution solubilities and thermodynamics: sulfates, carbonates and halides: Reviews in Mineralogy and Geochemistry, v. 40, no. 1, p. 481-511.

Glynn, P. D., and Reardon, E. J., 1990, Solid-solution aqueous-solution equilibria: thermodynamic theory and representation: American Journal of Science, v. 290, no. 2, p. 164-201.

Godinho, J. R. A., and Stack, A. G., 2015, Growth kinetics and morphology of barite crystals derived from face-specific growth rates: Crystal Growth & Design, v. 15, no. 5, p. 2064-2071.

Goldschmidt, V. M., Thomassen, L., Ulrich, F., Barth, T. F. W., Lunde, G. O. J., Zachariasen, W. H., and Holmsen, D., 1925, Geochemische Verteilungsgesetze der Elemente, I kommission hos J. Dybwad.

Goldsmith, J. R., and Laves, F., 1954, The microcline-sanidine stability relations: Geochimica et Cosmochimica Acta, v. 5, no. 1, p. 1-19.

Gomer, R., 1961, Field Emission and Field Ion Microscopy, Harvard University Press.

González-Munoz, M. T., Fernández-Luque, B., Martínez-Ruiz, F., Chekroun, K. B., Arias, J. M., Rodríguez-Gallego, M., Martínez-Canamero, M., De Linares, C., and Paytan, A., 2003, Precipitation of barite by Myxococcus xanthus: possible implications for the biogeochemical cycle of barium: Applied and Environmental Microbiology, v. 69, no. 9, p. 5722-5725.

Gordon, L., and Rowley, K., 1957, Coprecipitation of radium with barium sulfate: Analytical chemistry, v. 29, no. 1, p. 34-37.

Gordon, L. M., and Joester, D., 2011, Nanoscale chemical tomography of buried organic-inorganic interfaces in the chiton tooth: Nature, v. 469, no. 7329, p. 194-197.

Gordon, L. M., Tran, L., and Joester, D., 2012, Atom probe tomography of apatites and bone-type mineralized tissues: ACS nano, v. 6, no. 12, p. 10667-10675.

Gorman, B., Diercks, D., Salmon, N., Stach, E., Amador, G., and Hartfield, C., 2008, Hardware and techniques for cross-correlative TEM and atom probe analysis: Microscopy Today, v. 16, no. 4, p. 42-47.

Gorman, B. P., Diercks, D. R., and Kirchhofer, R., 2013, Laser and Material Effects on Laser Pulsed Atom Probe Analysis of Oxide and Nitride Ceramics: Microscopy and Microanalysis, v. 19, no. SupplementS2, p. 1882-1883.

Gorman, B. P., Diercks, D. R., Parman, S., and Cooper, R., 2015, Atomic Scale Analysis of Terrestrial and Extra-Terrestrial Geomaterials Using Atom Probe Tomography: Microscopy and Microanalysis, v. 21, no. SupplementS3, p. 1311-1312.

Gorski, C.A., Fantle, M.S., 2016, Stable Mineral Recrystallization in Low Temperature Aqueous Systems: A Critical Review: Geochimica and Cosmochimica Acta, Accepted.

Grambow, G., Duro, L., Spahiu, K., Kulik, D., and Brandt, F., Final synthesis report SKIN Project.

Grandia, F., Merino, J., and Amphos, J. B., 2008, Assessment of the radium-barium co-precipitation and its potential influence on the solubility of Ra in the near-field, SKB Stockholm, Sweden, TR-08-07.

Griffith, E.M. and Paytan A., 2012. Barite in the ocean-occurrence, geochemistry and palaeoceanographic applications: Sedimentology, v.59, e.6, p- 1817-1835.

Grundl, T., and Cape, M., 2006, Geochemical factors controlling radium activity in a sandstone aquifer: Ground Water, v. 44, no. 4, p. 518-527.

Gu, H., Moore, W. S., Zhang, L., Du, J., and Zhang, J., 2012, Using radium isotopes to estimate the residence time and the contribution of submarine groundwater discharge (SGD) in the Changjiang effluent plume, East China Sea: Continental Shelf Research, v. 35, p. 95-107.

Hanor, J. S., 2000, Barite–celestine geochemistry and environments of formation: Reviews in Mineralogy and Geochemistry, v. 40, no. 1, p. 193-275.

Hartshorne, M. I., Isheim, D., Seidman, D. N., and Taheri, M. L., 2014, Specimen preparation for correlating transmission electron microscopy and atom probe tomography of mesoscale features: Ultramicroscopy, v. 147, p. 25-32.

Heberling, F., Paulig, L., Nie, Z., Schild, D., and Finck, N., Morphology controls on calcite recrystallization: Environmental Science & Technology.

Hedström, H., Persson, I., Skarnemark, G., and Ekberg, C., 2013, Characterization of radium sulphate: Journal of Nuclear Chemistry, v. 2013.

Helgeson, H. C., 1978, Summary and critique of the thermodynamic properties of rock-forming minerals: American Journal of Science, v. 278, p. 1-229.

Hemes, S., Desbois, G., Urai, J. L., Schröppel, B., and Schwarz, J.-O., 2015, Multi-scale characterization of porosity in Boom Clay (HADES-level, Mol, Belgium) using a combination of X-ray μ-CT, 2D BIB-SEM and FIB-SEM tomography: Microporous and mesoporous materials, v. 208, p. 1-20.

Herbig, M., Choi, P., and Raabe, D., 2015, Combining structural and chemical information at the nanometer scale by correlative transmission electron microscopy and atom probe tomography: Ultramicroscopy, v. 153, p. 32-39.

Hirner, A. V., 2000, Elutions-und Extraktionsverfahren zur Bestimmung mobiler anorganischer und organischer Kontaminanten in Feststoffen, Analytiker-Taschenbuch, Springer, p. 151-177.

Holzer, L., and Cantoni, M., 2011, Review of FIB-tomography: Nanofabrication using focused ion and electron beams: principles and applications. Oxford University Press, NY. ISBN, v. 559201222.

Holzer, L., Indutnyi, F., Gasser, P., Münch, B., and Wegmann, M., 2004, Three-dimensional analysis of porous BaTiO3 ceramics using FIB nanotomography: Journal of Microscopy, v. 216, no. 1, p. 84-95.

Holzer, L., Münch, B., Rizzi, M., Wepf, R., Marschall, P., and Graule, T., 2010, 3D-microstructure analysis of hydrated bentonite with cryo-stabilized pore water: Applied clay science, v. 47, no. 3, p. 330-342.

Hönigschmid, O., 1911, Revision des Atomgewichts des Radiums und Herstellung von Radiumstandardpräparaten, Sitz: Ber. Kaiserl. Akad. Wiss. Wien, v. 120, p. 1617-1652.

Horai, K. i., 1971, Thermal conductivity of rock-forming minerals: Journal of Geophysical Research, v. 76, no. 5, p. 1278-1308.

Hövelmann, J., Putnis, A., Geisler, T., Schmidt, B. C., and Golla-Schindler, U., 2010, The replacement of plagioclase feldspars by albite: observations from hydrothermal experiments: Contributions to Mineralogy and Petrology, v. 159, no. 1, p. 43-59.

IAEA, 2012. The Safety Case and Safety Assessment for the Disposal of radioactive Waste. IAEA Safety Standard Series No. SSG-23.

Jacobsen, S. D., Smyth, J. R., Swope, R. J., and Downs, R. T., 1998, Rigid-body character of the SO_4 groups in celestine, anglesite and barite: Canadian mineralogist, v. 36, p. 1053-1060.

Jamieson, J. W., Hannington, M. D., Tivey, M. K., Hansteen, T., Williamson, N. M.-B., Stewart, M., Fietzke, J., Butterfield, D., Frische, M., and Allen, L., 2016, Precipitation and growth of barite within hydrothermal vent deposits from the Endeavour Segment, Juan de Fuca Ridge: Geochimica et Cosmochimica Acta, v. 173, p. 64-85.

Jamtveit, B., and Andersen, T. B., 1992, Morphological instabilities during rapid growth of metamorphic garnets: Physics and Chemistry of Minerals, v. 19, no. 3, p. 176-184.

Jaremalm, M., Köhler, S., and Lidman, F., 2013, Precipitation of barite in the biosphere and its consequences for the mobility of Ra in Forsmark and Simpevarp: SKB report TR-13-28.

Ji, Y., Kowalski, P. M., Neumeier, S., Deissmann, G., Kulriya, P. K., and Gale, J. D., Atomistic modeling and experimental studies of radiation damage in monazite-type $LaPO_4$ ceramics: Nuclear Instruments and Methods in Physics Research Section B: Beam Interactions with Materials and Atoms.

Jonas, L., John, T., King, H. E., Geisler, T., and Putnis, A., 2014, The role of grain boundaries and transient porosity in rocks as fluid pathways for reaction front propagation: Earth and Planetary Science Letters, v. 386, p. 64-74.

Jucker, H., 1954, Über die Mitfällung von Radium mit Bariumsulfat und seine Anreicherung und Bestimmung in Gemischen mit Bariumsalz: Diss. Naturwiss. ETH Zürich.

Jucker, H., and Treadwell, W., 1954, Über die Mitfällung von Radium mit Bariumsulfat: Helvetica Chimica Acta, v. 37, no. 7, p. 2002-2010.

Judat, B., and Kind, M., 2004, Morphology and internal structure of barium sulfate—derivation of a new growth mechanism: Journal of Colloid and Interface Science, v. 269, no. 2, p. 341-353.

Jurado-Vargas, M., Oliguín, M. T., Erdóñez-Regil, E., and Miménez-Reyes, M., 1997, Ion exchange of radium and barium in zeolites: Journal of Radioanalytical and Nuclear Chemistry, v. 218, no. 2, p. 153-156.

Kashchiev, D., and van Rosmalen, G. M., 2003, Review: Nucleation in solutions revisited: Crystal Research and Technology, v. 38, no. 7-8, p. 555-574.

Kelly, T. F., and Larson, D. J., 2012, Atom probe tomography 2012: Annual Review of Materials Research, v. 42, p. 1-31.

Kim, J.-S., Kwon, S.-K., Sanchez, M., and Cho, G.-C., 2011, Geological storage of high level nuclear waste: KSCE Journal of Civil Engineering, v. 15, no. 4, p. 721-737.

Klinkenberg, M., Brandt, F., Breuer, U., and Bosbach, D., 2014, Uptake of Ra during the recrystallization of barite: a microscopic and time of flight-secondary ion mass spectrometry study: Environmental science & technology, v. 48, no. 12, p. 6620-6627.

Kolowrat, L., 1910, Sur le dégagement de l'émanation par les sels de radium. Radium, v.7, no.9, 266-269.

Krest, J. M., and Harvey, J. W., 2003, Using natural distributions of short-lived radium isotopes to quantify groundwater discharge and recharge: Limnology and Oceanography, v. 48, no. 1, p. 290-298.

La Fontaine, A., Zavgorodniy, A., Liu, H., Zheng, R., Swain, M., and Cairney, J., 2016, Atomic-scale compositional mapping reveals Mg-rich amorphous calcium phosphate in human dental enamel: Science Advances, v. 2, no. 9, p. e1601145.

Labotka, T., Cole, D. R., Fayek, M., and Riciputi, L. R., 2002, Coupled cation and oxygen exchange between alkali feldspar and aqueous chloride solution: Geochim Cosmochim Acta, v. 66, p. A427.

Langmuir, D., and Melchior, D., 1985, The geochemistry of Ca, Sr, Ba and Ra sulfates in some deep brines from the Palo Duro Basin, Texas: Geochimica et Cosmochimica Acta, v. 49, no. 11, p. 2423-2432.

Langmuir, D., and Riese, A. C., 1985, The thermodynamic properties of radium: Geochimica et cosmochimica acta, v. 49, no. 7, p. 1593-1601.

Lasaga, A. C., and Luttge, A., 2001, Variation of crystal dissolution rate based on a dissolution stepwave model: Science, v. 291, no. 5512, p. 2400-2404.

Lind, S. C., Underwood, J. E., and Whittemore, C. F., 1918, The solubility of pure radium sulfate Journal of the American Chemical Society, v. 40, no. 3, p. 465-472.

Lippmann, F., 1977, The solubility products of complex minerals, mixed crystals, and three-layer clay minerals: N. Jb. Miner. Abh, v. 130, no. 3, p. 243-263.

Lorens, R. B., 1978, A Study of Biological and physical contronls on the trace metal content of calcite and aragonite, PhD thesis.

Lorens, R. B., 1981, Sr, Cd, Mn and Co distribution coefficients in calcite as a function of calcite precipitation rate: Geochimica et Cosmochimica Acta, v. 45, no. 4, p. 553-561.

Luedeking, C., and Wheeler, H., 1891, Notes on a Missouri barite: American Journal of Science, no. 252, p. 495-498.

Majumdar, A. S., King, H. E., John, T., Kusebauch, C., and Putnis, A., 2014, Pseudomorphic replacement of diopside during interaction with (Ni, Mg) Cl 2 aqueous solutions: Implications for the Ni-enrichment mechanism in talc-and serpentine-type phases: Chemical Geology, v. 380, p. 27-40.

Martin, T. L., Coe, C., Bagot, P. A. J., Morrall, P., Smith, G. D. W., Scott, T., and Moody, M. P., 2016, Atomic-scale Studies of Uranium Oxidation and Corrosion by Water Vapour: Scientific Reports, v. 6, p. 10.

Mayer, J., Giannuzzi, L. A., Kamino, T., and Michael, J., 2007, TEM sample preparation and FIB-induced damage: Mrs Bulletin, v. 32, no. 05, p. 400-407.

McLaren, A. C., 2005, Transmission electron microscopy of minerals and rocks, Cambridge University Press.

Meakin, P., 1992, Aggregation kinetics: Physica Scripta, v. 46, no. 4, p. 295.

Melcher, A. C., 1910, The solubility of silver chloride, barium sulphate, and calcium sulphate at high temperatures: Journal of the American Chemical Society, v. 32, no. 1, p. 50-66.

Merigoux, H., 1967, Etude de la mobilite de l'oxygene dans les feldspaths alcalins. PhD thesis.

Miller, M., Russell, K., and Thompson, G., 2005, Strategies for fabricating atom probe specimens with a dual beam FIB: Ultramicroscopy, v. 102, no. 4, p. 287-298.

Miller, M. K., and Forbes, R. G., 2014, The Local Electrode Atom Probe, Atom-Probe Tomography, Springer, p. 229-258.

Miller, M. K., Russell, K. F., Thompson, K., Alvis, R., and Larson, D. J., 2007, Review of atom probe FIB-based specimen preparation methods: Microscopy and Microanalysis, v. 13, no. 06, p. 428-436.

Milman, V., and Winkler, B., 1999, Ab initio modeling in crystallography: International Journal of Inorganic Materials, v. 1, no. 3, p. 273-279.

Milvy, P., and Cothern, C. R., 1989, Naturally occurring radionuclides in drinking water: An exercise in risk benefit analysis: Environmental geochemistry and health, v. 11, no. 2, p. 63-72.

Minkoff, I., and Lux, B., 1974, Instability criteria for growth of a hopper crystal related to spiral eutectic morphology: Journal of Crystal Growth, v. 22, no. 2, p. 163-165.

Morales, L. F. G., Mainprice, D., and Boudier, F., 2013, The influence of hydrous phases on the microstructure and seismic properties of a hydrated mantle rock: Tectonophysics, v. 594, p. 103-117.

Morey, G. W., and Hesselgesser, J. M., 1951, The solubility of some minerals in superheated steam at high pressures: Economic Geology, v. 46, no. 8, p. 821-835.

Morse, J. W., Arvidson, R. S., and Lüttge, A., 2007, Calcium Carbonate Formation and Dissolution: Chemical Reviews, v. 107, no. 2, p. 342-381.

Morse, J. W., and Bender, M. L., 1990, Partition coefficients in calcite: Examination of factors influencing the validity of experimental results and their application to natural systems: Chemical Geology, v. 82, p. 265-277.

Mullin, J. W., 2001, Crystallization, Butterworth-Heinemann. 610 p.

Nabhani, K. A., Khan, F., and Yang, M., 2016, Technologically Enhanced Naturally Occurring Radioactive Materials in oil and gas production: A silent killer: Process Safety and Environmental Protection, v. 99, p. 237-247.

Naehr, T., Stakes, D., and Moore, W., 2000, Mass wasting, ephemeral fluid flow, and barite deposition on the California continental margin: Geology, v. 28, no. 4, p. 315-318.

NAGRA, 2014. Technischer Bericht NTW 14-03. Charakteristische Dosisintervalle und Unterlagen zur Bewertung der Barrierensysteme.

Neuman, E. W., 1933, Solubility relations of barium sulfate in aqueous solutions of strong electrolytes: Journal of the American Chemical Society, v. 55, no. 3, p. 879-884.

Niedermeier, D. R., Putnis, A., Geisler, T., Golla-Schindler, U., and Putnis, C. V., 2009, The mechanism of cation and oxygen isotope exchange in alkali feldspars under hydrothermal conditions: Contributions to Mineralogy and Petrology, v. 157, no. 1, p. 65-76.

Nielsen, A. S., Batchelder, D., and Pyrz, R., 2002, Estimation of crystallinity of isotactic polypropylene using Raman spectroscopy: Polymer, v. 43, no. 9, p. 2671-2676.

Nikitin, B., and Tolmatscheff, P., 1933, Ein Beitrag zur Gültigkeit der Massenwirkungsgesetzes II. Quantitative Bestimmung der Löslichkeit des Radiumsulfates in Natriumsulfatlosungen und in Wasser: Z Phys Chem A, v. 167.

Noguchi, T., Arasaki, H., Oomori, T., and Takada, J., 2004, Age determination of submarine hydrothermal barite deposits by the ^{210}Pb/^{226}Ra method: Bunseki Kagaku (Japan Analyst), v. 53, no. 9, p. 1009-1013.

Ojovan, M. I., and Lee, W. E., 2011, Glassy wasteforms for nuclear waste immobilization: Metallurgical and Materials Transactions A, v. 42, no. 4, p. 837-851.

Okrusch, M., and Matthes, S., 2013, Mineralogie: eine Einführung in die spezielle Mineralogie, Petrologie und Lagerstättenkunde, Springer-Verlag.

O'Neil, J. R., and Taylor, H. P., 1967, The oxygen isotope and cation exchange chemistry of feldspars: American Mineralogist, v. 52, p. 1414-1437.

Paige, C., Kornicker, W., Hileman, O., and Snodgrass, W., 1998, Solution Equilibria for Uranium Ore Processing: The $BaSO_4$-H_2SO_4-H_2O System and the $RaSO_4$-H_2SO_4-H_2O System: Geochimica et cosmochimica acta, v. 62, no. 1, p. 15-23.

Parr, D. F., and Chang, L. L., 1980, Descriptive mineralogy of Pugh Quarry, northwestern Ohio: barite and celestite.

Paytan, A., Moore, W., and Kastner, M., 1996, Sedimentation rate as determined by 226 Ra activity in marine barite: Geochimica et Cosmochimica Acta, v. 60, no. 22, p. 4313-4319.

Pedrosa, E., Putnis, C., Renard, F., Burgos-Cara, A., Laurich, B., and Putnis, A., 2016, Porosity generated during the fluid-mediated replacement of calcite by fluorite: CrystEngComm, v. 18, no. 36, p. 6867-6874.

Pedrosa, E. T., Putnis, C. V., and Putnis, A., 2016, The pseudomorphic replacement of marble by apatite: The role of fluid composition: Chemical Geology, v. 425, p. 1-11.

Perdikouri, C., Kasioptas, A., Geisler, T., Schmidt, B. C., and Putnis, A., 2011, Experimental study of the aragonite to calcite transition in aqueous solution: Geochimica et Cosmochimica Acta, v. 75, no. 20, p. 6211-6224.

Perea, D. E., Liu, J., Bartrand, J., Dicken, Q., Thevuthasan, S. T., Browning, N. D., and Evans, J. E., 2016, Atom Probe Tomographic Mapping Directly Reveals the Atomic Distribution of Phosphorus in Resin Embedded Ferritin: Scientific Reports, v. 6, p. 22321.

Pérez-Huerta, A., Laiginhas, F., Reinhard, D. A., Prosa, T. J., and Martens, R. L., 2016, Atom probe tomography (APT) of carbonate minerals: Micron, v. 80, p. 83-89.

Piazolo, S., La Fontaine, A., Trimby, P., Harley, S., Yang, L., Armstrong, R., and Cairney, J. M., 2016, Deformation-induced trace element redistribution in zircon revealed using atom probe tomography: Nat Commun, v. 7.

Pina, C. M., Becker, U., Risthaus, P., Bosbach, D., and Putnis, A., 1998, Molecular-scale mechanisms of crystal growth in barite: Nature, v. 395, no. 6701, p. 483-486.

Pinto, A. J., Jimenez, A., and Prieto, M., 2009, Interaction of phosphate-bearing solutions with gypsum: Epitaxy and induced twinning of brushite ($CaHPO_4 \cdot 2H_2O$) on the gypsum cleavage surface: American Mineralogist, v. 94, no. 2-3, p. 313-322.

Pinto, A. J., Ruiz-Agudo, E., Putnis, C. V., Putnis, A., Jiménez, A., and Prieto, M., 2010, AFM study of the epitaxial growth of brushite ($CaHPO_4 \cdot 2H_2O$) on gypsum cleavage surfaces: American Mineralogist, v. 95, no. 11-12, p. 1747-1757.

Pitzer, K. S., 1973, Thermodynamics of electrolytes. I. Theoretical basis and general equations: The Journal of Physical Chemistry, v. 77, no. 2, p. 268-277.

Plummer, L., and Busenberg, E., 1987, Thermodynamics of aragonite-strontianite solid solutions: Results from stoichiometric solubility at 25 and 76 C: Geochimica et Cosmochimica Acta, v. 51, no. 6, p. 1393-1411.

Poinssot, C., and Geckeis, H., 2015, Radionuclide behaviour in the natural environment: an overview: Environmental Remediation and Restoration of Contaminated Nuclear and Norm Sites, p. 57.

Pollok, K., Putnis, C. V., and Putnis, A., 2011, Mineral replacement reactions in solid solution-aqueous solution systems: Volume changes, reactions paths and end-points using the example of model salt systems: American Journal of Science, v. 311, no. 3, p. 211-236.

Poonoosamy, J., Curti, E., Kosakowski, G., Grolimund, D., Van Loon, L., and Mäder, U., 2016, Barite precipitation following celestite dissolution in a porous medium: A SEM/BSE and μ-XRD/XRF study: Geochimica et Cosmochimica Acta, v. 182, p. 131-144.

Posiva, 2014. Safety Case for the Disposal of Spent Nuclear Fuel at Olkiluoto. FEP Screening and Processing. Posiva 2014-3.

Posiva, 2015. General time schedule for Final Disposal. http://www.posiva.fi/en/final_disposal/general_time_schedule_for_final_disposal#.WDVTUDVA57E. Abgerufen am 23.11.2016.

Pratt, R., 1993, Review of radium hazards and regulation of radium in industry: Environment international, v. 19, no. 5, p. 475-489.

Prieto, M., 2009, Thermodynamics of solid solution-aqueous solution systems: Reviews in Mineralogy and Geochemistry, v. 70, no. 1, p. 47-85.

Prieto, M., 2010, Thermodynamics of ion partitioning in solid solution-aqueous solution systems: European Mineralogical Union Notes in Mineralogy.

Prieto, M., 2014, Nucleation and supersaturation in porous media (revisited): Mineralogical Magazine, v. 78, no. 6, p. 1437-1448.

Prieto, M., Astilleros, J. M., and Fernández-Díaz, L., 2013, Environmental remediation by crystallization of solid solutions: Elements, v. 9, no. 3, p. 195-201.

Prieto, M., Heberling, F., Rodríguez-Galán, R. M., and Brandt, F., 2016, Crystallization behavior of solid solutions from aqueous solutions: An environmental perspective: Progress in Crystal Growth and Characterization of Materials.

Puchelt, H., 1967, Zur Geochemie des Bariums im exogenen Zyklus, Springer.

Putnis, A., 2002, Mineral replacement reactions: from macroscopic observations to microscopic mechanisms: Mineralogical Magazine, v. 66, no. 5, p. 689-708.

Putnis, A., 2009, Mineral replacement reactions: Reviews in mineralogy and geochemistry, v. 70, no. 1, p. 87-124.

Putnis, A., and Austrheim, H., 2013, Mechanisms of metasomatism and metamorphism on the local mineral scale: the role of dissolution-reprecipitation during mineral re-equilibration, Metasomatism and the Chemical Transformation of Rock, Springer, p. 141-170.

Putnis, A., and Putnis, C. V., 2007, The mechanism of reequilibration of solids in the presence of a fluid phase: Journal of Solid State Chemistry, v. 180, no. 5, p. 1783-1786.

Putnis, C. V., Geisler, T., Schmid-Beurmann, P., Stephan, T., and Giampaolo, C., 2007, An experimental study of the replacement of leucite by analcime: American Mineralogist, v. 92, no. 1, p. 19-26.

Putnis, C. V., Renard, F. o., King, H. E., Montes-Hernandez, G., and Ruiz-Agudo, E., 2013, Sequestration of selenium on calcite surfaces revealed by nanoscale imaging: Environmental science & technology, v. 47, no. 23, p. 13469-13476.

Putnis, C. V., Tsukamoto, K., and Nishimura, Y., 2005, Letter. Direct observations of pseudomorphism: compositional and textural evolution at a fluid-solid interface: American Mineralogist, v. 90, no. 11-12, p. 1909-1912.

Qian, G., Brugger, J., Skinner, W. M., Chen, G., and Pring, A., 2010, An experimental study of the mechanism of the replacement of magnetite by pyrite up to 300 C: Geochimica et Cosmochimica Acta, v. 74, no. 19, p. 5610-5630.

Raabe, O., 1989, Scaling of fatal cancer risks from laboratory animals to man: Health physics, v. 57, p. 419-432.

Rajabzadeh, M., 2007, A fluid inclusion study of a large MVT barite-fluorite deposit: Komshecheh, Central Iran: Iranian Journal of Science and Technology (Sciences), v. 31, no. 1, p. 73-87.

Řanda, Z., Ulrych, J., Turek, K., Mihaljevič, M., Adamovič, J., and Mizera, J., 2010, Radiobarites from the Cenozoic volcanic region of the Bohemian Massif: radiochemical study, history, and lead isotopic composition: Journal of radioanalytical and nuclear chemistry, v. 283, no. 1, p. 89-94.

Raufaste, C., Jamtveit, B., John, T., Meakin, P., and Dysthe, D. K., 2011, The mechanism of porosity formation during solvent-mediated phase transformations, in Proceedings Proceedings of the Royal Society of London A: Mathematical, Physical and Engineering Sciences, Volume 467, The Royal Society, p. 1408-1426.

Ray, I. L. F., Thiele, H., and Matzke, H., 1992, Transmission electron microscopy study of fission product behaviour in high burnup UO2: Journal of Nuclear Materials, v. 188, p. 90-95.

Renock, D., Landis, J. D., and Sharma, M., 2016, Reductive weathering of black shale and release of barium during hydraulic fracturing: Applied Geochemistry, v. 65, p. 73-86.

Rihs, S., and Condomines, M., 2002, An improved method for Ra isotope (^{226}Ra, ^{228}Ra, ^{224}Ra) measurements by gamma spectrometry in natural waters: application to CO_2-rich thermal waters from the French Massif Central: Chemical Geology, v. 182, no. 2, p. 409-421.

Roden, E. E., Leonardo, M. R., and Ferris, F. G., 2002, Immobilization of strontium during iron biomineralization coupled to dissimilatory hydrous ferric oxide reduction: Geochimica et Cosmochimica Acta, v. 66, no. 16, p. 2823-2839.

Röhlig, K. J., Geckeis, H., and Mengel, K., 2012, Endlagerung radioaktiver Abfälle: Chemie in unserer Zeit, v. 46, no. 3, p. 140-149.

Rosenberg, Y. O., Metz, V., and Ganor, J., 2011, Co-precipitation of radium in high ionic strength systems: 1. Thermodynamic properties of the $Na–Ra–Cl–SO_4–H_2O$ system – Estimating Pitzer parameters for $RaCl_2$: Geochimica et Cosmochimica Acta, v. 75, no. 19, p. 5389-5402.

Ruiz-Agudo, C., Ruiz-Agudo, E. n., Putnis, C. V., and Putnis, A., 2015, Mechanistic Principles of Barite Formation: From Nanoparticles to Micron-Sized Crystals: Crystal Growth & Design, v. 15, no. 8, p. 3724-3733.

Ruiz-Agudo, E., Álvarez-Lloret, P., Ibañez-Velasco, A., and Ortega-Huertas, M., 2016, Crystallographic Control in the Replacement of Calcite by Calcium Sulfates: Crystal Growth & Design, v. 16, no. 9, p. 4950-4959.

Ruiz-Agudo, E., Álvarez-Lloret, P., Putnis, C., Rodriguez-Navarro, A., and Putnis, A., 2013, Influence of chemical and structural factors on the calcite–calcium oxalate transformation: CrystEngComm, v. 15, no. 46, p. 9968-9979.

Ruiz-Agudo, E., Kudłacz, K., Putnis, C. V., Putnis, A., and Rodriguez-Navarro, C., 2013, Dissolution and carbonation of portlandite [Ca $(OH)_2$] single crystals: Environmental science & technology, v. 47, no. 19, p. 11342-11349.

Ruiz-Agudo, E., Putnis, C., and Putnis, A., 2014, Coupled dissolution and precipitation at mineral–fluid interfaces: Chemical Geology, v. 383, p. 132-146.

Sachtleben, 2015. Safety Data Sheet according to Regulation (EC) No 1907/2006 to 1272/2008. Print date: 09.06.2015 http://www.sachtleben.de/fileadmin/safety_data_sheets/blanc_fixe_xr_series_en.pdf (Access date: 30.11.2015).

Schmidt, J. E., Poplawsky, J. D., Mazumder, B., Attila, Ö., Fu, D., de Winter, D. A. M., Meirer, F., Bare, S. R., and Weckhuysen, B. M., 2016, Coke Formation in a Zeolite Crystal During the Methanol-to-Hydrocarbons Reaction as Studied with Atom Probe Tomography: Angewandte Chemie International Edition, v. 55, no. 37, p. 11173-11177.

Schneiderhöhn, H., 1949, Schwerspatgänge und pseudomorphe Quarzgänge in Westdeutschland: N. Jb. Miner. Geol. Paläont., Monatsh. A, p. 191-202.

Shannon, R.T., 1976, Revised Effective Ionic Radii and Systematic Studies of Interatomic Distances in Halides and Chalcohalogenides, Acta Crystallographica Section A: Crystal Physics, Diffraction, Theoretical and General Crystallography, v. 32, no.5, p.751-767.

Shao, H., Dmytrieva, S. V., Kolditz, O., Kulik, D. A., Pfingsten, W., and Kosakowski, G., 2009, Modeling reactive transport in non-ideal aqueous–solid solution system: Applied Geochemistry, v. 24, no. 7, p. 1287-1300.

Sheen, S., Lee, K. S., Chung, W. Y., Nam, S., and Kang, D. R., 2016, An updated review of case–control studies of lung cancer and indoor radon-Is indoor radon the risk factor for lung cancer?: Annals of occupational and environmental medicine, v. 28, no. 1, p. 1.

SKB, 2010. Metodval – utvärdering av strategier och system för att ta hand om använt kärnbränsle.

SKB, 2011. Long-term safety for the final repository of spent nuclear fuel at Forsmark Main report of the Sr-site project I-III.

Somlai, J., Horváth, G., Kanyár, B., Kovács, T., Bodrogi, E., and Kávási, N., 2002, Concentration of 226Ra in Hungarian bottled mineral water: Journal of Environmental Radioactivity, v. 62, no. 3, p. 235-240.

Stack, A. G., 2009, Molecular Dynamics Simulations of Solvation and Kink Site Formation at the {001} Barite−Water Interface: The Journal of Physical Chemistry C, v. 113, no. 6, p. 2104-2110.

Stack, A. G., 2015, Precipitation in pores: A geochemical frontier: Rev Mineral Geochem, v. 80, p. 165-190.

Stack, A. G., and Rustad, J. R., 2007, Structure and dynamics of water on aqueous barium ion and the {001} barite surface: The Journal of Physical Chemistry C, v. 111, no. 44, p. 16387-16391.

Stevie, L.A., Irwin, R.B., Shofner, T.L., Brown, S.R., Drown, J.L., Giannuzzi, L.A., 1998, Plan view TEM sample preparation using the focused ion beam lift-out technique. AIP Conferece Proceedings, v.449, p. 868.

Sturchio, N. C., 1990, Radium isotopes, alkaline earth diagenesis, and age determination of travertine from Mammoth Hot Springs, Wyoming, USA: Applied Geochemistry, v. 5, no. 5-6, p. 631-640.

Sturchio, N. C., Bohlke, J. K., and Markun, F. J., 1993, Radium isotope geochemistry of thermal waters, Yellowstone National Park, Wyoming, USA: Geochimica et Cosmochimica Acta, v. 57, no. 6, p. 1203-1214.

Sun, H., and Semkow, T. M., 1998, Mobilization of thorium, radium and radon radionuclides in ground water by successive alpha-recoils: Journal of Hydrology, v. 205, no. 1, p. 126-136.

Sutherland, D. N., 1970, Chain formation of fine particle aggregates: Nature, v.226, p. 1241-1242.

Takamizawa, H., Shimizu, Y., Inoue, K., Nozawa, Y., Toyama, T., Yano, F., Inoue, M., Nishida, A., and Nagai, Y., 2016, Predoping effects of boron and phosphorous on arsenic diffusion along grain boundaries in polycrystalline silicon investigated by atom probe tomography: Applied Physics Express, v. 9, no. 10, p. 106601.

Taylor, L. S., and Zografi, G., 1998, The quantitative analysis of crystallinity using FT-Raman spectroscopy: Pharmaceutical research, v. 15, no. 5, p. 755-761.

Templeton, C. C., 1960, Solubility of Barium Sulfate in Sodium Chloride Solutions from 25° to 95° C: Journal of Chemical and Engineering Data, v. 5, no. 4, p. 514-516.

Tesoriero, A. J., and Pankow, J. F., 1996, Solid solution partitioning of Sr^{2+}, Ba^{2+}, and Cd^{2+} to calcite: Geochimica et Cosmochimica Acta, v. 60, no. 6, p. 1053-1063.

Thiele, H., Hoppe, K., and Moll, G., 1962, Über das kolloide Gold: Colloid & Polymer Science, v. 185, no. 1, p. 45-52.

Thien, B. M., Kulik, D. A., and Curti, E., 2014, A unified approach to model uptake kinetics of trace elements in complex aqueous–solid solution systems: Applied Geochemistry, v. 41, p. 135-150.

Thoenen, T., Hummel, W., Berner, U., and Curti, E., 2014, The PSI/Nagra Chemical Thermodynamic Database 12/07.

Thomas, J. and Gemming, T. Analytical Transmission Electron Microscopy: An Introduction for Operators, Springer, 357 p.

Thompson, K., Lawrence, D., Larson, D., Olson, J., Kelly, T., and Gorman, B., 2007, In situ site-specific specimen preparation for atom probe tomography: Ultramicroscopy, v. 107, no. 2, p. 131-139.

Torapava, N., Ramebäck, H., Curti, E., Lagerkvist, P., and Ekberg, C., 2014, Recrystallization of 223Ra with barium sulfate: Journal of Radioanalytical and Nuclear Chemistry, v. 301, no. 2, p. 545-553.

Uchameyshvili, N., Malinin, S., and Khitarov, N., 1966, Solubility of barite in concentrated chloride solutions of some metals at elevated temperatures in relation to problems of genesis of barite deposits, Geochemistry International USSR, v. 3, p. 951.

Valley, J. W., Cavosie, A. J., Ushikubo, T., Reinhard, D. A., Lawrence, D. F., Larson, D. J., Clifton, P. H., Kelly, T. F., Wilde, S. A., and Moser, D. E., 2014, Hadean age for a post-magma-ocean zircon confirmed by atom-probe tomography: Nature Geoscience, v. 7, no. 3, p. 219-223.

Valley, J. W., Reinhard, D. A., Cavosie, A. J., Ushikubo, T., Lawrence, D. F., Larson, D. J., Kelly, T. F., Snoeyenbos, D. R., and Strickland, A., 2015, Presidential Address. Nano-and micro-geochronology in Hadean and Archean zircons by atom-probe tomography and SIMS: New tools for old minerals: American Mineralogist, v. 100, no. 7, p. 1355-1377.

Van den Berghe, S., Van Renterghem, W., and Leenaers, A., 2008, Transmission electron microscopy investigation of irradiated U–7 wt% Mo dispersion fuel: Journal of Nuclear Materials, v. 375, no. 3, p. 340-346.

Vinograd, V., Brandt, F., Rozov, K., Klinkenberg, M., Refson, K., Winkler, B., and Bosbach, D., 2013, Solid–aqueous equilibrium in the BaSO 4–RaSO 4–H 2 O system: first-principles calculations and a thermodynamic assessment: Geochimica et Cosmochimica Acta, v. 122, p. 398-417.

Vurpillot, F., Bostel, A., and Blavette, D., 2000, Trajectory overlaps and local magnification in three-dimensional atom probe: Applied Physics Letters, v. 76, no. 21, p. 3127-3129.

Wang, R. S., Yang, X. N., and Wu, Q. Y., 1993, Study of the immobilization of226Ra: Journal of Radioanalytical and Nuclear Chemistry, v. 198, no. 2, p. 281-285.

Warren, S., 1980, Effects of radiation on normal tissues: CA: A Cancer Journal for Clinicians, v. 30, no. 6, p. 350-355.

Weigel, F., and Trinkl, A., 1968, Crystal chemistry of radium I radium halides: Radiochimica Acta v. 9, no. 1, p. 36-38.

Weigel, F., and Trinkl, A., 1968, Crystal chemistry of radium III preparation, crystal structure and atomic radius of metallic radium Univ., Munich. Technische Hochschule, Munich.

Weigel, F., and Trinkl, A., 1968, Crystal chemistry of radium, II, radium salts of the type $RaXO_4$, X=S,Se,Cr,Mo,W: Univ., Munich. Technische Hochschule, Garching, Ger.

Widanagamage, I. H., Griffith, E. M., Singer, D. M., Scher, H. D., Buckley, W. P., and Senko, J. M., 2015, Controls on stable Sr-isotope fractionation in continental barite: Chemical Geology, v. 411, p. 215-227.

Widanagamage, I. H., Schauble, E. A., Scher, H. D., and Griffith, E. M., 2014, Stable strontium isotope fractionation in synthetic barite: Geochimica Et Cosmochimica Acta, v. 147, p. 58-75.

Wilkinson, J. J., 2001, Fluid inclusions in hydrothermal ore deposits: Lithos, v. 55, no. 1–4, p. 229-272.

Williams, D. B., and Carter, C., 2009, Transmission Electron Microscopy: A Text Book for Materials Science. Springer: New York.

Winkler, B., 1999, An introduction to “Computational Crystallography”, Zeitschrift für Kristallographie - Crystalline Materials, Volume 214, p. 506.

Winter, D., DE, M., Schneijdenberg, C., Lebbink, M., Lich, B., Verkleij, A., Drury, M., and Humbel, B., 2009, Tomography of insulating biological and geological materials using focused ion beam (FIB) sectioning and low- kV BSE imaging: Journal of microscopy, v. 233, no. 3, p. 372-383.

Workman, D., and Cowperthwaite, I., 1963, An occurrence of kyanite pseudomorphing andalusite from Southern Rhodesia: Geological Magazine, v. 100, no. 05, p. 456-466.

Wyart, J. t., and Sabatier, G., 1958, Mobilite des ions silicium et aluminum dans les cristaux de feldspath: Bull Soc fr Minéral Cristallogr, v. 81, p. 223-226.

Yoshida, Y., Nakazawa, T., Yoshikawa, H., and Nakanishi, T., 2009, Partition coefficient of Ra in gypsum: Journal of radioanalytical and nuclear chemistry, v. 280, no. 3, p. 541-545.

Zaitseva, N., and Carman, L., 2001, Rapid growth of KDP-type crystals: Progress in crystal growth and characterization of materials, v. 43, no. 1, p. 1-118.

Zangwill, A., 1988, Physics at surfaces, Cambridge university press.

Zhang, T., Bain, D., Hammack, R., and Vidic, R. D., 2015, Analysis of Radium-226 in High Salinity Wastewater from Unconventional Gas Extraction by Inductively Coupled Plasma-Mass Spectrometry: Environmental Science & Technology, v. 49, no. 5, p. 2969-2976.

Zhang, T., Gregory, K., and Hammack, R. W., 2015, Co-Precipitation of Radium with Barium and Strontium Sulfate and Its Impact on the Fate of Radium during

Treatment of Produced Water from Unconventional Gas Extraction: Wastewater and Shale Formation Development: Risks, Mitigation, and Regulation, v. 48, p. 159.

Zhang, T., Gregory, K., Hammack, R. W., and Vidic, R. D., 2014, Co-precipitation of radium with barium and strontium sulfate and its impact on the fate of radium during treatment of produced water from unconventional gas extraction: Environmental science & technology, v. 48, no. 8, p. 4596-4603.

Zhang, Y., 2008, Geochemical kinetics, Princeton University Press.

Zhang, Y., Ni, H., and Chen, Y., 2010, Diffusion data in silicate melts: Reviews in Mineralogy and Geochemistry, v. 72, no. 1, p. 311-408.

Zhong, S., and Mucci, A., 1995, Partitioning of rare earth elements (REEs) between calcite and seawater solutions at 25°C and 1 atm, and high dissolved REE concentrations: Geochimica et Cosmochimica Acta, v. 59, no. 3, p. 443-453.

Zhu, C., 2004, Coprecipitation in the barite isostructural family: 2. Numerical simulations of reactions and mass transport: Geochimica et cosmochimica acta, v. 68, no. 16, p. 3339-3349.

Zielinski, R., Otton, J., and Budahn, J., 2001, Use of radium isotopes to determine the age and origin of radioactive barite at oil-field production sites: Environmental Pollution, v. 113, no. 3, p. 299-309.

Zou, H., Zhang, S. t., Chen, A. q., Fang, Y., and Zeng, Z. f., 2016, Hydrothermal Fluid Sources of the Fengjia Barite–fluorite Deposit in Southeast Sichuan, China: Evidence from Fluid Inclusions and Hydrogen and Oxygen Isotopes: Resource Geology, v. 66, no. 1, p. 24-36.

Standortauswahlgesetz vom 23.Juli 2013 (BGBI. I S. 2553), das durch den Artikel 2 des Gesetzes vom 26. Juli 2016 (BGBI.I S.1843) geändert worden ist § 3 Kommission Lagerung hochradioaktiver Abfälle

11 Acknowledgments

I am greatly thankful to Prof. Dr. Bosbach for giving me the opportunity to conduct my PhD research at his institute, the fruitful discussion about my results and his support. Prof. Dr. Roth is thanked for his willingness to be my second corrector and I am very thankful for the time we spent discussing my results.

The Swedish waste management agency SKB is acknowledged for the partial funding of this study. Especially, Prof. Dr. Kastriot Spahiu and Dr. Lena Zetterström-Evins are thanked for making this thesis work possible.

I would like to express my profound gratitude to my supervisors Dr. Felix Brandt and Dr. Martina Klinkenberg for their guidance, the many fruitful discussions and their continuous help. Their doors were always open whenever I had a question and I am deeply grateful for their support.

I would like to especially thank Dr. Juri Barthel for sharing his knowledge, discussing my results, the numerous explanations on electron microscopy and data analysis. Thank you for encouraging me so many times during my PhD.

Special thanks belong to Dr. Uwe Breuer who always had time to discuss my results. I am very thankful to him for sharing his knowledge about mass spectrometry and for supporting me during my PhD.

Prof. Dr. Joachim Mayer is thanked for his continuous support of my research.
Maximilian Kruth is thanked for his continuous support with the FIB preparation, FIB tomography and the TEM characterization.

I would like to express my gratitude to Dr. Guido Deissmann for his advice and his feedback on my texts. I greatly appreciate all the knowledge you shared with me.

Dr. Ivan Povstugar is acknowledged for his support in discussing all the topics in this thesis related to APT and furthermore on his feedback regarding my writings of these parts.

A special gratitude is owed to my office mate, Dr. Sarah Finkeldei, for sharing her expertise and giving me valuable advice.

I am deeply grateful to Dr. Julia Heuser and Dr. Natalia Shcherbina for their help with correction of the manuscript.

Dr. Andrew Stack and Dr. Roland Hellmann are greatly thanked for the fruitful discussion about my research.

Dr. Aleksei Savenko is acknowledged for his support during the FIB preparation of the APT samples and the APT characterization. For the help with the sampling of the experiments and the SEM sample preparation, I would like to thank Rainer Engelmann and Katharina Dahmen. Murat Güngör is thanked for the preparation of numerous FIB cross-sections. Ralf König, Dr. Andreas Wilden and Fabian Sadowski are greatly acknowledged for their dedication to the radiation protection in the controlled area. In addition, I would like to thank Fabian Sadowski for numerous ICP-MS analyses. Doris Meertens is thanked for her support with the FIB preparations and Werner Pieper for his technical support during the TEM characterizations.

Victor Vinograd is acknowledged for answering all my questions related to thermodynamics of solid solutions.

Dr. Alexandra Yatim is greatly acknowledged for the possibility to use their FIB instrument during maintenance of our instrument and I further would like to thank her for her advice and help.

For his permission to use the computer dedicated to FIB tomography reconstruction containing the Avizo program, I would like to thank Dr. Roland Schierholz.

All my colleagues at the IEK-6 are greatly thanked for the good and pleasant working atmosphere, especially Christian Schreinemachers, Dr. Philip Kegler, Joshua Rutkowski and Dr. Clemens Listner.

Dr. Jenna Poonosamy is thanked for her time to discuss solid solution thermodynamics and for providing the excel file to construct Lippmann diagrams.

I would like to thank Dr. Lurdes Fernandez-Diaz for sharing her knowledge about fluid inclusions in minerals with me. I appreciate your time.

Most important, I would like to especially thank my family and friends. Eva, Lisa, Sarah, Micha, Simon, Nina, Nora and Schazi are especially thanked for their support throughout the last three years.

I would like to thank my whole family for their continuous support during my studies and my PhD thesis. I am especially grateful to my mother, my brother Konrad and my sister Anette.

12 Already published parts of this PhD

Peer-reviewed publications

J. Weber, J. Barthel, F. Brandt, M. Klinkenberg, U. Breuer, M. Kruth, D. Bosbach, 2016. Nano-structural features of barite crystals observed by electron microscopy and atom probe tomography. *Chemical Geology*, 424, 51-59.

Conference presentations

J. Weber, F. Brandt, M. Klinkenberg, J. Barthel, U. Breuer, D. Bosbach, *The uptake of Ra into barite*. National fall meeting of the American Chemical Society, Philadelphia, USA, 2016. **Invited talk.**

J. Weber, F. Brandt, M. Klinkenberg, U. Breuer, J. Barthel, I. Povstugar, D. Bosbach. *$Ba_xRa_{1-x}SO_4$ – nano-structural and chemical investigations by electron microscopy and APT.* Atom Probe Tomography & Microscopy, Gyeongju, South Korea, 2016.

J. Weber, F. Brandt, M. Klinkenberg, U. Breuer, J. Barthel, A. Savenko, D. Bosbach. *Combined Atom Probe Tomography and Scanning Transmission Electron Microscopy characterization of $Ba_xRa_{1-x}SO_4$ solid solutions – enabling the process understanding of Ra uptake into barite.* European APT Workshop, Leoben, Austria, 2015.

J. Weber, F. Brandt, M. Klinkenberg, U. Breuer, J. Barthel, A. Savenko, D. Bosbach. *Advanced Microanalytical Characterization of the $(Ba,Ra)SO_4$ Solid Solution with APT and TEM.* 15th International Conference on the Chemistry and Migration Behaviour of Actinides and Fission Products in the Geospere, Santa Fe, New Mexico, USA.

J. Weber, F. Brandt, M. Klinkenberg, U. Breuer, J. Barthel, A. Savenko, D. Bosbach. *Characterization of $(Ba,Ra)SO_4$ solid solutions on the atomic level by Atom Probe Tomography and Transmission Electron Microscopy.* GdcH Wissenschaftsforum, Dresden, Germany, 2015.

J. Weber, F. Brandt, M. Klinkenberg, U. Breuer, J. Barthel, A. Savenko, D. Bosbach. *Characterization of $(Ba,Ra)SO_4$ solid solutions with true nm-scale resolution.* Goldschmidt Conference in Prague, Czech Republic, 2015.

J. Weber, F. Brandt, M. Klinkenberg, U. Breuer, A. Savenko, J. Barthel, D. Bosbach. *Nano-scale analysis of Ra uptake into barite by TEM and APT.* Second Joint Student Workshop on f-Element Chemistry, Karlsruhe, Germany, 2015. **Award for oral contribution**.

J. Weber, U. Breuer, A. Savenko, M. Klinkenberg, F. Brandt, D. Bosbach. *Method development for the LEAP and TEM characterization of $(Ba,Ra)SO_4$ solid solutions on the atomic level.* Annual meeting of the DMG (German mineralogical society) in Jena, Germany, 2014.

Poster

J. Weber, F. Brandt, M. Klinkenberg, J. Barthel, U. Breuer, D. Bosbach, *The uptake of Ra into barite*. National fall meeting of the American Chemical Society, Philadelphia, USA, 2016.

J. Weber, U. Breuer, A. Savenko, M. Klinkenberg, F. Brandt, D. Bosbach *Ra uptake into barite -Method development for a characterization on the atomic level.* 6th School on Atom Probe Tomography, Rouen, France, 2014.

J. Weber, U. Breuer, A. Savenko, M. Klinkenberg, F. Brandt, D. Bosbach. *Chemical and structural investigations of* $Ba_xRa_{1-x}SO_4$ *on the atomic level by TEM and APT.* Atom Probe Tomography & Microscopy, Stuttgart, Germany, 2014.

J. Weber, F. Brandt, U. Breuer, A. Savenko, M. Klinkenberg, D. Bosbach. *A combined TE M and APT study - Ra uptake into barite.* 8th European Summer School on Separation Chemistry and Conditioning as well as Supramolecular, Intermolecular, Interaggregate Interactions, Bonn, Germany, 2014.

13 Curriculum vitae

10/2013 -ongoing	PhD at RWTH Aachen University / Forschungszentrum Jülich, IEK-6: **Ra uptake into barite**
3/2013 – 10/2013	Master thesis at Forschungszentrum Jülich, IEK-6: **Uptake of radium and solid solution formation in the ternary system of (Ba,Ra,Sr)SO_4**
10/2011 – 10/2013	Master studies of Geosciences, Rheinische Friedrich-Wilhelms-Universität Bonn
3/2013 – 10/2013	Bachelor thesis at Rheinische Friedrich-Wilhelms-Universität Bonn: **Umweltanalyse der Riffe von Abrolhos und Fernando de Noronha, Brasilien, anhand rezenter benthischer Foraminiferen (Environmental analysis of the Abrolhos and Fernando de Noronha reefs, Brazil on the basis of recent, benthic foraminifera analysis)**
10/2008-10/2011	Bachelor studies of Geosciences, Rheinische Friedrich-Wilhelms-Universität Bonn
08/2007-08/2008	Aupair in Virginia, USA
2007	Abitur (German highschool exam with university entrance qualification), Carl-von-Ossietzky-Gymnasium Bonn-Ückesdorf

14 Eidesstattliche Erklärung

Hiermit versichere ich eidesstattlich, dass ich die Dissertation selbstständig verfasst und alle in Anspruch genommenen Hilfen in der Dissertation angegeben habe.

Jülich, den

15 Appendix

Tab. 7 Overview of the Ra concentrations in solution at different recrystallization times of the SL 1 experiment. The highlighted samples were characterized within this doctoral thesis.

Recrystallization time [d]	Ra-concentration [mol/L]
0	5.00E-06
1	4.90E-06
2	4.91E-06
3	4.91E-06
4	4.87E-06
7	4.89E-06
9	4.77E-06
18	4.49E-06
24	4.46E-06
30	4.48E-06
37	4.57E-06
44	4.58E-06
72	4.16E-06
99	4.06E-06
127	4.03E-06
184	2.74E-06
254	3.24E-06
555	4.86E-07
778	2.82E-08
1010	4.23E-08
1193	5.20E-08
1345	5.20E-08

Tab. 8 **Overview of the Ra concentrations in solution at different recrystallization times of the SL 2 experiment. Sampling dates when solid samples were taken and characterized are highlighted. The sample of day 443 was characterized as well by ToF-SIMS (Klinkenberg et al., 2014).**

Recrystallization time [d]	Ra-concentration [mol/L]
0	5.04E-06
1	4.87E-06
7	4.36E-06
14	4.21E-06
21	4.20E-06
28	3.65E-06
42	3.57E-06
70	2.80E-06
98	1.77E-06
127	4.85E-07
154	3.96E-08
182	2.03E-08
238	1.93E-08
337	2.41E-08
350	2.80E-08
443*	3.48E-08
532	4.34E-08
602	5.03E-08
664	6.84E-08
883	8.20E-08

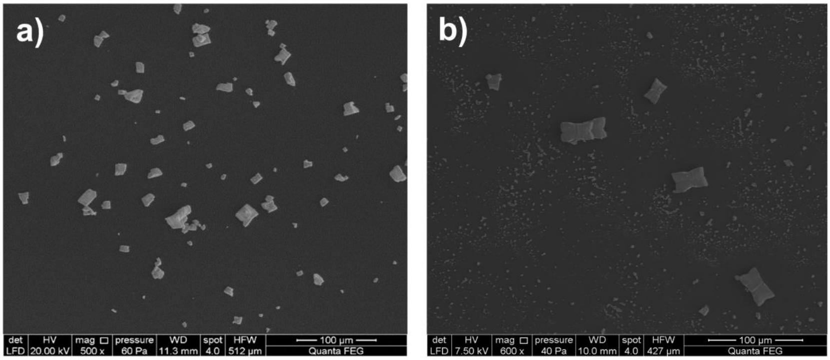

Fig. 54 **SEM characterization of the barite samples prior equilibration and grain size separation via Atterberg sedimentation showing a broad grain size distribution of (a) SL barite an (b) AL barite.**

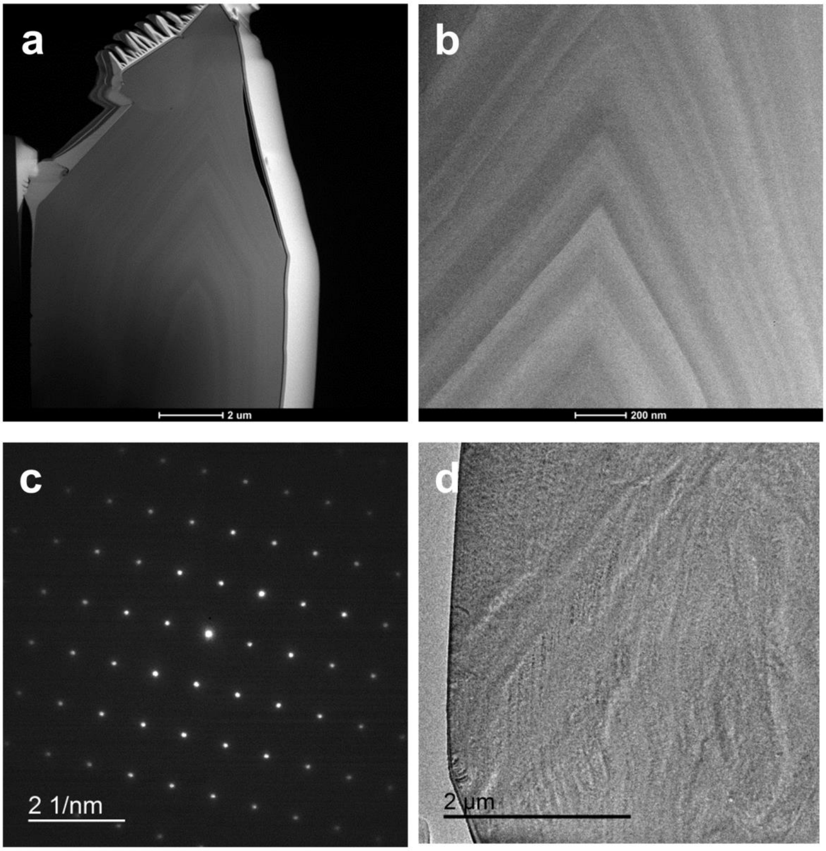

Fig. 55 TEM characterization of SL barite prior equilibration. The layered structure is well recognizable in the HAADF-STEM images (a) and (b). The clear diffraction spots (c) show that the barite particle is crystalline. Furthermore, the layered structure can be observed in TEM-BF imaging (d) as well.

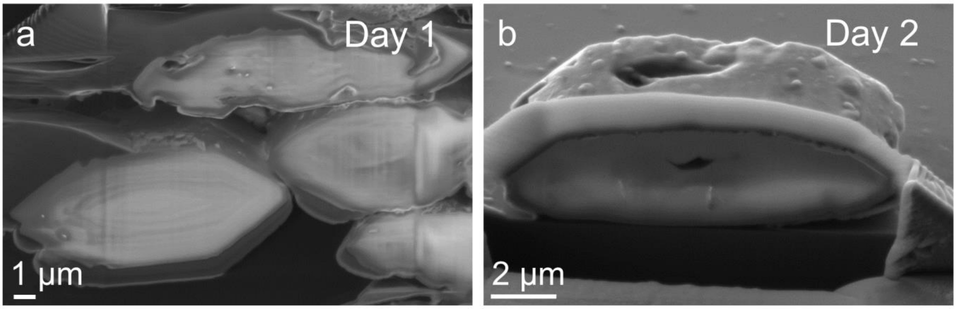

Fig. 56 **SEM images of FIB cross-sections of day 1 (a) and day 2 (b) of the Ra uptake experiments of SL barite. No change within the internal microstructure was observed.**

**Tab. 9 Peaks observed in the mass-to-charge ratio spectrum of the APT measurements of the SL barite and identified ionic species.
Reprinted with permission from Elsevier, Weber et al., 2016 (see p. 101 within this doctoral thesis).**

Barite 1		Barite 1		Barite 2		Barite 2	
m/n	Identified Species	m/n	Identified Species	m/n	Identified Species	m/n	Identified Species
3	H_3^+	82	SO_3^+	2	H_2^+	69	Ba^{2+}
17	OH^+	154	BaO^+	3	H_3^+	69.5	HBa^{2+}
18	H_2O^+	185	$BaSO^+$	17	OH^+	70	H_2Ba^{2+}
19	$(H_2O)H^+$	185.5	$BaSO^+$	18	H_2O^+	76	BaO^{2+}
23	Na^+	186	$BaSO^+$	19	$(H_2O)H^+$	76.5	BaO^{2+}
32	S^+/O_2^+	-	-	23	Na^+	77	BaO^{2+}
33	HS^{+}/HO_2^+	-	-	32	S^+/O_2^+	77.5	BaO^{2+}
35	Cl^+	-	-	33	HS^{+}/HO_2^+	78	BaO^{2+}
43	Sr^{2+}	-	-	34	$S^{+}/H_2O_2^+$	80	SO_3^+
43.5	Sr^{2+}	-	-	35	Cl^+	81	SO_3^+/HSO_3^+
44	Sr^{2+}	-	-	36	HCl^+	82	SO_3^+
48	SO^+	-	-	37	Cl^+	98	$H_2SO_4^+$
64	SO^{2+}	-	-	38	HCl^+	144	$S_2O_5^+$
65	Ba^{2+}	-	-	39	NaO^{2+}	151	BaO^+
66	Ba^{2+}	-	-	43	Sr^{2+}	152	BaO^+
67	Ba^{2+}	-	-	44	Sr^{2+}	153	BaO^+
67.5	Ba^{2+}	-	-	48	SO^+	154	BaO^+
68	Ba^{2+}	-	-	49	H_2SO^+	185	$BaSO^{2+}$
69	Ba^{2+}	-	-	50	H_2SO^+	185.5	$BaSO^{2+}$
69.5	HBa^{2+}	-	-	51	H_2SO^+	186	$BaSO^{2+}$
70	H_2Ba^{2+}	-	-	52	H_2SO^+	187	$BaSO^{2+}$
76	BaO^{2+}	-	-	53	H_2SO^+	230	$BaSO_4^+$
76.5	BaO^{2+}	-	-	64	SO^{2+}	231	$BaSO_4^+$
77	BaO^{2+}	-	-	65	Ba^{2+}	232	$BaSO_4^+$
77.5	BaO^{2+}	-	-	66	Ba^{2+}	233	$BaSO_4^+$
78	BaO^{2+}	-	-	67	Ba^{2+}	234	$BaSO_4^+$
80	SO_3^+	-	-	67.5	Ba^{2+}	235	$BaSO_4^+$
81	SO_3^+/HSO_3^+	-	-	68	Ba^{2+}	236	$BaSO_4^+$

Tab. 10 Peaks observed in the mass-to-charge ratio of the APT measurement of the SL barite after 898 days of recrystallization and identified ionic species.

m/n	Identified Species	m/n	Identified Species
2	H_2^+	65	Ba^{2+}
3	H_3^+	66	Ba^{2+}
17	OH^+	67	Ba^{2+}
18	H_2O^+	67.5	Ba^{2+}
19	$(H_2O)H^+$	68	Ba^{2+}
23	Na^+	69	Ba^{2+}
32	S^+/O_2^+	70	H_2Ba^{2+}
43	Sr^{2+}	77	BaO^{2+}
44	Sr^{2+}	77.5	BaO^{2+}
48	SO^+	78	BaO^{2+}
49	H_2SO^+	80	SO_3^+
50	H_2SO^+	81	SO_3^+/HSO_3^+
51	H_2SO^+	82	SO_3^+
52	H_2SO^+	153	BaO^+
53	H_2SO^+	186	$BaSO^{2+}$
64	SO^{2+}	234	$BaSO_4^+$

Band / Volume 354
Herstellung thermisch gespritzter Schichten mit optimierten Spannungseigenschaften
M. Mutter (2016), VI, 142, VII-XXII, xxvi pp
ISBN: 978-3-95806-200-9

Band / Volume 355
Entwicklung selbstheilender Wärmedämmschichten
D. Koch (2016), X, 120 pp
ISBN: 978-3-95806-201-6

Band / Volume 356
Betriebsstrategien für Brenngaserzeugungssysteme zur Anwendung in HT-PEFC-Hilfsstromaggregaten
D. Krekel (2017), IX, 265 pp
ISBN: 978-3-95806-203-0

Band / Volume 357
Korrosion metallischer Bipolarplatten in Hochtemperatur-Polymerelektrolyt-Brennstoffzellen
V. Weißbecker (2017), viii, 194 pp
ISBN: 978-3-95806-205-4

Band / Volume 358
Realistic Bandwidth Estimation in the Theoretically Predicted Radionuclide Inventory of PWR-UO2 Spent Fuel Derived from Reactor Design and Operating Data
I. Fast (2017), XI, 129 pp
ISBN: 978-3-95806-206-1

Band / Volume 359
Light Trapping by Light Treatment
Direct Laser Interference Patterning
For the Texturing of Front Contacts in Thin-Film Silicon Solar Cells
T. Dyck (2017), vi, 172, XI pp
ISBN: 978-3-95806-208-5

Band / Volume 360
Interface and Topography Optimization for Thin-Film Silicon Solar Cells with Doped Microcrystalline Silicon Oxide Layers
C. Zhang (2017), VII, 156 pp
ISBN: 978-3-95806-209-2

Schriften des Forschungszentrums Jülich
Reihe Energie & Umwelt / Energy & Environment

Band / Volume 361
Calibration and large-scale inversion of multi-conguration electromagnetic induction data for vadose zone characterization
C. von Hebel (2017), ix, 123 pp
ISBN: 978-3-95806-210-8

Band / Volume 362
Process-based modelling of regional water and energy fluxes taking into account measured neutron intensities by cosmic-ray probes
R. Baatz (2017), xvi, 135 pp
ISBN: 978-3-95806-211-5

Band / Volume 363
Quantitative Analyse der Lithiumverteilung in Kathoden- und Elektrolyt-Dünnschichten für Festkörperbatterien
C. Dellen (2017), vi, 161 pp
ISBN: 978-3-95806-214-6

Band / Volume 364
Intragruppentrennung Seltener Erden mittels neuer phosphororganischer Liganden
S. Hadić (2017), VIII, 164 pp
ISBN: 978-3-95806-215-3

Band / Volume 365
Automated Magnetic Divertor Design for Optimal Power Exhaust
M. Blommaert (2017), xxiv, 220 pp
ISBN: 978-3-95806-216-0

Band / Volume 366
PEM-Elektrolyse-Systeme zur Anwendung in Power-to-Gas Anlagen
G. Tjarks (2017), IV, 135 pp
ISBN: 978-3-95806-217-7

Band / Volume 367
Fundamental Insights into the Radium Uptake into Barite by Atom Probe Tomography and Electron Microscopy
J. Weber (2017), IX, 143 pp
ISBN: 978-3-95806-220-7

Weitere ***Schriften des Verlags im Forschungszentrum Jülich*** unter
http://wwwzb1.fz-juelich.de/verlagextern1/index.asp

Energie & Umwelt /
Energy & Environment
Band / Volume 367
ISBN 978-3-95806-220-7

JÜLICH
FORSCHUNGSZENTRUM